

ABSTRACT

Phased Array Impedance Tuning, Secure Transmission, and Nonlinear Spatial Intermodulation Suppression for Next-Generation Radar and Communications Systems

Pedro A. Rodriguez-Garcia, Ph.D.

Mentor: Charles P. Baylis II, Ph.D.

Simultaneously transmitting radar and communications signals from the same multi-beam phased array system, using spatial diversity, allows multiple functions to use the same frequency and can alleviate spectral congestion. An issue arises, however in a transmitter array that consists of power amplifiers connected to the antenna elements. Undesired spatial intermodulation beams are transmitted as a result of the nonlinearities in these power amplifiers and can degrade both radar and communications mission abilities. The research presented in this dissertation resolves the nonlinear intermodulation products caused by these power amplifier nonlinearities by element-wise impedance tuning between each power amplifier and antenna element to reverse the nonlinear distortion effects. To emphasize the importance of the flexibility that element-wise impedance tuning provides, the analysis of a single-beam phased array transmitter is presented to demonstrate the dynamic improvement in range for both radar and communications scenarios individually. The improvement results from resolving the mismatch between the antenna elements due to mutual coupling as the array scan angle

changes. Finally, to ensure secure communications messages while maintaining radar capabilities, a directional modulation technique is presented, as well as Barker code sequencing, to maintain communications security in the transmit and receive mode of the radar.

Phased Array Impedance Tuning, Secure Transmission, and Nonlinear Spatial Intermodulation
Suppression for Next-Generation Radar and Communications Systems

by

Pedro A. Rodriguez-Garcia, B.S., B.S., M.S.

A Dissertation

Approved by the Department of Electrical and Computer Engineering

Kwang Y. Lee, Ph.D., Chairperson

Submitted to the Graduate Faculty of
Baylor University in Partial Fulfillment of the
Requirements for the Degree
of
Doctor of Philosophy

Approved by the Dissertation Committee

Charles P. Baylis II, Ph.D., Chairperson

Robert J. Marks II, Ph.D.

Yang Li, Ph.D.

Liang Dong, Ph.D.

Jonathan Rylander, Ph.D.

Accepted by the Graduate School

May 2020

J. Larry Lyon, Ph.D., Dean

Copyright © 2020 by Pedro A. Rodriguez-Garcia

All rights reserved

TABLE OF CONTENTS

LIST OF FIGURES	vi
LIST OF TABLES	ix
ACKNOWLEDGMENTS	x
CHAPTER ONE	1
Introduction.....	1
1.1 Single-Beam and Dual-Beam Phased Array Antennas.....	3
1.2 Radar Range and Reconfigurable Matching Networks.....	6
1.3 Literature Review of the State-of-the-Art.....	9
1.4 Summary	20
CHAPTER TWO	22
Single-Beam Phased Array Impedance Tuning for Increased Radar Range	22
2.1 Mutual Coupling in Phased Array Transmitters	23
2.2 Phased Array Impedance Tuning.....	27
2.3 Summary	42
CHAPTER THREE	43
Dual-Beam Phased Array Impedance Tuning for Spurious Beam Suppression	43
3.1 Spatial Intermodulation Theory	45
3.2 Spatial Intermodulation Suppression	51
3.3 Comparison of Impedance Tuning with Predistortion.....	67
3.4 Summary	75
CHAPTER FOUR.....	77
Secure Transmission in Dual-Beam Phased Array Transmitters.....	77
4.1 Zero-Forcing Directional Modulation for Radar and Communications	79
4.2 Barker Code Radar Signal Synthesis	88
4.3 Summary	91
CHAPTER FIVE	92
Conclusion and Future Work.....	92
BIBLIOGRAPHY.....	95

LIST OF FIGURES

Figure 1.1. Single-beam phased array transmitter example.....	4
Figure 1.2. Dual-beam phased array transmitter example	5
Figure 1.3. Transistor load-pull output power contours	7
Figure 1.4. Maximum range detection improvement scene.....	8
Figure 1.5. Array reconfigurable circuit diagram	8
Figure 2.1. Example two-element mutual coupling.....	24
Figure 2.2. Four-element uniform linear microstrip array	27
Figure 2.3. Driven element impedances when scan angles are swept	28
Figure 2.4. Un-tuned broadside driven impedances and array pattern	30
Figure 2.5. Switched-state stub tuner layout and Smith Chart impedance coverage.....	31
Figure 2.6. Identically tuned broadside driven impedances and array pattern	34
Figure 2.7. Non-identically tuned broadside driven impedances and array pattern	35
Figure 2.8. Transmission coefficients for tuner cases.....	36
Figure 2.9. Un-tuned $\theta_s = -60^\circ$ driven impedances and array pattern	37
Figure 2.10. Un-tuned $\theta_s = -25^\circ$ driven impedances and array pattern	37
Figure 2.11. Un-tuned $\theta_s = +10^\circ$ driven impedances and array pattern	38
Figure 2.12. Un-tuned $\theta_s = +30^\circ$ driven impedances and array pattern	38
Figure 2.13. Tuner Smith Chart impedance coverage for varying scan angles	39
Figure 2.14. Tuned $\theta_s = -60^\circ$ driven impedances and array pattern	40
Figure 2.15. Tuned $\theta_s = -25^\circ$ driven impedances and array pattern	41

Figure 2.16. Tuned $\theta_s = +10^\circ$ driven impedances and array pattern	41
Figure 2.17. Tuned $\theta_s = +30^\circ$ driven impedances and array pattern	42
Figure 3.1. Dual-beam block diagram with spurious beams on transmit	45
Figure 3.2. Array factor derivation from array elements and propagation vector	47
Figure 3.3. Theoretical dual-beam array patterns for $\theta_r = -30^\circ$ and $\theta_c = +40^\circ$	49
Figure 3.4. Theoretical dual-beam array patterns for $\theta_r = +10^\circ$ and $\theta_c = -15^\circ$	49
Figure 3.5. Theoretical dual-beam array patterns for $\theta_r = +50^\circ$ and $\theta_c = -50^\circ$	50
Figure 3.6. Input power vs. output power plot for MWT-173 transistor	52
Figure 3.7. Element antenna feed without and with reconfigurable matching network	54
Figure 3.8. Element-wise matching networks connected to each element	54
Figure 3.9. Impedance tuner Smith Chart coverage	55
Figure 3.10. Ideal dual-beam array pattern for $\theta_r = -30^\circ$ and $\theta_c = +40^\circ$	56
Figure 3.11. Un-tuned and tuned array pattern for $\theta_r = -30^\circ$ and $\theta_c = +40^\circ$	57
Figure 3.12. Ideal dual-beam array pattern for $\theta_r = +10^\circ$ and $\theta_c = -15^\circ$	61
Figure 3.13. Un-tuned and tuned array pattern for $\theta_r = +10^\circ$ and $\theta_c = -15^\circ$	61
Figure 3.14. Ideal dual-beam array pattern for $\theta_r = +50^\circ$ and $\theta_c = -50^\circ$	64
Figure 3.15. Un-tuned and tuned array pattern for $\theta_r = +50^\circ$ and $\theta_c = -50^\circ$	65
Figure 3.16. Predistortion array pattern for $\theta_r = -30^\circ$ and $\theta_c = +40^\circ$	69
Figure 3.17. Combination array pattern for $\theta_r = -30^\circ$ and $\theta_c = +40^\circ$	72
Figure 4.1. Dual-beam block diagram with spatial security	79
Figure 4.2. No directional security per-symbol dual-beam array pattern	82
Figure 4.3. Constellation diagram when no spatial security is enforced	83
Figure 4.4. Directional security per-symbol dual-beam array pattern in transmit mode ...	84

Figure 4.5. Transmit mode constellation diagram when spatial security is enforced.....85

Figure 4.6. Directional security per-symbol dual-beam array pattern in receive mode86

Figure 4.7. Receiver dual-beam array pattern.....87

Figure 4.8. Receive mode constellation diagram when spatial security is enforced87

Figure 4.9. Transmit and receive barker coded radar signal.....89

Figure 4.10. Ambiguity function of received radar signal.....90

LIST OF TABLES

Table 2.1. Tuner Transmission Coefficients with Identical Tuning States.....	35
Table 2.2. Tuner Transmission Coefficients with Non-Identical Tuning States	35
Table 2.3. Radar Range Improvement for Varying Scan Angles	40
Table 3.1. Comparison of Array Pattern Magnitude for $\theta_r = -30^\circ$ and $\theta_c = +40^\circ$	59
Table 3.2. Un-Tuned IMD3 Reversal Factor Values for $\theta_r = -30^\circ$ and $\theta_c = +40^\circ$	59
Table 3.3. Tuned IMD3 Reversal Factor Values for $\theta_r = -30^\circ$ and $\theta_c = +40^\circ$	59
Table 3.4. Comparison of Array Pattern Magnitude for $\theta_r = +10^\circ$ and $\theta_c = -15^\circ$	62
Table 3.5. Un-Tuned IMD3 Reversal Factor Values for $\theta_r = +10^\circ$ and $\theta_c = -15^\circ$	63
Table 3.6. Tuned IMD3 Reversal Factor Values for $\theta_r = +10^\circ$ and $\theta_c = -15^\circ$	63
Table 3.7. Comparison of Array Pattern Magnitude for $\theta_r = +50^\circ$ and $\theta_c = -50^\circ$	65
Table 3.8. Un-Tuned IMD3 Reversal Factor Values for $\theta_r = +50^\circ$ and $\theta_c = -50^\circ$	65
Table 3.9. Tuned IMD3 Reversal Factor Values for $\theta_r = +50^\circ$ and $\theta_c = -50^\circ$	66
Table 3.10. Predistortion IMD3 Reversal Factor Values for $\theta_r = -30^\circ$ and $\theta_c = +40^\circ$	70
Table 3.11. Combination IMD3 Reversal Factor Values for $\theta_r = -30^\circ$ and $\theta_c = +40^\circ$	72
Table 3.12. Radiated Power and IMD3 Beam Values for $\theta_r = -30^\circ$ and $\theta_c = +40^\circ$	74
Table 3.13. Radiated Power and IMD3 Beam Values for $\theta_r = +10^\circ$ and $\theta_c = -15^\circ$	75
Table 3.14. Radiated Power and IMD3 Beam Values for $\theta_r = +50^\circ$ and $\theta_c = -50^\circ$	75

ACKNOWLEDGMENTS

First and foremost, I would like to thank God for blessing me with the opportunity to be at Baylor for graduate school. I would also like to thank my advisor Dr. Charles Baylis, for his input, encouragement, and support in my academic pursuits at Baylor. I would also like to thank Dr. Robert Marks for his continually generous contributions to this work and his humor. I wish to acknowledge the assistance and support of Lawrence Cohen of the Naval Research Laboratory, William Crespo of the Naval Surface Warfare Center – Crane Division, and Jack Sifri of Keysight Technologies for their experience, industry expertise, and knowledge that contributed positively to this work. I would like to thank my employer, Raytheon, for financial support, flexibility, and patience as I pursued this academic interest as an admitted member of the Raytheon Space and Airborne Systems Advanced Studies Program. I want to acknowledge Keysight Technologies for their donation of the Advanced Design System Software and Modelithics for their donation of various simulation model libraries. I would also like to acknowledge the National Science Foundation and the Naval Research Laboratory for sponsoring part of this work.

To conclude, I would like to thank my family members: my mother Delmy, my father Pedro, my brother Benjamin, and my grandfather Papa Mincho who is watching over me from Heaven. This was only possible with your unconditional love and support.

CHAPTER ONE

Introduction

Many spectral bands previously allocated for radar transmission have recently been re-allocated for sharing with wireless communications. For example, 3.45 to 3.7 GHz has been re-allocated from solely radar use to shared radar/communications use. New approaches for radar transmission are required to ensure accurate, high-resolution radar detection while coexisting with other wireless devices. In the fifth-generation (5G) radio spectrum management structure, spectrum is expected to be allocated in real-time for the microwave and millimeter wave bands [1]. Much like the spectral domain, the spatial domain can also be exploited to enhance shared-frequency operations using multi-beam phased array antenna systems which transmit different signals in different directions from the same operating frequency. Multi-beam transmissions allow frequencies to be shared by more than one user, relying on spatial diversity to avoid self-interference, and allowing multiple capabilities to be employed from the same system. Transmitting simultaneous radar and communications signals from the same dual-beam phased array system, therefore, is a reliable way of mitigating the spectrum sharing problem [2]. Forming a hybrid system in which both functionalities use the same frequency band can result in more efficient real-time spectrum usage, as well as reduced cost and computation in a joint spatial and spectral regulatory framework [3].

This research serves as an expansion of previous work performed at Baylor University in adaptive next-generation radar [4] transmission to include multiple phased

array antenna elements. The work done previously included the optimization of a 90 W evanescent-mode S-band cavity impedance tuner [27], conceivably used for radar due to its high-power tunable circuitry, connected between a single power amplifier (PA) and a 50Ω antenna load. The circuit and waveform optimizations were developed to adaptively tune the reconfigurable matching network in real-time to present the optimal load reflection coefficient Γ_L to the preceding power amplifier as operating frequency changes to maximize the transmitter power, therefore increasing range capabilities while conforming to spectral constraints for coexistence.

While the previous work showed quick and successful tuning results in a single-element transmitter, practical radar systems employ multiple-element phased arrays. This research investigates the expansion of the adaptive, reconfigurable next-generation radar capabilities previously addressed to a multiple-element phased array system suitable for real-world mission scenarios. Chapter One, Section 1.1 discusses the background of single-beam and dual-beam phased array antennas. Section 1.2 includes a discussion of radar range capabilities and improvement that can be accomplished with reconfigurable matching network circuitry. Section 1.3 describes a literature review of previously developed capabilities by others in phased array impedance matching and includes a description of how the research in this dissertation is different from and novel compared to the previous approaches. Chapter Two describes the process involved in applying element-wise impedance matching to a four-element single-beam radar phased array transmitter system to increase range detection capabilities. Chapter Three describes a novel solution in applying reconfigurable circuitry to a dual-beam radar and communications (RadCom) phased array transmitter system to suppress unwanted

artifacts that are transmitted as the result of power amplifier nonlinearities. Chapter Four discusses a technique for implementing directional security in a dual-beam RadCom phased array assuming knowledge of the location of a potential eavesdropper. For this work, G. Ledford assisted with calculations of the baseband weighted vector. C. Baylis and R. J. Marks supervised the work and consulted the pseudo-inverse method in conjunction with directional modulation for use with RadCom systems. Finally, Chapter Five presents some conclusions from this dissertation research and discusses potential future work investigating the expansions of the innovations presented in this dissertation.

1.1 Single-Beam and Dual-Beam Phased Array Antennas

A phased array antenna is an assembly of multiple individual antenna elements grouped together to act as a single transmitter. When transmitting, radio waves from the single antenna elements constructively interfere to provide increased radiation in a certain direction, creating a main radiated beam, while, in other directions, radio waves also destructively interfere to suppress radiation in other directions, creating nulls in the beam pattern. The main beam of the phased array can also be electronically steered to change the direction of the main beam without physically moving the array. The antenna radiation gain increases as the number of elements increases, providing a narrower beam width in the desired steering direction. When the beam width of the main beam is narrower, the radar array can more precisely resolve the direction in which a target is located. Since phased array transmitters deliver increased directional radiation without physical movement, they provide faster and more accurate radar target tracking precision. Such precision is more suitable for radar applications than single-antenna transmitters,

which transmit a nearly omni-directional radiation pattern that is not suitable for accurate target tracking.

Phased arrays can be designed to transmit a radiation pattern with a single beam or multiple beams, depending on the desired application. Figure 1.1 shows a visual representation of a single-beam uniform linear array (ULA) phased array transmitter in which the elements are placed on a line and spaced a certain distance d apart.

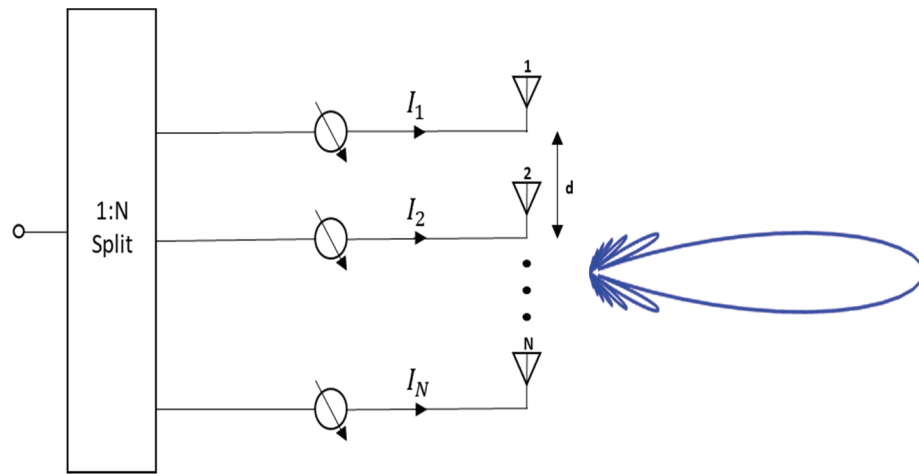


Figure 1.1. Visual representation of a single-beam ULA transmitter.

The ULA beam pattern that is synthesized by an array consisting of N elements for a single-beam array shown in Figure 1.1 is described by [5]

$$AP(\theta)_{single-beam} = f(\theta) \sum_{n=0}^{N-1} I_n e^{jnk_0 d \sin \theta}, \quad (1.1)$$

where $f(\theta)$ is the element radiation factor of the individual antenna elements used, $k_0 = 2\pi/\lambda_0$ is the wavenumber, d is the spacing between each individual antenna element, and I_n is the individual antenna element feed signal. Beam steering without physically moving the array is accomplished by providing a linear phase shift distribution of the

individual antenna element feed signals I_n , which must be preserved to maintain the array pattern shape and desired steering direction. To steer the ULA main beam for the single-beam transmitter, $I_n = |I_n|e^{-jnk_0d\sin\theta_s}$, where θ_s is the desired steering direction from -60° to $+60^\circ$ and $|I_n|$ is the desired magnitude of the excitation signal at element n .

A dual-beam, shared-frequency phased array has an advantage over the single-beam phased array in that it can be used for a simultaneous radar and communications co-design (RadCom) objective from a single transmitter at the same operating frequency.

Figure 1.2 shows a visual representation of a dual-beam ULA transmitter.

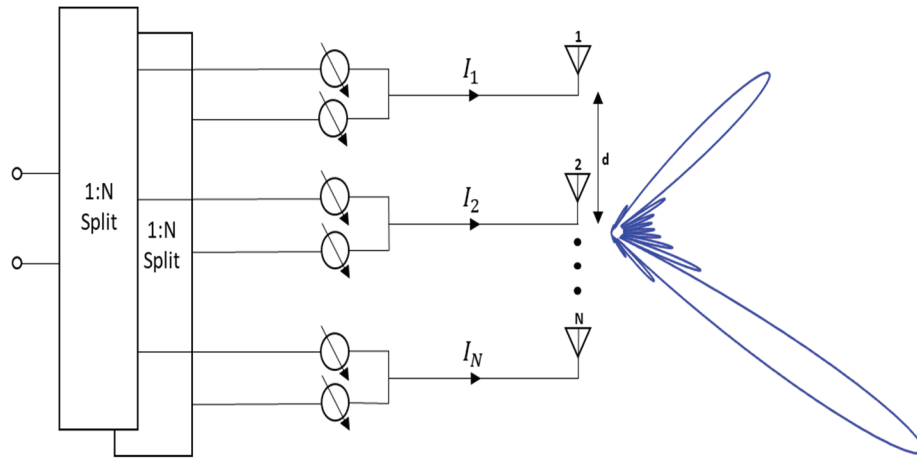


Figure 1.2. Visual representation of a dual-beam ULA transmitter.

As shown in Figure 1.2, two main beams can be transmitted at the same operating frequency from the same phased array. To provide two main beams, the excitation signals I_n are modified to be $I_n = I_{r_n} + I_{c_n} = |I_{r_n}|e^{-jnk_0d\sin\theta_r} + |I_{c_n}|e^{-jnk_0d\sin\theta_c}$, where θ_r is the desired radar main beam steering direction from -60° to $+60^\circ$, θ_c is the desired communications main beam steering direction from -60° to $+60^\circ$, $|I_{r_n}|$ is the magnitude of the radar excitation signals, and $|I_{c_n}|$ is the magnitude of the communications

excitation signals. The array pattern equation for the dual-beam transmitter therefore follows from a modified version of equation (1.1), in which the two excitations are summed together before they are fed to the individual antenna elements:

$$AP(\theta)_{dual-beam} = f(\theta) \left(\sum_{n=0}^{N-1} I_{r_n} e^{jnk_0 d \sin \theta} + \sum_{n=0}^{N-1} I_{c_n} e^{jnk_0 d \sin \theta} \right). \quad (1.2)$$

1.2 Radar Range and Reconfigurable Matching Networks

Next-generation radar systems must adapt in real-time to changing frequency constraints as well as changing beam steering directions (scan angles), while providing optimum output power for increased detection range as the radar sweeps the operating space to detect targets. The radar range equation, which describes the maximum radial range from the radar that a target can be reasonably detected, is described as

$$R_{max} = \sqrt[4]{\frac{P_t G^2 \lambda^2 \sigma}{(4\pi)^3 P_{min}}}, \quad (1.3)$$

where P_t corresponds to the transmitter output power, G is the magnitude of the array gain described in the previous section, λ is the transmitter wavelength, σ is the target radar cross section, and P_{min} is the minimum detectable signal power. According to (1.3), if all other terms remain constant and the transmitter output power P_t decreases, a decrease in maximum radar detection range results. The decrease in transmitter output power results from the changing mutual couplings in the antenna elements as the phased array transmitter changes scan angle. Changing mutual couplings of the antenna elements cause different load impedances to be presented to the preceding power amplifiers (PAs), as will be discussed in detail in Chapter Two. These varying load impedances can reduce

the output power, causing a significant reduction of radar range detection capabilities. An experiment was conducted in the Keysight Advanced Design System (ADS) simulation software to demonstrate the effects of varying load impedances on the output power. A load-pull simulation was taken of an MWT-173 transistor PA with output power contours shown in Figure 1.3 representing the variation of output power with load impedance. The marker “m1” in Figure 1.3 corresponds to the optimum output-power load impedance for each of the array amplifiers. Presenting this load impedance to each power amplifier in the array would maximize transmitter output power, maximizing the radar detection range. The markers “m2” through “m5” are arbitrarily placed on the load-pull contours that correspond to load impedances that result in output power levels that are 3 dB below the maximum power level, which could result when changing array scan angle. If these load impedances are presented to the PAs and are left unchanged, this can result in a 16 percent reduction of radar detection range.

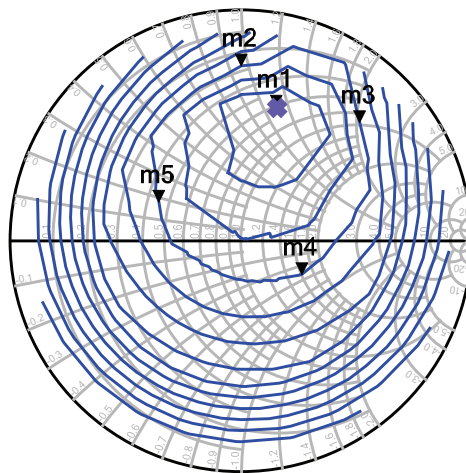


Figure 1.3. Simulated load-pull transistor output power variations.

To maintain maximum output power transmission, thus maximizing radar detection range as the array changes its scan angle, reconfigurable matching circuitry is placed between the PAs and antenna elements to resolve the mismatch that occurs from the mutual couplings of the array elements. Reconfiguring as the radar scans the operating space for targets allows the radar range to be optimized for any scan angle as shown in Figure 1.4. Figure 1.5 shows a block diagram of how the reconfigurable matching networks are placed in the phased array transmitter.

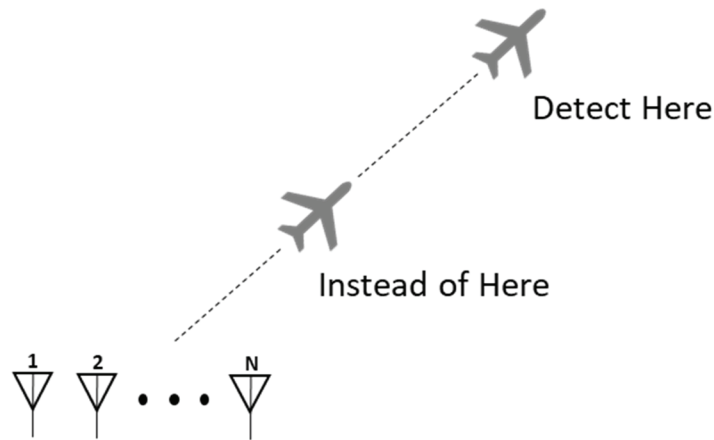


Figure 1.4. Phased array transmitter with increased detection range at new scan angle.

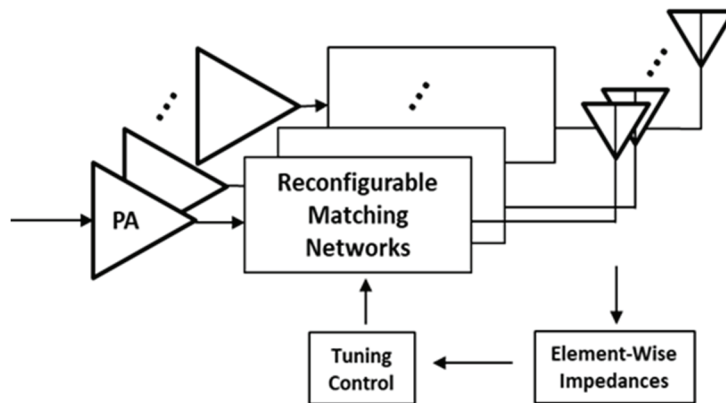


Figure 1.5. Block diagram of element-wise array matching circuit configuration.

Element-wise impedance tuning, as shown in Figure 1.5, can allow beam integrity to be maintained while maximizing radar range in both single-beam and dual-beam transmitter problems, as presented throughout this dissertation. Maximum radar detection range capabilities for both single-beam and dual-beam transmitters can be optimized in real time using these reconfigurable matching networks, regardless of desired scan angle. The solution presented in this dissertation provides the freedom and flexibility that will benefit next-generation radar and communications systems.

1.3 Literature Review of the State-of-the-Art

1.3.1 Power Amplifier Nonlinearities in Two-Tone and Single-Tone, Dual-Beam Transmitters

The works in [6]-[13] describe intermodulation artifacts that appear in the transmissions of multi-beam, multi-tone phased arrays that result from the third-order nonlinearities of power amplifiers. In their work, detailed calculations are performed and the third-order intermodulation products that occur at the $2f_1 - f_2$ and $2f_2 - f_1$ intermodulation frequencies are shown. Emphasis is placed on two-tone phased array transmitters that will have spatial intermodulation beams or “beat beams” at the intermodulation frequencies mentioned. Sandrin [6] gives measurement results verifying that for two intended main beams transmitted at 4000 MHz and 4010 MHz, two unintended beat beams occur at 3990 MHz and 4020 MHz. The beat beams are generally high-magnitude beams that are unintended and should be mitigated properly. Larsson [7] describes nonlinearities in multi-tone transmissions that are caused by PA hardware in antenna arrays in single-user and multi-user beamforming communications scenarios. In the single-user case, the non-linearities are beamformed into the same direction as the

desired signal. In the multi-user case, the nonlinearities are beamformed into different spatial directions which are different from that of the desired signals. Hemmi [8] also provides further details on two-tone phased array transmissions and provides detailed equations of the third-order nonlinear response of the transmit power amplifier. Haupt [9] provides a time-domain analysis of antenna arrays and describes the time-dependent spurious signals that arise from nonlinearities in the amplifiers in two-tone transmitters. Mollen [10] uses Hermite polynomials to model PA nonlinearities that cause radiation pattern distortion in multi-tone communications transmissions. The radiation pattern caused by the distortion resembles that of the desired signal when there is a single dominant user and is more spatially spread when there are multiple dominant users at different frequencies. Zaghoul [11] demonstrates experimental measurement and demonstration of intermodulation products for two-tone Ku-band phased array. System level performance is assessed through the carrier-to-noise-and-interference ratio (CNIR) in which PA nonlinearities contribute to its degradation. Loyka [12] discusses nonlinear effects in active array antennas. In a multi-tone scenario, the intermodulation beams have different directions at the intermodulation frequencies than those of the main beams at the fundamental frequencies. These intermodulation beams impact array performance and an instantaneous quadrature technique is implemented to provide accurate models for calculating the intermodulation products. Obermier [13] discusses the nonlinear effects of PAs on the array pattern of a spaced based transmitter. The intermodulation distortion (IM) that results from the nonlinearities are transmitted in the far-field which produces intermodulation beams. An analysis of the equivalent isotropic radiated power (EIRP) is performed and it was found that different types of PAs produce different levels of IM

distortion, so system requirements should determine which type of PAs to implement in the design. The analyses in these works show that the beat beams that occur from these nonlinear transmissions are significant, can cause system performance degradation, and therefore should be properly mitigated.

The research in this dissertation is a special case of the works in [6]-[13] in that a shared-frequency phased array for a joint radar and communications (RadCom) system is analyzed, relying on spatial diversity to avoid self-interference as described in Chapter Three, rather than a multi-tone system as described in these sources.

1.3.2 Mitigation Techniques for Power Amplifier Nonlinearities in Phased Array Transmitters

Kaho [14] describes a single-beam transmission scenario in which the intended carrier beam and IM beam components are transmitted in the same direction. Kaho uses an IM controller consisting of a predistortion-type linearizer and variable phase shifters. This technique attempts to increase the carrier to IM power ratio (C/IM) by steering the main IM beams away from the main carrier beam while simultaneously reducing the magnitude of the IM beams. By using the IM controller technique, the C/IM₃ ratio was improved by 8 dB, from 18 to 26 dB when the intended carrier beam was steered to broadside (0°). Rupakula [15] describes in detail the nonlinear IM products that occur in a single-beam 5G phased array receiver as a result of the presence of multiple interferers. The third-order IM products (IM₃) are highest in magnitude in certain predictable scan angles and can limit the sensitivity of the receiver. Rupakula explains that by using a Taylor taper across the elements in the array, the highest magnitude interferer level is lowered only by -3.47 dB compared to an array without an applied Taylor taper. It is also

explained that nulling interferers using adaptive phased array nulls also have little effect on the IM3 component in the array even if the interferer is nulled by 25 dB. Yamauchi [16] describes the presence of intermodulation distortion (IMD) and interference distortion (IFD). Yamauchi describes the process of reducing the nonlinear distortion (NLD) by removing the IFD at the receiving end in a MIMO active phased array antenna. In the multi-beam satellite communications system, NLD is calculated as the sum of the IMD and IFD products that appear as a result of power amplifier nonlinearities. This source describes a two-tone transmission that reduces the IFD beams at the receiving point by increasing the number of antenna elements to produce sharp beams for good isolation of the IFD and IMD beams. Lier [17] demonstrates an intermodulation suppression technique for satellite systems by selecting different aperture phase distributions per beam and suppressing the power of the IM beams at the intended transmitted directions. Lier assumes different carrier frequencies per beam in this source. The phase excitations are selected by a linearly constrained minimax optimizer using a reduced gradient algorithm. The in-band IM products are essentially steered away from the intended carrier beams to reduce the IM power in the coverage region. Johannsen [18] explains that in the case of nonlinear power amplifier operation, IM distortion is generated by the distributed power amplifiers in a scanned beam satellite-communications phased array. Some IM radiated power falls outside the intended scan beam area, and some fall inside the intended scan beam area with different carrier frequencies. The frequency reuse system presented in this source realizes an average IM distortion reduction of several dB. The input signal consists of multiple carrier frequencies and with frequency reuse, a second or third set of carriers of the same

frequencies, but with different phase shifts, are combined with the first set of carriers prior to amplification. The result is a greater spatial dispersion of the IM products as the intended coverage area is covered several times by the same carrier frequencies.

O'Connor [19] uses waveform engineering to avoid power amplifier intermodulation distortion in a shared aperture radar and communications system. The input signals to the power amplifiers are constrained to be constant envelope, and an approximation is constructed that gives lower peak-to-average power ratio (PAPR) as opposed to the combination of the two desired signals. The inherent trade off in this approach is that half the effective radiated power (ERP) must be exhausted from the radar to satisfy the constant envelope constraint. An approximation is constructed to relax the constant envelope constraint but has lower PAPR which reduces the potential for intermodulation distortion and produces a nearly constant envelope waveform to dedicate more ERP to the radar signal. Haupt [20] provides a detailed analysis of power amplifier modeling techniques for multi-beam, multi-tone wideband phased array transmitters. Haupt compares Hemmi's nonlinearity polynomial model [8] to the Rapp nonlinearity model [21] and provides insight that care should be taken when selecting a nonlinear model for modeling performance near and in compression. Based on experimental results, when the PA model is used near compression, the polynomial model may be convenient, but could be inaccurate compared to the Rapp model for choosing an operating point that reduces PA nonlinearities in the transmitted array pattern. Braithwaite [22] applies digital predistortion (DPD) to reduce the intermodulation (IMD) beams that occur from PA nonlinearities in a dual-beam, shared-frequency system. With a third-order nonlinearity, four beams are transmitted: two intended beams, and two intermodulation beams. DPD

modules are applied for beam correction in each of the four transmitted beam directions: two for the intended linear beam directions, and two for the unintended IMD beams directions. The basis waveform models used for each DPD module in each of the four transmitted directions are assumed to be memoryless. Experimental results for a 32-element array show that DPD can be used to suppress the IMD beams that are transmitted. The magnitudes of the two main beams, however, are also affected, since the overall array pattern shape is modified as a result of the DPD.

The research presented is novel in that it demonstrates element-wise impedance tuning to maximize transmitter output power and beam integrity for a single-beam system and for a shared-frequency, dual-beam joint radar and communications system. An analysis on the array pattern of a shared-frequency, dual-beam RadCom array caused by the antenna signals fed by the outputs of the individual power amplifiers is described and the results are presented. As described in detail in Chapter Three, the IMD products distort the magnitude and phase progression of the antenna feed signals severely, however, these effects can be mitigated by individually impedance tuning each of the elements such that the IM distortion is reversed. The original intended array pattern is therefore restored as a result [23].

1.3.3 Reconfigurable Impedance Tuning Between Amplifier and Antenna Load

Impedance matching between the power amplifier and antenna load for maximum power transfer has been investigated in the literature. Sun [24] overviews automatic antenna tuning using fast tuning algorithms, impedance monitoring, and programmable matching systems in a software-defined radio (SDR) platform. The design and operation of automatic antenna tuning units (AATUs) is discussed using on-chip matching

networks for UHF to microwave transceiver antennas. The AATUs consist of three major components: an adjustable matching network that produces the required impedance transformation, an impedance sensor, and a control system which includes a tuning algorithm to adjust the matching network in response to feedback data from the impedance sensor. The adjustable matching network consists of a modified pi-matching network array with variable inductors and capacitors placed for a CMOS on-chip tuner application. The work presented in this source only considers one power amplifier and one antenna element, so an adjustment for an array of elements is needed as suggested by this dissertation. De Mingo [25] presents two antenna input impedance automatic pi-matching lumped-element systems. The first design includes a simplified version of a generic tuner that can achieve good match between the antenna and the amplifier with low losses. The second design includes an application specific integrated circuit (ASIC) control unit that implements a complex search algorithm. The impedance tuning suggested in this work is meant for receivers in mobile systems whose antenna input impedance experiences changes from the environment and the human body interactions from the user. The tuning mechanism used here, once again, was intended for a single antenna and a single amplifier. Gu [26] presents a direct calculation method for adaptive matching network control utilizing an analytic algorithm based on an integrated measurement of antenna load impedance. A pi-network is employed, and as the matching network element values and the optimal tuning conditions are found directly within hundreds of microseconds following updating of the new antenna load impedance from the processor. The key blocks include the tunable pi matching network, load impedance measurement circuitry, and analytic match tuning algorithm. As in the case of the other

sources, this source presents adaptive impedance tuning for only one element. All works presented above implement the matching network techniques for use in mobile communications systems in which high power handling capability is not a specific requirement and coherent transmission from an array is not anticipated. For radar systems, high power handling capacity is required, so impedance tuning methods that can handle high-power tuning should be considered. Semnani [27] demonstrates a 90 W evanescent-mode S-band cavity tuner design that could conceivably be used in radar phased array tuning. Alcalá-Medel [28] presents a fast impedance tuning algorithm to maximize radar detection range over operating frequency and antenna input impedance changes using Semnani's evanescent-mode S-band cavity tuner.

This dissertation expands upon the tuning mechanisms in [27] and [28] to include an array of power amplifiers and antenna elements as well as an array of high-power handling capable impedance tuners. The problem becomes more complex when an array of transmitters is considered, because the mutual couplings of the antenna elements fluctuate as each individual element is tuned to the desired impedance [5]. The experiments discussed in this dissertation show that the impedances essentially become a “moving target”: once one element is tuned, the adjacent element impedances are distorted and re-tuning the impedances to account for this phenomenon is needed. This dissertation provides a system-level solution for this problem, in that both the individual power amplifiers as well as the array of antenna elements are considered and tuned while preserving the array pattern shape as well as desired scan angle.

1.3.4 Phased Array Scan Angle Impedance Matching

For a single-beam, phased array transmitter, wide-angle impedance matching techniques according to the sources in [29]-[31] have been suggested as a way of handling the changes in individual antenna element impedances as the array is steered to different directions. The antenna element impedances change due to the change in the mutual couplings of the elements as the array changes scan angle. This results in dynamic mismatches that may decrease the overall gain of the array, reducing transmit range in either radar or communications applications. The objective of the work by Luther [29] is to eliminate the use of phase shifters in a 3-element microstrip steerable parasitic array radiator, using tuning stubs and compensation varactors to preserve resonance at the operating frequency. Open-circuited stubs are placed at the parasitic ports, and their geometries are designed to achieve electronic scanning from -20° to $+20^\circ$ elevation. The center antenna is the driving element and is fed through microstrip-to-slot coupling. This static design was able to achieve the intended beam scanning from -20° to 20° while maintaining low return loss for all scan angles in this range. Using the center antenna as the driving element and the outer two antennas as parasitic elements, no phase shifters were required to steer the beams in this range. Since mutual coupling between closely spaced patch antennas is an effective feed mechanism, the beam was steered by reactive loading at the parasitic radiator terminals. Magill [30] describes the changing magnitude of reflections with scan angle and wave polarization. The presented solution is to compensate for the changing reflections as the array changes scan angle by placing a dielectric sheet in front of the array. The dielectric sheet serves as a purely shunt susceptible medium in space. Calculations are detailed in this source for the thickness of

the sheet and the required dielectric constant ϵ_r to provide wide-angle impedance matching. It is shown in simulations and measurement that this dielectric sheet compensates for most of the wide-angle variation reflections to the phased array transmitter. Xia [31] presents a microstrip phased array using an overlapped feeding network to achieve wide-angle impedance matching. The array can scan from -60° to 60° with a gain decrease lower than 3 dB. Overlapped subarrays are realized by overlapping the power dividers in the feeding network. As a result, the feedlines of the array elements are connected to each other which results in compensation of the mutual couplings in the array elements as the scan angle changes. Simulated and measurement results show that with the overlapped feeding structure in this static design, low return loss was achieved for scan angles between -60° and 60° .

A solution in this dissertation that is distinct from the sources above is that a simple microstrip array design is used with reconfigurable matching circuits placed between the antenna elements and the preceding power amplifiers [32]. Since the matching circuits are reconfigurable and can adapt for any scan angle, there is no need to implement a complex array structure such as those designed in the works above. Implementing this solution shows promise for providing greater flexibility and freedom. In addition, it is expected to be usable with a simpler array design, while still providing maximum power from the power amplifiers to increase range capabilities.

1.3.5 Secure Communications from Joint Radar and Communications Systems

Blunt [33]-[35] presents a RadCom system that enables generation of arbitrary signals as a function of spatial angle and time via a MIMO transmitter. Blunt uses phase-attached radar-communications (PARC) [33] to maximize data throughput and energy on

target. In Blunt's approach, the radar and communications modes are combined into a single, frequency modulated (FM) waveform through a summation of two continuous phase structures. The radar phase structure remains unchanged, whereas the communications phase structure is generated based on the data to be transmitted. Initial phase shift estimates for the communications structure is achieved by transmitting radar-only sweeps during which the transmitted waveform is known completely at the communications receiver. With this knowledge, appropriate demodulation at the communications receiver is validated and spectral resources are shared efficiently. Blunt also presents a far-field radiated emission design (FFRED) [34] to transmit multiple independent data streams in arbitrary spatial directions while simultaneously maintaining the integrity of active radar sensing. The FFRED approach is a spatial diversity waveform design that constrains the emitted waveform to be constant modulus to minimize loss in radar transmit power. Through this iterative optimization approach, the resulting radar and communications waveforms are power efficient and spectrally well constrained as the measurements show. Blunt also demonstrates a tandem-hopped radar and communications approach (ThoRaCs) [35] in which undistorted orthogonal frequency division multiplexing (OFDM) waveforms are embedded into the FM structure of radar waveforms via an optimization process. The radar waveforms are therefore information-bearing waveforms that are designed to have constant amplitude for good power efficiency. Experimental results show that communications integrity and good radar performance are simultaneously achieved with the ThoRaCs approach. Spatial communications security should be considered in such systems, which can be addressed by the directional modulation concept presented in Bernhard's work [36]-[37]. Bernhard

presents a directional modulation scheme that is intended for use in phased array communications systems where knowledge of the location of an eavesdropper is known [36]. Directional security is achieved through intelligently selected phase shifts that are applied to the input excitation signals, purposely distorting the transmit constellation in the direction of the eavesdropper location. A genetic algorithm is presented that is used to select the phase shifts. A closed-form solution is available in the directional modulation technique of Xie [38] that quickly calculates the appropriate excitation phase shifts via a pseudo-inverse technique that requires much less computation time than a genetic algorithm. In a RadCom system, however, the radar signal must be transformed into a modulated signal that can utilize the techniques above and provide directional security. Yinjuan [39] describes Barker code sequencing to modulate a transmitted radar pulse.

The research presented in this dissertation combines the techniques described in [36]-[39] into an integrated RadCom system that achieves spatially secure communications [40]. This approach utilizes a uniform linear array (ULA) dual-beam system as described in Section 1.1. The excitations of each element are derived from a fixed frequency carrier modified by a baseband-weighted vector and applied to subsequent per-element power amplifiers. The baseband-weighted vector is calculated in real-time using zero-forcing directional modulation (ZF). Since the ZF method is deterministic and presents a reasonable computational workload, it is suitable for a novel real-time implementation of the proposed system.

1.4 Summary

This chapter introduced the research of this dissertation, including useful background information, and a literature review. Implementing phased array systems

with single-beam and dual-beam transmissions, which formulates the basis of the research, is described through equations and diagrams. The radar range equation and its importance to this research with reconfigurable impedance tuning is introduced, as is the novelty of this research compared to the state-of-the-art in this field.

CHAPTER TWO

Single-Beam Phased Array Impedance Tuning for Increased Radar Range

In a radar phased array system, mutual coupling between antenna elements can cause significant variations in impedance presented by the transmit antennas to the preceding circuitry when the scan angle varies [41]. This can negatively impact radar range capabilities. Reconfigurable circuitry can be used to provide matching to a power amplifier for improvement of output power, power-added efficiency (PAE), and/or spectral performance [42], and therefore can improve range. It has been shown in a simulation example that presenting the power amplifier with an antenna impedance away from the antenna impedance for which an amplifier load matching network was designed could reduce the output power by approximately 3 dB, which translated to a communication range reduction of 29.3%, or a radar range reduction of 15.9% [4]. To avoid such reductions, impedance tuners can be placed in each array element. For radar, real-time impedance tuning has long been impractical due to a lack of high-power tunable circuitry. Semnani, however, demonstrates a 90 W evanescent-mode S-band cavity tuner design that could conceivably be used in radar phased array tuning [43]. The works in [24]-[26] describe several reconfigurable antenna impedance tuning methodologies that adapt for changes in single-element antenna impedances due to environmental changes such as human hand and body effects in wireless communications handsets. An expansion is needed for a multi-antenna phased array system, as well as an analysis in the changing scan angles and transmission antenna gain for an active electronically scanned

array (AESA). Several other works have shown that wide-angle array impedance matching can be achieved [29]-[31] using various design techniques inherent to the phased array itself to resolve the array impedance mismatch. Implementing element-wise reconfigurable matching networks, however, is expected to provide more output power capability and greater flexibility in a real-time system than static wide-angle matched designs. Rather than a typical fixed power-amplifier matching network to match the antenna impedance to the optimal power-amplifier load impedance, a tunable matching network can allow the amplifier to be consistently loaded with its optimum termination as the array scan angle is varied, without degrading the array pattern. By placing impedance tuners in the individual elements of the array, each changing driven impedance can be matched to the power amplifier as the scan angle changes, as shown in Figure 1.5.

Through a co-simulation setup between Keysight Technologies Advanced Design System (ADS) circuit simulation software and ADS Momentum electromagnetic simulation software, the effect of element-wise reconfigurable circuitry on the range performance of radar can be analyzed, as well as the impact of impedance tuning on the transmitting array pattern. The results of this work are also expected to be applicable to fifth-generation (5G) wireless communication systems utilizing phased arrays.

2.1 Mutual Coupling in Phased Array Transmitters

Mutual coupling, according to Haupt [5], is the interaction between an antenna and its environment. In a phased array transmitter, an antenna element interacts with the other antenna elements in the array. The radiation from one antenna element causes apparent reflections in the other antenna elements, since every element receives some of the radiation from the other elements. Figure 2.1 illustrates this mutual coupling effect in

a simple two-element array. The second antenna radiates a wave that is received by the first antenna and vice versa. The received waves at each element travel from the antennas back to their sources, resembling reflected waves, causing changes in the driven element impedances presented by the antennas. As the scan angle is varied, the amount of mutual coupling between elements changes, changing the driven element impedances.

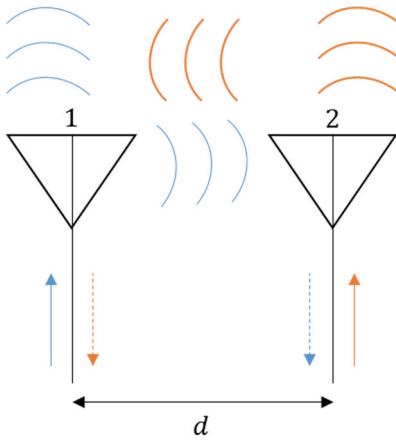


Figure 2.1. Radiation representation of mutual coupling between two phased array antenna elements.

The self and mutual impedances of each antenna element in a phased array can be represented by the well-known impedance matrix $[Z]$, which relates currents and voltages of the elements:

$$\begin{bmatrix} V_1 \\ \vdots \\ V_N \end{bmatrix} = \begin{bmatrix} Z_{11} & \cdots & Z_{1N} \\ \vdots & \ddots & \vdots \\ Z_{N1} & \cdots & Z_{NN} \end{bmatrix} \begin{bmatrix} I_1 \\ \vdots \\ I_N \end{bmatrix}. \quad (2.1)$$

For a two-element array, (2.1) reduces to the following:

$$\begin{aligned} V_1 &= Z_{11}I_1 + Z_{12}I_2 \\ V_2 &= Z_{21}I_1 + Z_{22}I_2. \end{aligned} \quad (2.2)$$

Assuming that the two-element array is a two-port linear circuit network, the self-impedance of each antenna is the impedance of the isolated antenna in the absence of the other antenna. If the current flowing into element 2 is zero (this can be enforced by terminating element 2 in an open circuit), the ratio V_1/I_1 is the Z_{11} term. Similarly, if antenna 1 is terminated in an open circuit, then the impedance presented by antenna 2 to its transmitter circuit is the self-impedance Z_{22} :

$$Z_{11} = \left. \frac{V_1}{I_1} \right|_{I_2=0} \quad Z_{22} = \left. \frac{V_2}{I_2} \right|_{I_1=0} . \quad (2.3)$$

The mutual impedances between antenna elements describe the mutual coupling. These terms represent the open-circuit voltage across an antenna input that results from a current input to the other antenna. For the two-antenna system, the mutual impedance terms are defined as follows based on (2.2):

$$Z_{12} = \left. \frac{V_1}{I_2} \right|_{I_1=0} \quad Z_{21} = \left. \frac{V_2}{I_1} \right|_{I_2=0} . \quad (2.4)$$

When antennas are placed in an array and excited simultaneously, the “driven element impedance” is the ratio of voltage across the antenna port to the current entering the antenna. The driven element impedances are a sum of their self and mutual impedances:

$$\begin{aligned} Z_{d1} &= \frac{V_1}{I_1} = Z_{11} + Z_{12} \frac{I_2}{I_1} \\ Z_{d2} &= \frac{V_2}{I_2} = Z_{21} \frac{I_1}{I_2} + Z_{22} . \end{aligned} \quad (2.5)$$

The driven element impedance equations in (2.5) can be expanded to compensate for any amount of array elements as well as for changing scan angle. For a linear two-element array, zero phase can be assumed for the first antenna current, and the second antenna current is assigned the same magnitude, with a phase shift based on the scan angle θ_s :

$$I_1 = |I_1|$$

$$I_2 = |I_2|e^{-jk_0d \sin \theta_s}.$$

For a linear array configuration, assuming canonical excitation of the array elements, the generalized driven element impedance of an N -element array with scan angle θ_s is given as follows [5]:

$$Z_{dn} = \sum_{m=1}^N Z_{nm} \frac{|I_m|}{|I_n|} e^{jk_0(n-m)d \sin \theta_s}. \quad (2.6)$$

From (2.6), the self-impedance terms ($n = m$) remain unchanged. Steering the array, however, changes the mutual impedance terms ($n \neq m$). Driven element impedance mismatches can therefore occur as a result of changing the array scan angle and can be mitigated properly with reconfigurable element-wise impedance tuners. Precautions must be taken, however, when tuning the individual array elements. When individual driven element impedances are altered in equation (2.6), the current sources are also altered in magnitude and phase. To preserve the integrity of the antenna pattern, the relative phases and amplitudes of the individual elements needed to steer the array to the desired scan angle must be unharmed. Although driven impedances for different array elements may be different, tuning to match each element individually can cause distortion in the beam pattern in such cases. Impedance tuning should therefore be performed to maximize power, while ensuring the actual transmitted beam pattern is close enough to the canonical beam pattern to be considered acceptable.

2.2 Phased Array Impedance Tuning

Simulations were conducted using a co-simulation with the Advanced Design System (ADS) circuit simulator and Momentum EM simulators from Keysight Technologies. A schematic was first generated with a uniform linear array (ULA) of four $\lambda/2$ -spaced microstrip patch antenna elements (Figure 2.2). The elements were designed using Rogers RO4003C substrate at the design frequency of 3.55 GHz, a frequency presently allocated for sharing between radar and wireless communications in the United States. Nonlinear models for the MWT-173 Gallium Arsenide (GaAs) metal-semiconductor field-effect transistor (MESFET) biased at $V_{DS} = 4.5$ V and $V_{GS} = -1.5$ V were connected to the antenna elements.

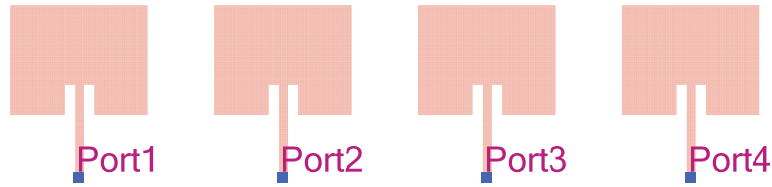


Figure 2.2. 4-element $\lambda/2$ uniform linear microstrip array in ADS.

Figure 2.3 shows a parameter sweep of the driven element impedances at 3.55 GHz as the array scans from $\theta_s = -60^\circ$ to $+60^\circ$ in the $\phi = 0^\circ$ cut that was conducted to observe the mismatch effects of varying the scan angle. In Figure 2.3, the driven end element impedances (elements 1 and 4) behave similarly and the driven inner element impedances (elements 2 and 3) behave similarly because of array symmetry.

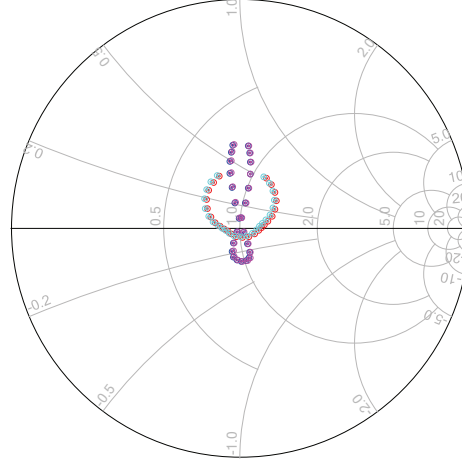


Figure 2.3. Parameter swept driven element impedances for scan angles of $\theta_s = -60^\circ$ to $+60^\circ$ at 3.55 GHz for $k_0 = 2\pi/\lambda$, $d = \lambda/2$, end elements (light blue and red), and inner elements (dark blue and purple).

The driven element impedances for this array of four elements follow from equation (2.6):

$$\begin{aligned}
 Z_{d1} &= \frac{V_1}{I_1} = Z_{11} + Z_{12} \frac{I_2}{I_1} + Z_{13} \frac{I_3}{I_1} + Z_{14} \frac{I_4}{I_1} \\
 Z_{d2} &= \frac{V_2}{I_2} = Z_{21} \frac{I_1}{I_2} + Z_{22} + Z_{23} \frac{I_3}{I_2} + Z_{24} \frac{I_4}{I_2} \\
 Z_{d3} &= \frac{V_3}{I_3} = Z_{31} \frac{I_1}{I_3} + Z_{32} \frac{I_2}{I_3} + Z_{33} + Z_{34} \frac{I_4}{I_3} \\
 Z_{d4} &= \frac{V_4}{I_4} = Z_{41} \frac{I_1}{I_4} + Z_{42} \frac{I_2}{I_4} + Z_{43} \frac{I_3}{I_4} + Z_{44}.
 \end{aligned} \tag{2.7}$$

To steer the beam to a direction θ_s , the individual current sources in (2.7), for a uniformly spaced linear array, follow the linear phase progression

$$\begin{aligned}
 I_1 &= |I_1| & I_2 &= |I_2| e^{-jk_0 d \sin \theta_s}, \\
 I_3 &= |I_3| e^{-j2k_0 d \sin \theta_s} & I_4 &= |I_4| e^{-j3k_0 d \sin \theta_s}.
 \end{aligned} \tag{2.8}$$

It is imperative that this phase progression remain unharmed when tuning the driven element impedances in (2.7) to preserve the integrity of the array pattern. From (2.8), the

first element is typically excited with no phase shift. The next consecutive elements all experience varying phase shifts so these relative phase shifts should be maintained to provide an undistorted array pattern and steer the array properly to the desired scan angle.

2.2.1 Tuning at Broadside

Upon observing these effects, the array was then steered to the broadside ($\theta_s = 0^\circ$) scan angle, with identical current-source excitations of each array element in magnitude and phase at 3.55 GHz. A load-pull assessing the variation of power delivered based on power amplifier load impedance was then conducted to determine the optimum terminating load impedance. The driven impedances were placed on the same load-pull plot in Figure 2.4 to show the power delivered load impedance level in which the un-tuned driven element impedances were located as well as the array pattern. Due to the equality of all four excitation currents, the initial driven element impedances for the broadside case are represented as a special case of equation (2.7):

$$\begin{aligned}
 Z_{d1} &= \frac{V_1}{I_1} = Z_{11} + Z_{12} + Z_{13} + Z_{14} \\
 Z_{d2} &= \frac{V_2}{I_2} = Z_{21} + Z_{22} + Z_{23} + Z_{24} \\
 Z_{d3} &= \frac{V_3}{I_3} = Z_{31} + Z_{32} + Z_{33} + Z_{34} \\
 Z_{d4} &= \frac{V_4}{I_4} = Z_{41} + Z_{42} + Z_{43} + Z_{44}.
 \end{aligned} \tag{2.9}$$

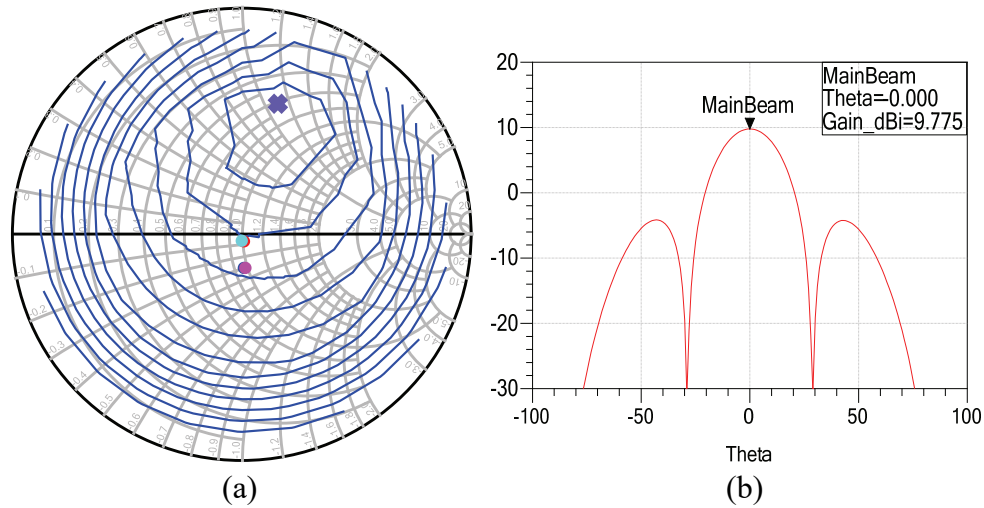


Figure 2.4. (a) Untuned driven element impedances for $\theta_s = 0^\circ$, (b) untuned array pattern (dBi).

Figure 2.4(a) shows the un-tuned driven element impedances with the output power load-pull contours. The un-tuned driven element impedances are not located at the maximum output power load impedance and according to the radar range equation (1.2). This power deficiency can result in a significant reduction of range detection radar capabilities if the driven element impedances are left unchanged without impedance tuning.

To mitigate this reduction of radar range and maximize the transmitter output power, the driven element impedances are tuned with models for the switched-state radial stub reconfigurable impedance tuners presented by Calabrese [44]. A tuner is placed between each antenna element and its associated power amplifier. The layout of the tuner and its 3.55 GHz driven element impedance coverage at broadside for each element is presented in Figure 2.5.

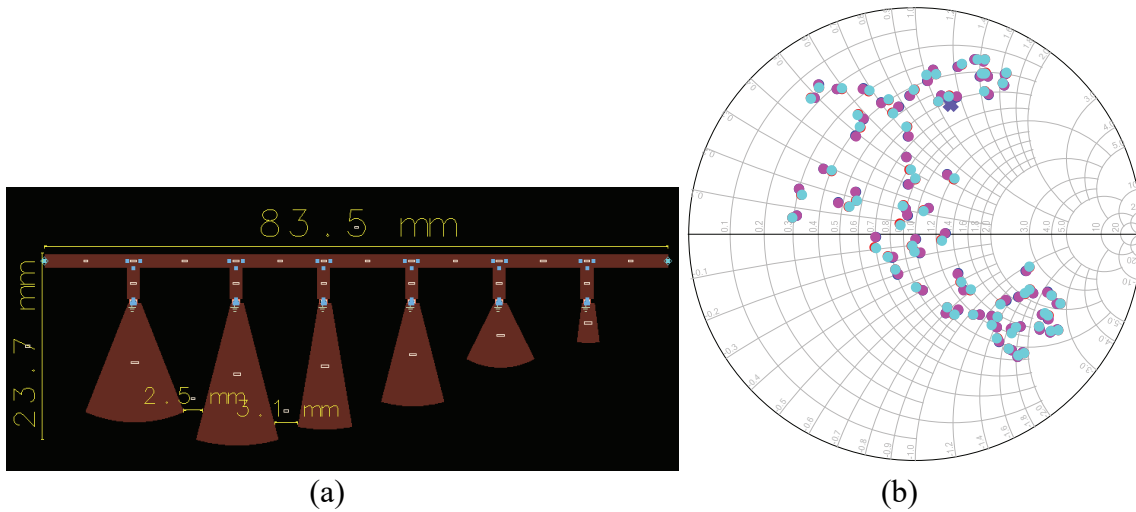


Figure 2.5. (a) Board layout of the switched-state radial stub impedance tuner, (b) tuner element-wise driven impedance coverage for $\theta_s = 0^\circ$ showing closest points to maximum PA power delivered load impedance (purple x-mark) at switch state 111110 for all tuners.

The tuner switch state combination can be represented with a binary sequence. A bit of “1” indicates a radial stub has been activated (presented to the series line by closing the switch), and a bit of “0” indicates a radial stub has not been activated (Figure 2.5(a)). Since there are a total of six radial stubs in the design, this switched-stub configuration provides a total combination of $2^6 = 64$ unique tuning states. The 3.55 GHz impedance coverage (Figure 2.5(b)) shows that it is possible to tune the driven impedances from Figure 2.4(a) for the $\theta_s = 0^\circ$ to the optimum power delivered load impedance to be presented to each power amplifier using this reconfigurable impedance tuner design. Tuner losses at the varying switch states, however, may differ significantly since different stubs are “activated” and “deactivated” according to the switch state. This means that not only must the impedance tuning mechanism consider the maximum power delivered load impedance, but also the tuner loss at the different switch states. The tuner design is discussed in greater detail in [44].

From Figure 2.5(b), there are at least two tuner switch states that could match the driven element impedances to the optimum PA load impedance. However, the losses may be different for the two states, so it is desired to find the state that provides the optimum tuner output power considering state-wise tuner losses. For this reason, the fast tuning algorithm presented by Calabrese [44] is used to determine the switch state needed to tune all driven element impedances to the maximum output power and account for tuner losses. The algorithm begins with the switch state of 000000 (all switches off). The power is subsequently measured at the output of each tuner which is fed to each element in the array. The first switch is toggled to the activated state and the output power is measured for improvement. If output power is improved by activation of the first switch, that switch remains activated and the process iterates through the rest of the switches. The algorithm is then re-iterated until no further improvement in output power is accomplished and the switch state that gives the maximum output power is selected [44]. In performing the search algorithm for driven impedances resulting from $\theta_s = 0^\circ$, the maximum output power is accomplished using a switch state sequence of 111110. This tuning state is applied to the tuners in all four elements to preserve the linear phase progression of the current sources; maintaining the scan angle and the array pattern shape, and tuning the driven element impedances to the optimum power delivered PA load impedance. The resulting tuned driven element impedances and the resulting array pattern for $\theta_s = 0^\circ$ are shown in Figure 2.6. Figure 2.6(a) shows that all tuned impedances presented to the power amplifiers are near the target load impedance on the Smith Chart.

As a result of the impedance matching, the achievable resulting transmit power increases from 19.2 dBm to 22.1 dBm, providing 18.2% radar range improvement. Figure 2.6(b) shows that the array scan angle and overall beam shape remain unharmed. Since each element uses the same tuner switch state of 111110, the adjustments to the magnitude and phase of the transmitted waveform in all elements are expected to be identical, preserving the beam pattern.

Figure 2.7 shows that tuning inner and outer elements differently can result in undesirable effects on the array pattern. The inner elements were tuned using the switch state sequence of 111110 whereas the outer elements were tuned with the switch state sequence of 000010, which is the state providing the next closest Γ_L to the maximum PA power delivered Γ_L considering tuner losses. Because similar values of Γ_L are presented in all elements, similar impedance matching is achieved. The number of exposed stubs, however, is very different between the two states, causing significant magnitude and phase adjustments to the voltage at the output of the tuner. Removing magnitude and/or phase equality between the circuitry in the different transmitter elements causes the transmitted pattern to be altered, as shown in Figure 2.7(b). The antenna gain at the intended scan angle of $\theta_s = 0^\circ$ is reduced from 9.767 dBi to -0.801 dBi (Figure 2.8(b)), and the two sidelobes possess higher gain than the desired scan angle. To steer the array to $\theta_s = 0^\circ$, the phases of all current excitations for all elements must be identical. Tuning the outer two elements with a different switch state alters their currents to be out of phase with the inner elements. Figure 2.8(a) shows that all four elements have the same transmission phase when the matching networks are tuned to the same switch setting, whereas Figure 2.8(b) shows that two different transmission phases exist for the scenario

where the outer and inner elements have different matching network switch settings. The magnitude and phase of S_{21} are shown in Tables 2.1 and 2.2, respectively, for each of the four elements. The difference in S_{21} magnitudes in Figure 2.8(a) is small at 3.55 GHz, but the difference in phases between the inner and outer elements is approximately 143° . As such, the phase differences between inner and outer element transmissions seems to be the main cause of the beam distortion visible in Figure 2.7(b), when compared to the case where all elements are tuned identically (Figure 2.6(b)).

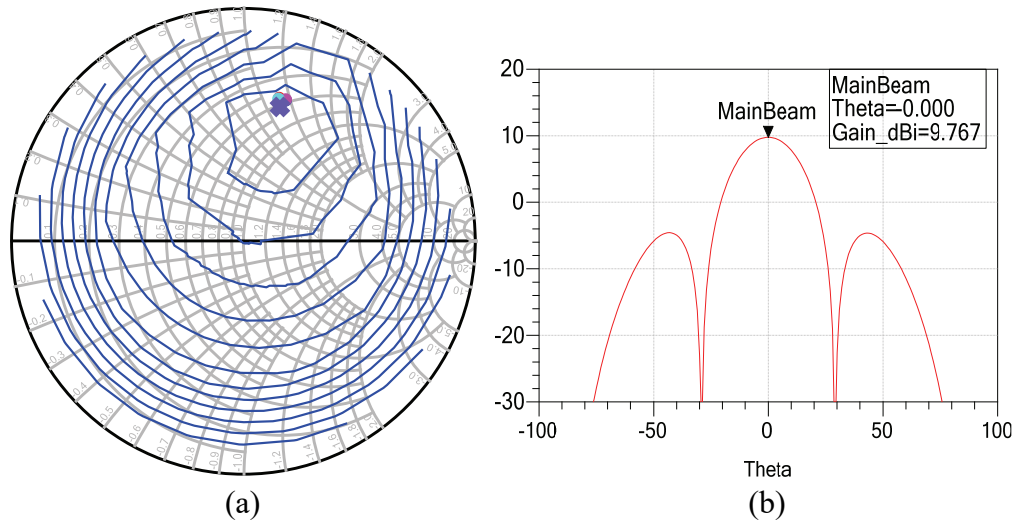


Figure 2.6. (a) Tuned driven element impedances for $\theta_s = 0^\circ$, (b) identically tuned array gain pattern (dBi).

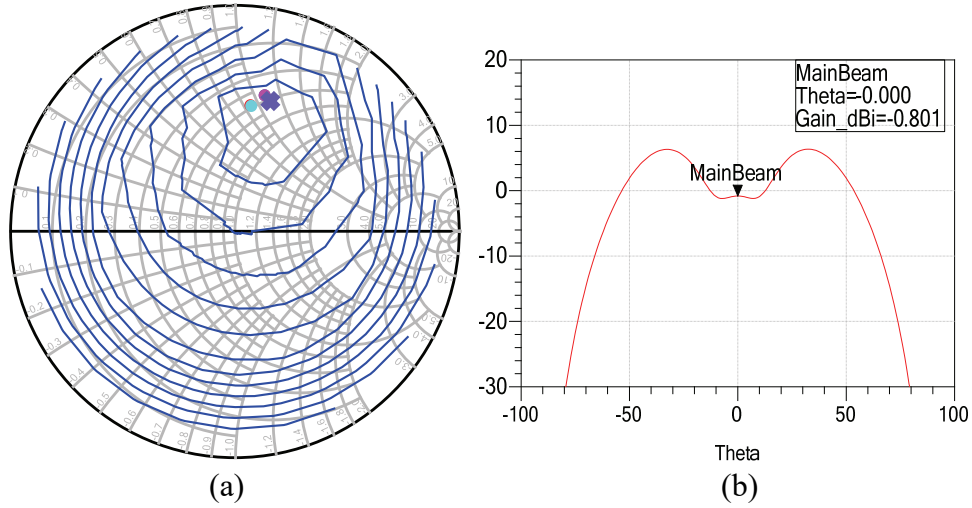


Figure 2.7. (a) Non-identically tuned driven element impedances for $\theta_s = 0^\circ$, (b) Non-identically tuned array gain pattern (dBi).

Table 2.1. Tuner transmission coefficients identically tuned

Element	$ S_{21} $	$\angle S_{21}$
1	0.54	38.78°
2	0.54	38.78°
3	0.54	38.78°
4	0.54	38.78°

Table 2.2. Tuner transmission coefficients non-identically tuned

Element	$ S_{21} $	$\angle S_{21}$
1	0.49	-105.08°
2	0.54	38.78°
3	0.54	38.78°
4	0.49	-105.08°

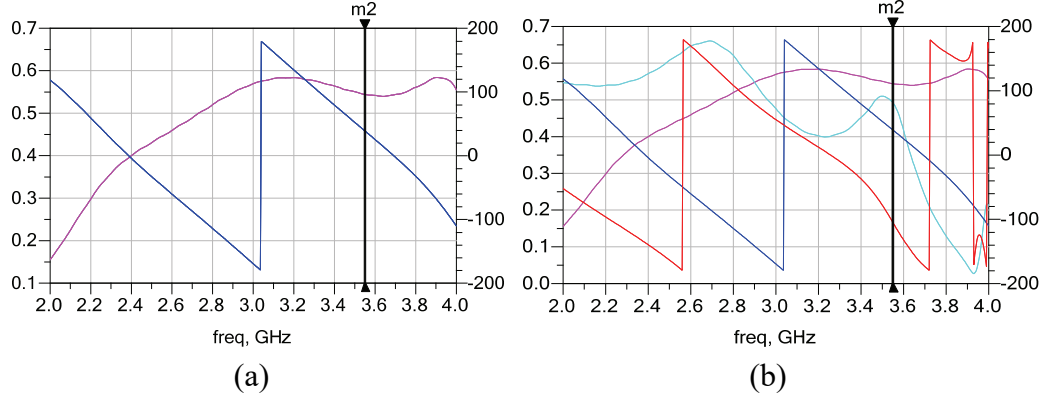


Figure 2.8. (a) Magnitudes (pink, y-axis) and phases (dark blue, right y-axis) of S_{21} of each tuner when tuned with all same switch states, (b) Magnitudes (purple, y-axis) of inner elements, magnitudes (light blue, y-axis) of end elements, phases (dark blue, right y-axis) of inner elements, and phases (red, right y-axis) of S_{21} of each tuner when only inner and outer elements tuned with the same switch states.

When all elements are not identically tuned, the phase progression can be disrupted, and the array pattern shape will be distorted. The same principle applies across all scan angles.

2.2.2 Tuning at Varying Scan Angles

As the array scan angle θ_s deviates from broadside, the mutual coupling effects change, and the initial driven element impedances will also change, as calculated by equation (2.6). Figures 2.9-2.12 show the initial un-tuned driven element impedances and array patterns of the four elements when the array is steered to the scan angles of $\theta_s = -60^\circ, -25^\circ, +10^\circ,$ and $+30^\circ$, respectively. The differences between driven impedances of different elements are greater in these scenarios.

To increase radar detection range capabilities for $\theta_s = +60^\circ$, the driven element impedances from Figure 2.9 must once again be tuned using the algorithm in [44] to provide the maximum output power considering tuner losses. The switched-state stub tuner's load impedance coverage for each of the four scan angles at 3.55 GHz is shown in

Figure 2.13 with the PA maximum-power load impedance. The tuner setting to match the initial driven impedance to the desired PA load impedance while minimizing tuner loss is desired.

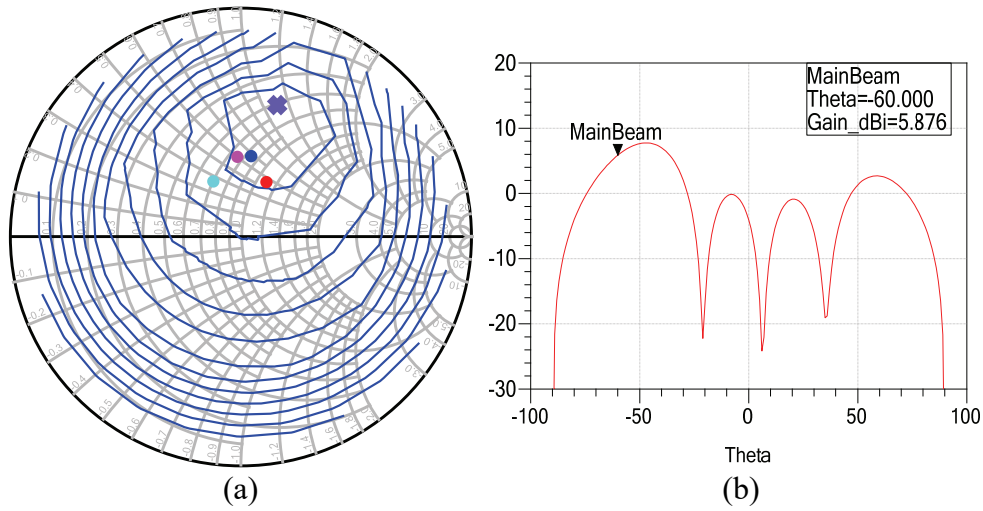


Figure 2.9. (a) Untuned driven element impedances for $\theta_s = -60^\circ$, (b) untuned array pattern (dBi).

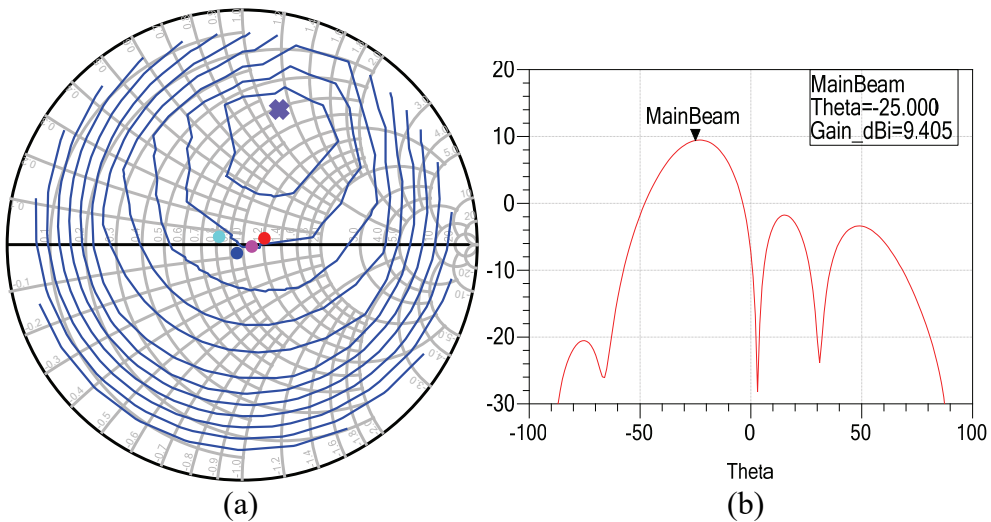


Figure 2.10. (a) Untuned driven element impedances for $\theta_s = -25^\circ$, (b) untuned array pattern (dBi).

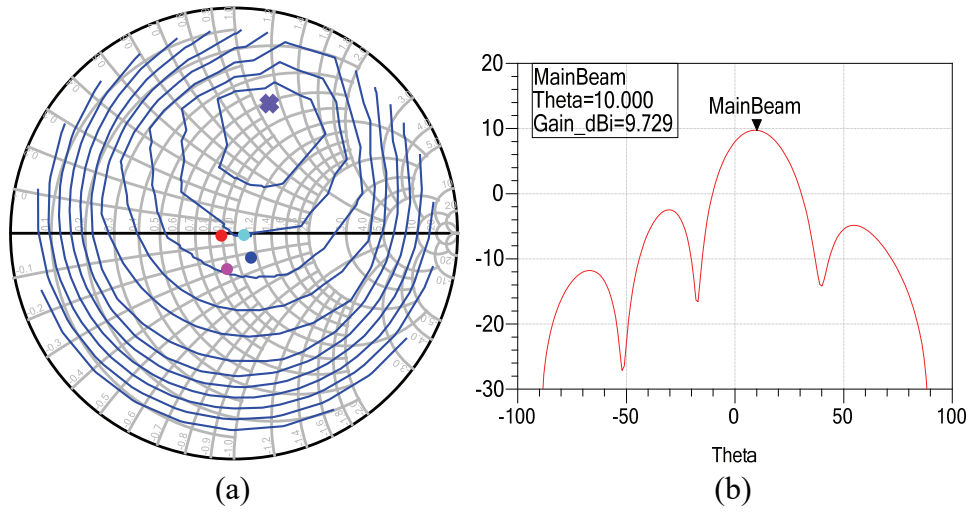


Figure 2.11. (a) Untuned driven element impedances for $\theta_s = +10^\circ$, (b) untuned array pattern (dBi).

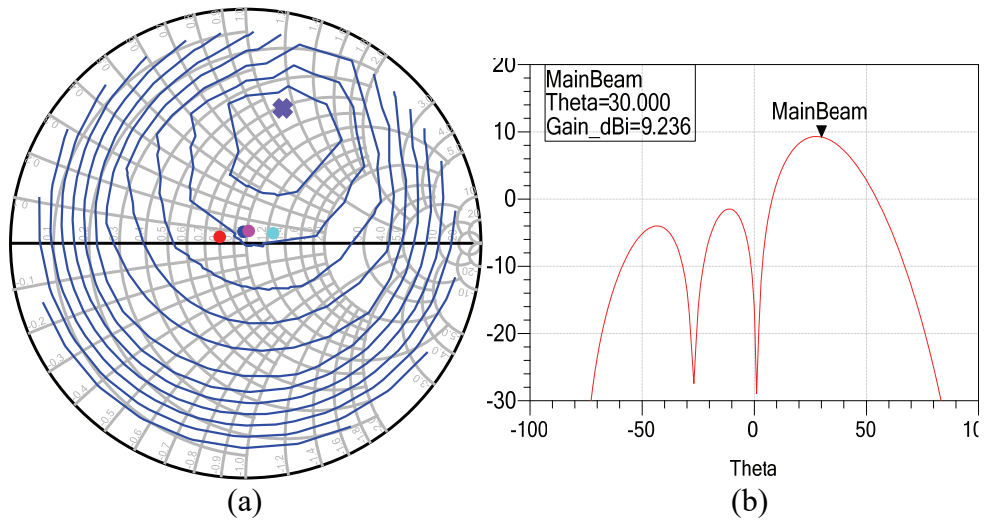


Figure 2.12. (a) Untuned driven element impedances for $\theta_s = +30^\circ$, (b) untuned array pattern (dBi).

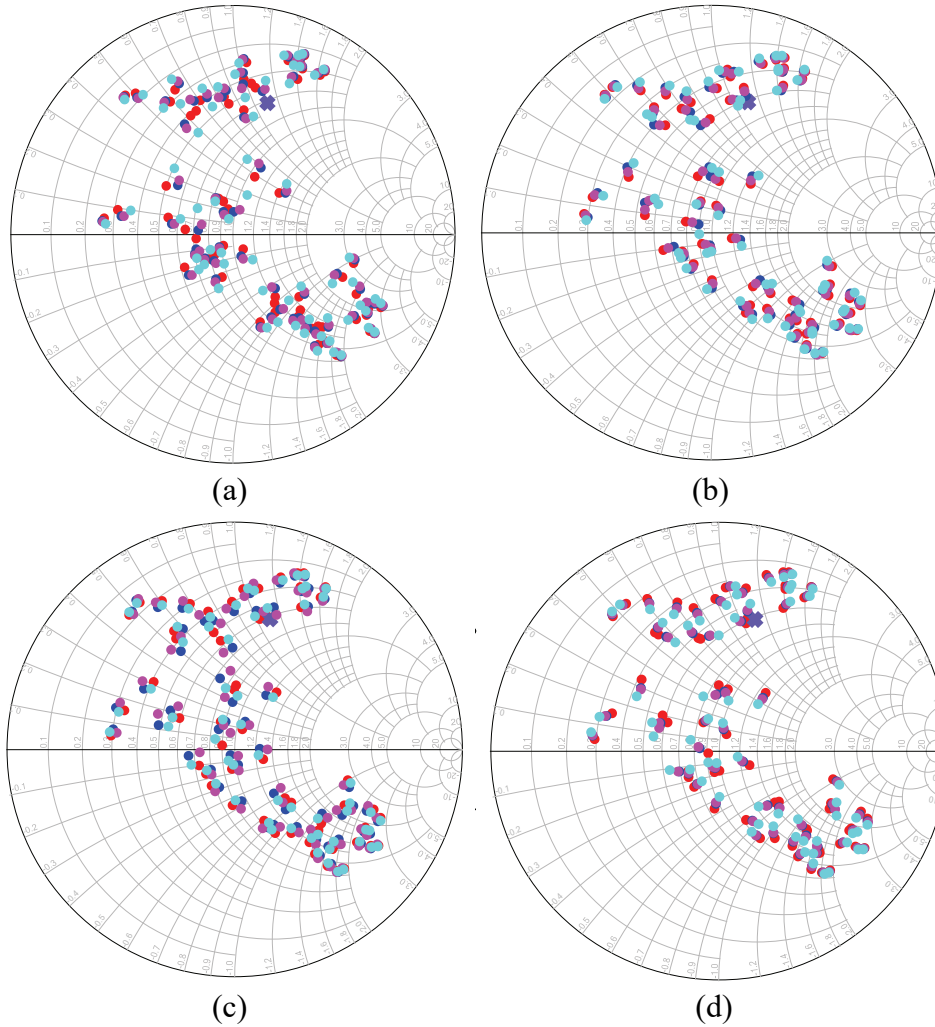


Figure 2.13. (a) Tuner element-wise driven impedance coverages (end elements = light blue and red, inner elements = dark blue and purple) for $\theta_s = -60^\circ$, (b) $\theta_s = -25^\circ$, (c) $\theta_s = +10^\circ$, and (d) $\theta_s = +30^\circ$. The amplifier maximum-power load impedance is labeled with an 'X'.

Implementing the iterative algorithm presented in [44], the switch state 111110 was once again determined to be the optimal switch state for all scan angles. Using this tuner configuration for all scan angles, all driven element impedances were tuned with this switch state on each element to preserve the scan angle and array pattern shape. Calculated range improvements are shown in Table 2.3 for the different scan angles; the improvements range from 18% to nearly 27%. Figures 2.14-2.17 show how well the

switched-state tuners can tune all driven element impedances to the desired PA load impedance at each varying scan angle. The results show the tuners are robust enough to overcome the mutual couplings of the elements at the varying scan angles, regardless of the initial asymmetry of the driven impedances on the Smith Chart. Additionally, the array pattern integrity is preserved, as seen by comparing the tuned patterns (Figures 2.14(b)-2.17(b)) with the untuned patterns (Figures 2.9(b)-2.12(b)), since all elements at each scan angle were tuned using the same switch state. The relative phases of the antenna input signals, therefore, remain the same.

Table 2.3. Achievable Tuned Radar Range Improvement

Scan Angle	Initial Transmit Power	Tuned Transmit Power	Radar Range Improvement
-60°	17.2 dBm	21.9 dBm	+26.5%
-25°	18.6 dBm	21.9 dBm	+21.5%
+10°	19.1 dBm	22.1 dBm	+18.9%
+30°	18.3 dBm	22.0 dBm	+23.7%

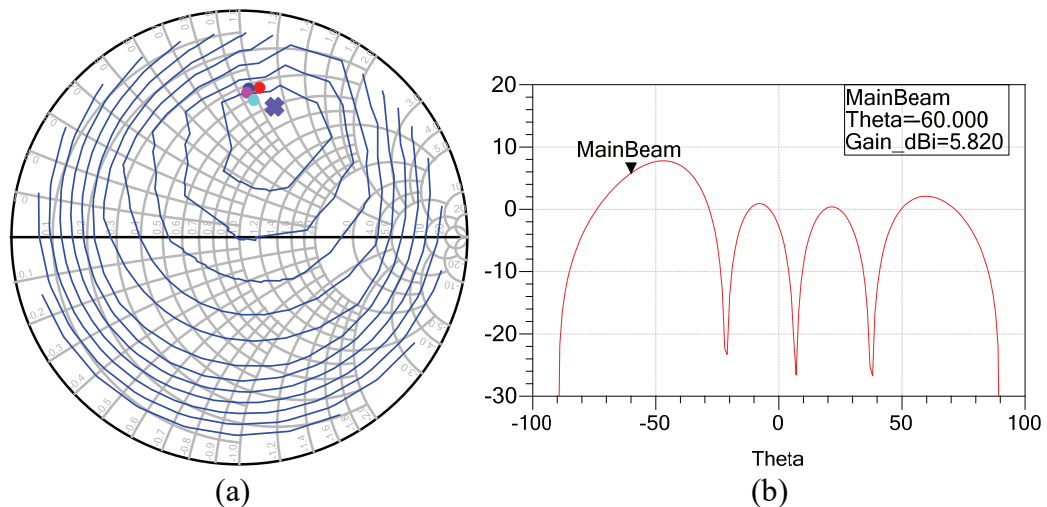


Figure 2.14 (a) Tuned driven element impedances at $\theta_s = -60^\circ$, (b) tuned array gain pattern (dBi).

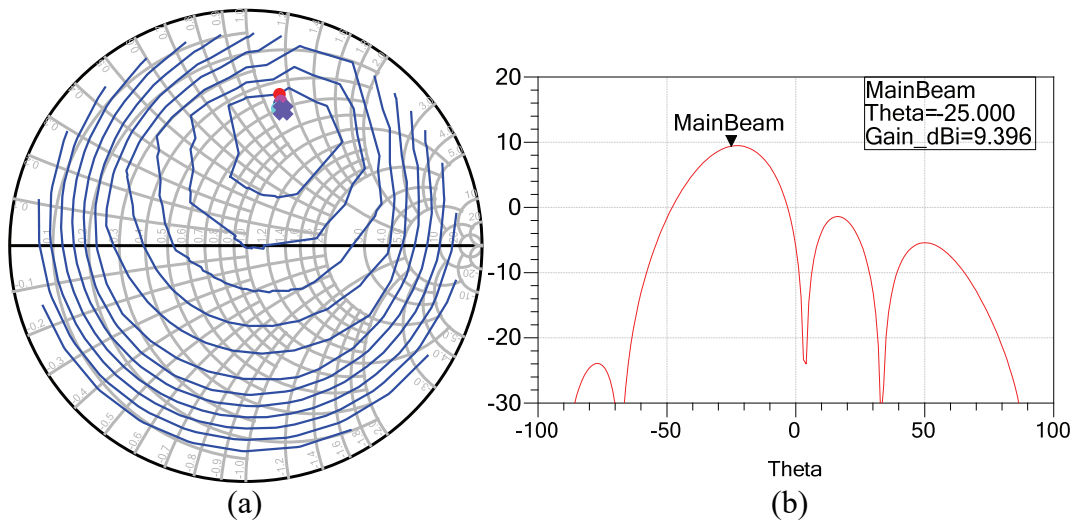


Figure 2.15 (a) Tuned driven element impedances at $\theta_s = -25^\circ$, (b) tuned array pattern (dBi).

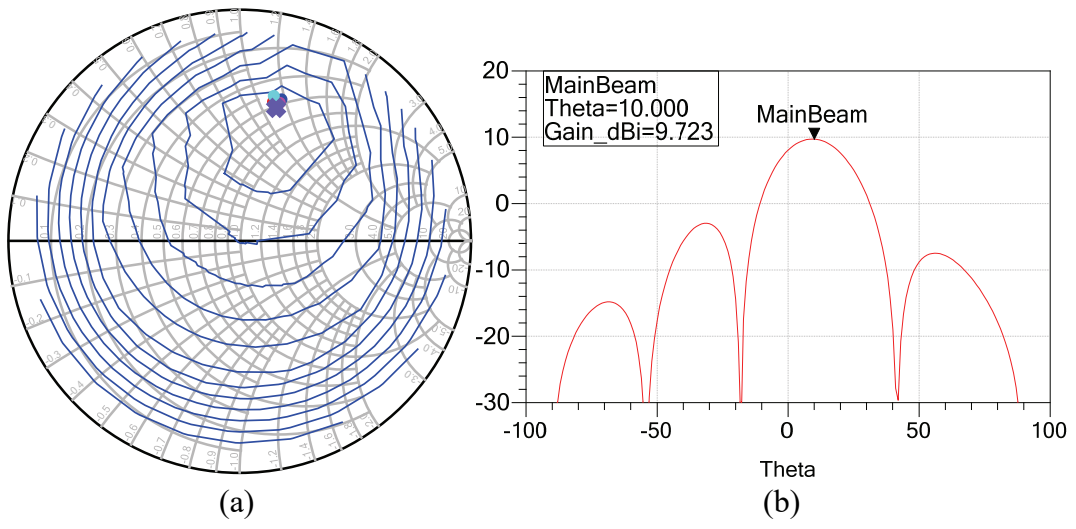


Figure 2.16 (a) Tuned driven element impedances at $\theta_s = +10^\circ$, (b) tuned array pattern (dBi).

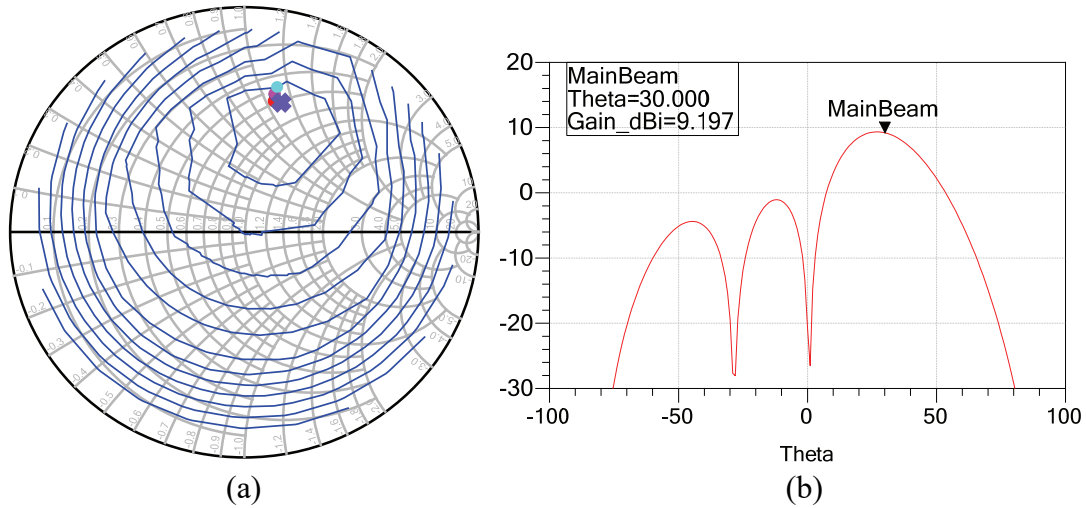


Figure 2.17 (a) Tuned driven element impedances at $\theta_s = +30^\circ$, (b) tuned array pattern (dBi).

2.3 Summary

The effects of impedance tuning in the individual elements of a phased array transmitter on detection range capabilities have been demonstrated in a joint circuit and electromagnetic simulation platform. For an EM simulation of four-element, $\lambda/2$ spaced, microstrip linear array, an increase in output power and calculated radar range is achieved through element-wise impedance tuning. Simulation comparison of the tuned array to an un-tuned array results in calculated radar range increases of over 12 percent, and often over 20 percent for some scan angles. While the output power is increased significantly, very little effect on the relative transmission array pattern is observed if the individual elements are tuned identically, because identical tuning preserves the relative magnitude ratios and phase shifts of the element antenna currents. This experiment demonstrates the potential benefits obtainable by placing real-time impedance tuning in the elements of phased array transmitters for radar, with the results extending to fifth-generation (5G) directional wireless communication applications utilizing phased arrays.

CHAPTER THREE

Dual-Beam Phased Array Impedance Tuning for Spurious Beam Suppression

Dual-beam wireless transmissions are often performed from phased-array systems to allow simultaneous transmission of radar and communications signals in different directions [2]. Multi-beam transmissions rely on spatial diversity to avoid interference and allow frequencies to be shared by more than one user, easing the strain on the frequency spectrum. Nonlinearities in the power amplifiers (PAs) of the transmit elements, however, cause unwanted spatial intermodulation beams, or “beat beams”, to be transmitted [6]-[7]. Hemmi describes combined spatial and frequency intermodulation products from a dual-beam, dual-tone transmission [8], later discussed by Haupt [9]. Mollen uses Volterra and Hermite PA modeling approaches to calculate intermodulation beams [10]. Experimental measurement demonstration of intermodulation array products is provided by Zaghloul for a Ku-band array [11]. Loyka discusses modeling and simulation techniques related to active array performance and suggests the instantaneous quadrature technique to capture circuit nonlinearities and their effects on array performance [12]. Obermier discusses an approach to assess the effects of spatial intermodulation on the antenna array factor, and to adjust the input power needed to maximize the equivalent isotropic radiated power (EIRP) [13]. While the specific problem of transmitter beam intermodulation is considered, Kaho describes an intermodulation beam phenomenon that can occur based on single-beam transmission of two different carrier frequencies, and demonstrates a method of improving the

intermodulation beams by adjusting the carrier to intermodulation power ratio of the PA [14]. Further, intermodulation issues in receive arrays and potential solutions are discussed and demonstrated by Rupakula [15].

The first consideration of impedance tuning as a strategy for spatial intermodulation beat beam mitigation is presented. Recent demonstrations of high-power reconfigurable matching circuits for radar [43, 59] make practical the application of real-time impedance tuning to minimization of spatial intermodulation products in a dual-beam RadCom shared-frequency transmission system. Since impedance tuning impacts both the gain and linearity of the PA, the approach presented can deal with the undesirable beat-beam artifacts of the amplifier nonlinearities while also maximizing element amplifier gain, a combined task that most waveform engineering and predistortion techniques alone cannot accomplish. Various works in the literature deal with linearity issues, mitigating the undesirable beat beams through waveform engineering, orthogonal phase distribution selection, and an amplifier-modeling based approach [16]-[21]. Braithwaite describes a predistortion approach to mitigate the unwanted intermodulation beams [22]. While impedance tuning has been demonstrated as a solution for real-time control of spectral intermodulation products for coexistence [4], the first demonstration of using impedance tuning to control spatial intermodulation products is presented. A co-simulation technique is utilized with circuit and electromagnetic (EM) simulators to compute the effect on array performance from nonlinearities in the amplifier. A comparison of the results of this technique is also made to a recently demonstrated predistortion method [22] to show that impedance tuning is

much more effective at obtaining the desired beam pattern while maximizing element PA gain.

3.1 Spatial Intermodulation Theory

Consider a dual-beam, radar/communications (RadCom) shared-frequency transmission block diagram as shown in Figure 3.1.

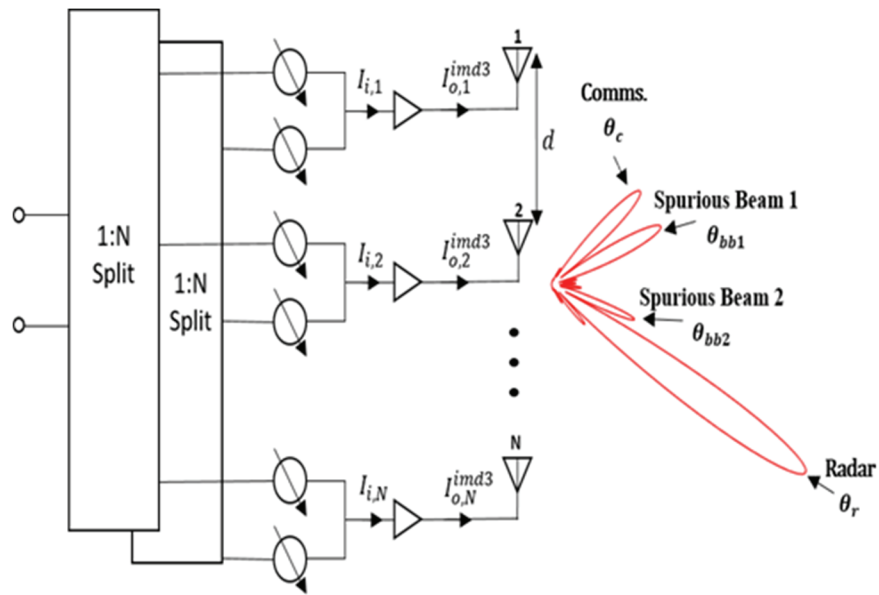


Figure 3.1. Dual-beam, dual-signal, shared-frequency phased array RadCom block diagram.

Both beams share the same frequency ω_0 . The radar and communications input signals are added together at each power amplifier [8] after applying the appropriate phase shifts to steer the two beams. The signal phasor sent into the n th element at frequency ω_0 is represented by

$$I_{i,n} = I_{r_n} + I_{c_n} = A_{r_n} e^{-jn\alpha_r} + A_{c_n} e^{-jn\alpha_c}, \quad (3.1)$$

where A_{r_n} and A_{c_n} are the amplitude of the radar and communications signals fed into the n th element, respectively, and α_r and α_c represent the phase shifts needed to steer the radar beam and communications beam to the desired directions, respectively. For array steering, $\alpha_r = k_0 d \sin(\theta_r)$, $\alpha_c = k_0 d \sin(\theta_c)$, where θ_r and θ_c represent the desired elevation steering directions for the radar and communications beams respectively, d is the antenna element spacing, and $k_0 = 2\pi/\lambda_0$. For a simplified mathematical discussion, if a power amplifier (PA) can be described as having a third-order nonlinearity, the amplifier input-output relationship at the n th element in the array [45] is described by

$$I_{o,n}^{imd3} = \beta_1 I_{i,n} + \beta_2 I_{i,n}^2 + \beta_3 I_{i,n}^3. \quad (3.2)$$

From applying (3.1) to (3.2), the power-amplifier output phasor representation of the content at ω_0 is given by

$$\begin{aligned} I_{o,n}^{imd3} = & A_{r_n} \left(\beta_1 + \frac{5}{4} \beta_3 A_{r_n}^2 + \beta_3 A_{c_n}^2 \right) e^{-jn\alpha_r} \\ & + A_{c_n} \left(\beta_1 + \frac{5}{4} \beta_3 A_{c_n}^2 + \beta_3 A_{r_n}^2 \right) e^{-jn\alpha_c} \\ & + \frac{1}{2} \beta_3 A_{r_n}^2 A_{c_n} e^{-jn(2\alpha_r - \alpha_c)} \\ & + \frac{1}{2} \beta_3 A_{r_n} A_{c_n}^2 e^{-jn(2\alpha_c - \alpha_r)}. \end{aligned} \quad (3.3)$$

Here only the fundamental frequency terms ω_0 are shown, since unwanted content at the harmonic terms $2\omega_0$ and $3\omega_0$ can be more easily removed. Since this is a shared-frequency system, the intermodulation products (IM) only occur at the fundamental frequency ω_0 . The β_3 term in (3.3) is a parameter that models the gain compression of the PA and is typically modeled as a negative number [45]. This term describes the generation of third-order nonlinearities that appear in the output signal of the PA. With a

negative β_3 term, as is the case when a compressed PA is connected to the individual antenna elements [45], the amplitude of the phasor signal is reduced indicating that some power is lost at the fundamental frequency ω_0 to third-order IM distortion (IMD3).

As the PA phasor output signal (3.3) is fed to the individual antenna elements in the array, so too are the IMD3 products, causing distortion in the far-field array pattern. The far-field array factor determines the output beam pattern of the phased array. In a uniform linear array (ULA) consisting of N antenna elements as shown in Figure 3.2, the array factor is derived by the relative positions and spacings of the antenna elements and the direction of wave propagation caused by the individual element excitations.

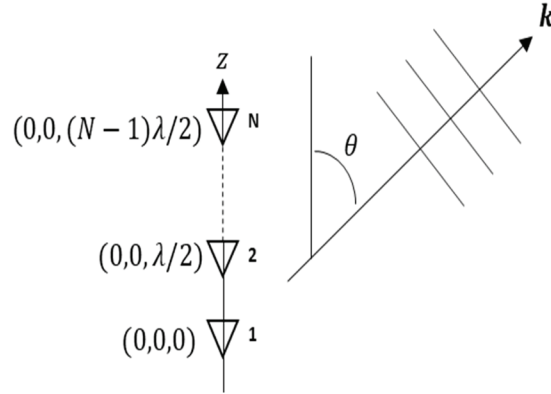


Figure 3.2. Array of N elements placed along z -axis separated in distance by $\lambda/2$.

Each n th antenna element is located at a position given by $\mathbf{r}_n = (x_n, y_n, z_n)$, and the wave propagation vector is given by, $\mathbf{k} = k_0(\sin\theta\cos\phi\hat{x} + \sin\theta\sin\phi\hat{y} + \cos\theta\hat{z})$. Since each element is excited with the PA output signal described by (3.3), the array factor is the spatial Fourier Transform in the far-field of the phasor excitation signals fed to the radiating antenna elements,

$$AF(\theta) = \sum_{n=1}^N I_{o,n}^{imd3} e^{j\mathbf{k}\cdot\mathbf{r}_n}. \quad (3.4)$$

Expanding this array factor in (3.4) yields the IMD3 array factor radiating superposition given by:

$$\begin{aligned}
AF(\theta)_{imd3} = & \sum_{n=0}^{N-1} A_{r_n} \left(\beta_1 + \frac{5}{4} \beta_3 A_{r_n}^2 + \beta_3 A_{c_n}^2 \right) e^{j(n[k_0 d \sin(\theta) - \alpha_r])} \\
& + \sum_{n=0}^{N-1} A_{c_n} \left(\beta_1 + \frac{5}{4} \beta_3 A_{c_n}^2 + \beta_3 A_{r_n}^2 \right) e^{j(n[k_0 d \sin(\theta) - \alpha_c])} \\
& + \sum_{n=0}^{N-1} \frac{1}{2} \beta_3 A_{r_n}^2 A_{c_n} e^{j(n[k_0 d \sin(\theta) - (2\alpha_c - \alpha_r)])} \\
& + \sum_{n=0}^{N-1} \frac{1}{2} \beta_3 A_{r_n} A_{c_n}^2 e^{j(n[k_0 d \sin(\theta) - (2\alpha_r - \alpha_c)])} , \tag{3.5}
\end{aligned}$$

The resulting array pattern at frequency ω_0 will have four large-magnitude beams: two intentional main beams at θ_r and θ_c and two spurious spatial intermodulation beams at θ_{bb1} and θ_{bb2} . These spurious beam locations are derived as follows from (3.5):

$$\alpha_{bb1} = 2\alpha_c - \alpha_r, \alpha_{bb2} = 2\alpha_r - \alpha_c, \tag{3.6}$$

$$\theta_{bb1} = \sin^{-1} \left(-\frac{\alpha_{bb1}}{k_0 d} \right), \theta_{bb2} = \sin^{-1} \left(-\frac{\alpha_{bb2}}{k_0 d} \right), \tag{3.7}$$

The quantities in (3.6) describe the IMD3 phase distortions caused by the PA nonlinearities at the fundamental frequency ω_0 to the antenna feed signals. Equation (3.7) calculates the directions in which these unintended spurious beams are transmitted in the far-field. Figures 3.3-3.5 show the theoretical elevation antenna pattern of a 64-element $\lambda/2$ -spaced linear array for several RadCom direction combinations with and without the calculated third-order power amplifier nonlinearities calculated from (3.5) and plotted using Matlab. Without the PA, there is no nonlinearity present, and the constant β_3 term is set to 0. Without the intermodulation terms in (3.5), the array factor

contains only the intended radar and communication beam terms. In Figures 3.3-3.5, the array patterns without the PA show pronounced transmission beams only at θ_r and θ_c .

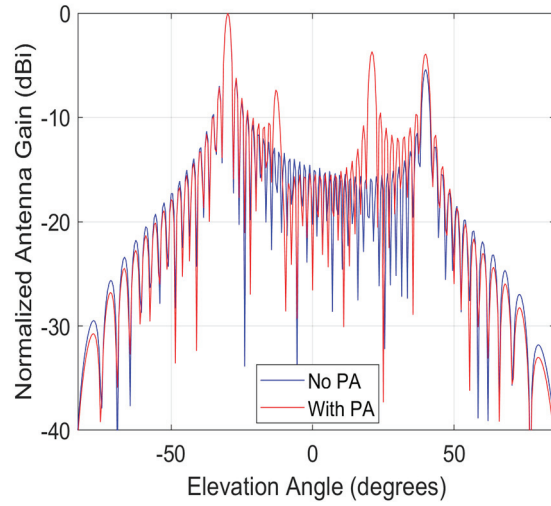


Figure 3.3. Normalized theoretical elevation dual-beam array pattern (dBi): $\theta_r = -30^\circ$, $\theta_c = +40^\circ$, calculated $\theta_{bb1} = -12^\circ$, calculated $\theta_{bb2} = +21^\circ$.

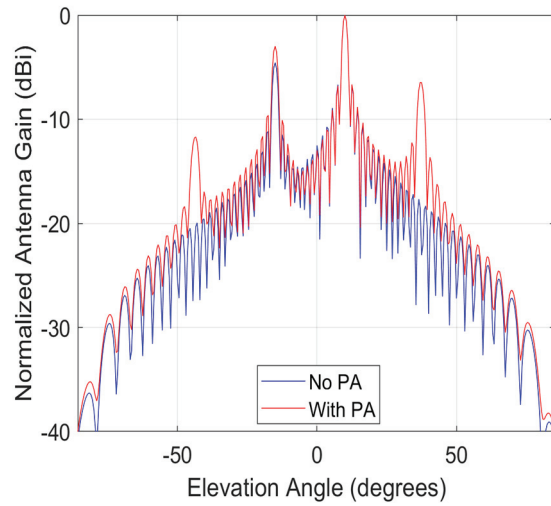


Figure 3.4. Normalized theoretical elevation dual-beam array pattern (dBi): $\theta_r = +10^\circ$, $\theta_c = -15^\circ$, calculated $\theta_{bb1} = -44^\circ$, calculated $\theta_{bb2} = +37^\circ$.

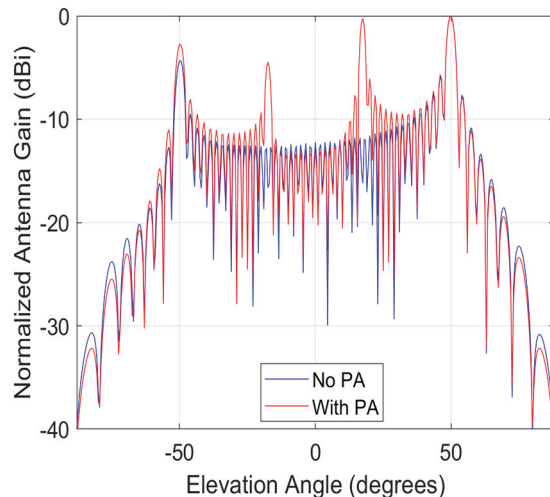


Figure 3.5. Normalized theoretical elevation multi-beam antenna pattern: $\theta_r = +50^\circ$, $\theta_c = -50^\circ$, calculated $\theta_{bb1} = -17^\circ$, calculated $\theta_{bb2} = +17^\circ$.

When the IMD3 artifacts are ignored, the antenna array transmits the two intended main beams at their respective elevation locations. When the IMD3 artifacts are included, however, two additional undesired beams are transmitted. In Figure 3.3, the elevation angles of the radar and communications beams are $\theta_r = -30^\circ$ and $\theta_c = +40^\circ$, respectively. From (3.7), the spurious beams resulting from IMD3 are calculated to be at $\theta_{bb1} = -12^\circ$ and $\theta_{bb2} = +21^\circ$. The plot of the array pattern with the PAs present shows new beam presence at these angles. The theory was similarly verified in the RadCom scenarios of Figures 3.4 and 3.5, with new beams visible at θ_{bb1} and θ_{bb2} . All plots showed the theoretical results of a 64-element $\lambda/2$ -spaced ULA which showed pronounced spurious beams at the expected directions, as calculated by equation (3.7). When more elements are used, the spurious beams become more pronounced, since more elements provide sharper resolution due to increased far-field spatial sampling described by equation (3.4). When fewer antenna elements are used, the spurious beams are less

pronounced, and may be fused into the adjacent sidelobes in the array pattern due to imprecise far-field spatial sampling.

3.2 Spatial Intermodulation Suppression

To view and correct the issue of spatial intermodulation in a more realistic setting, a joint circuit and electromagnetic (EM) simulation platform was used. Using the Advanced Design System software (ADS) and ADS Momentum EM simulator from Keysight Technologies, a schematic was generated with an array of 16 $\lambda/2$ -spaced microstrip patch antenna elements. The elements were designed using Rogers RO4003C substrate at the design frequency of 3.55 GHz, to lie within the 3.55-3.7 GHz radar band, presently allocated for spectrum sharing between radar and communications. As in the system block diagram of Figure 3.1, the antenna array is fed using two signal sources: one for the radar signal and another for the communications signal. These sources are connected to two 1:16 power splitters that feed into phase shifters according to the desired direction of the subsequent RadCom beams. The phase-shifted signals are then combined as input to the individual power amplifiers, which then feed into the individual microstrip antenna elements. Each of the 16 power amplifier devices used was a nonlinear MWT-173 Gallium Arsenide (GaAs) metal-semiconductor field-effect transistor (MESFET) nonlinear transistor model from Modelithics, biased at $V_{DS} = 4.5$ V and $V_{GS} = -1.5$ V. For the MESFETs, an output power vs. input power plot at a 50Ω load impedance was generated to assess the linear and nonlinear operating ranges of the PA device. Figure 3.6 shows these results and indicates that the input 1-dB compression point (P1dB) $P_{in,1dB} = 14$ dBm for this type of amplifier results in an output power of 20.07 dBm. Driving the device beyond P1dB results in gain reduction and nonlinear

behavior with third-order intermodulation distortion, simply modeled by the previously described equation (3.3). Ofcourse, this compression characteristic will vary as the load impedance is tuned.

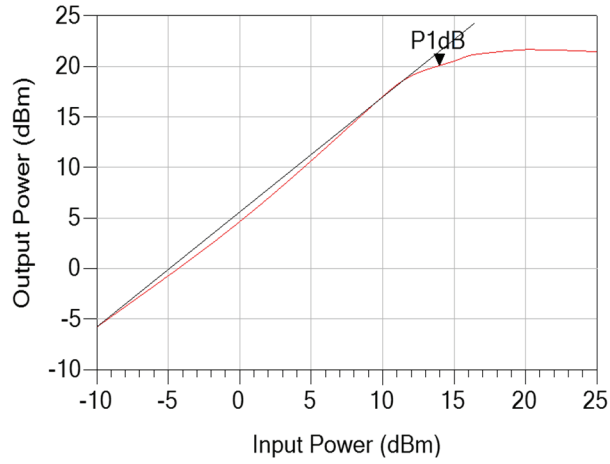


Figure 3.6. Input Power vs. Output Power for MWT-173 transistor at 3.55 GHz.

As discussed in the previous section, the radar and communication excitations are fed into the individual antenna elements as given by (3.1), and the nonlinear power amplifiers cause unwanted IMD3 artifacts at the operating frequency ω_0 as given by (3.3) that translate into the unwanted beat beams. To remove the beat beams, the PA outputs must be modified to reverse the IMD3 artifacts and produce an output as close to (3.1) as possible. This can be accomplished by multiplying the IMD3 PA phasor output signal $I_{o,n}^{imd3'}$ of (3.3) by an IMD3 reversal factor κ_n shown as follows, such that it can be modified to resemble the linear phasor signal excitation at the PA input:

$$\begin{aligned}
 I_{in} &= I_{o,n}^{imd3'} \cdot \kappa_n \\
 \kappa_n &= \frac{I_{i,n}}{I_{o,n}^{imd3'}} \cdot
 \end{aligned}
 \tag{3.7}$$

The IMD3 reversal factor κ_n is a phasor ratio of the n -th linear PA phasor input source excitation to the n -th IMD3 PA phasor output excitation to reverse the effect of the IMD3 phasor excitation fed to the array elements. The bottom line in this technique is that it attempts to ensure that all amplifier phasor outputs are complex constant multiples of their inputs. If the amplifier output phasors are related to each other in the same way in amplitude and phase as the original signals, then the array factor and far-field pattern will be identical to the intended pattern. In such case, the array factor from the optimized-amplifier aperture, $AF_{corrected}(\theta)$ will contain only terms resulting from α_r and α_c terms at element, each modified by the complex multiplier $1/\kappa_n$:

$$AF_{corrected}(\theta) = \sum_{n=0}^{N-1} \frac{1}{|\kappa_n|} A_{r_n} e^{j(n[k_0 d \sin(\theta) - (\alpha_r + \angle \kappa_n)])} + \sum_{n=0}^{N-1} \frac{1}{|\kappa_n|} A_{c_n} e^{j(n[k_0 d \sin(\theta) - (\alpha_c + \angle \kappa_n)])} \quad (3.8)$$

If the κ_n are all the same, then the AF will be undistorted, and the spurious beams are eliminated. Optimization should therefore be performed of the PAs to obtain all κ_n phasor values equal in magnitude and phase. In this case, the corrected feed excitation sent to the antenna will resemble the linear phasor excitation shown in (3.1), which does not cause spurious transmissions in the array pattern, and only the two intended RadCom beams will be transmitted.

To construct a procedure that allows this IMD3 spatial distortion to be reversed in real time, reconfigurable impedance tuners are placed between each PA and antenna element as shown in Figure 3.7. This reconfigurable matching network changes the phasor signal that is fed to the single antenna element from $I_{o,n}^{imd3}$ to $I_{o,n}^{imd3'}$. A

reconfigurable matching network in each element between the PA device and antenna can intelligently tune each individual feed phasor signal $I_{o,n}^{imd3'}$ in real-time to obtain identical values of κ_n across the elements, reversing the IMD3 effects on the array pattern. Figure 3.8 shows this concept for the entire array. In the dual-beam scenario, equation (3.1) shows that each PA will be driven with a different input power level, causing the linearity of the PAs in the different elements to vary. At these different drive levels, the gain and IMD3 levels will also vary significantly.

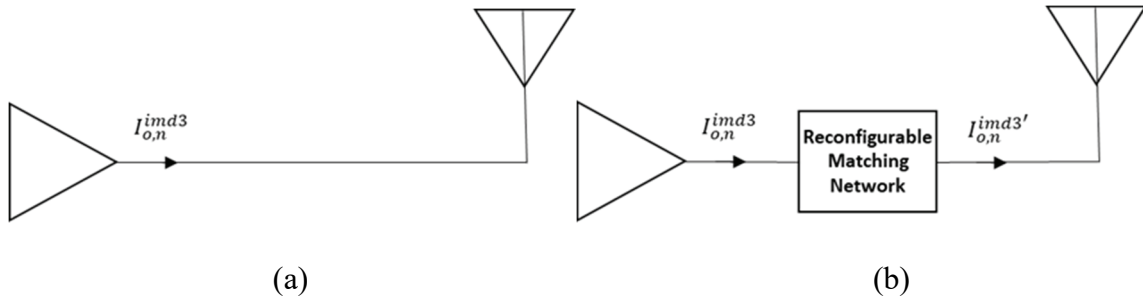


Figure 3.7. (a) Antenna feed without matching network, (b) antenna feed with reconfigurable matching network.

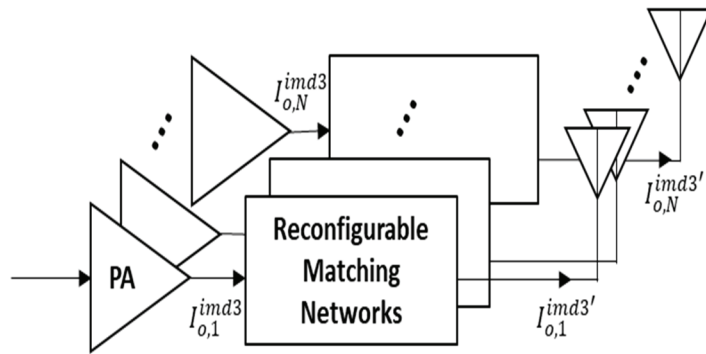


Figure 3.8. Block diagram of element-wise matching networks.

To demonstrate a real-time impedance tuning approach using the ADS/Momentum co-simulation platform a model of an evanescent-mode cavity impedance tuner designed by Semnani [59] is placed between each of the 16 PA nonlinear transistor models and each of the 16 antenna elements in the ADS simulator. Figure 3.9 shows the wide Smith Chart coverage of the impedance tuner model at 3.55 GHz, the frequency at which these experiments are performed.

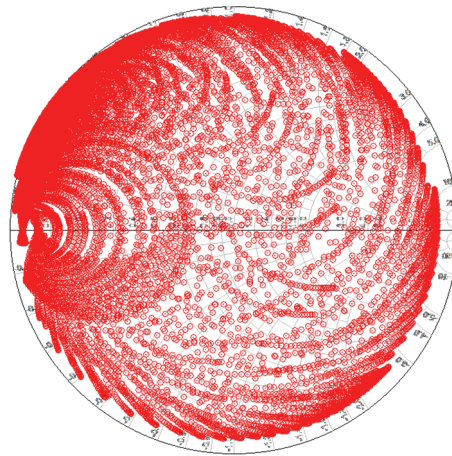


Figure 3.9. Impedance tuner Smith Chart Coverage at 3.55 GHz.

The simulation was constructed to provide 18.88 dBm available input power to the radar component and 16.19 dBm available input power to the communication component at each PA. This results in a total maximum available power of 20.75 dBm to the first element, where the radar and communications excitation components are in phase. The overall available power level of each PA varies with the relative phases of the radar and communication inputs. No input matching network design was performed for this simple experiment, so the input power values measured in the circuit schematic, representing the power delivered to the network, often are visibly lower than the available power values for those elements. A gradient descent optimization was applied directly in

the ADS optimizer tool to tune the reconfigurable capacitors, modeling the resonator discs, in each tuner. The simulation optimizer is given two goals: minimizing the standard deviation of the κ_n phasor quantities, as defined by (3.7), and minimizing the individual magnitudes of the κ_n phasor quantities. Minimizing κ_n standard deviation ensures all phasor quantities are as identical as possible to restore the ideal array pattern. Minimizing $|\kappa_n|$ maximizes the amplifier gain and output power. The simulation was performed for three different RadCom beam direction combinations.

3.2.1 RadCom Directions: $\theta_r = -30^\circ$ and $\theta_c = +40^\circ$

Following the optimizations in the ADS/Momentum simulator, the resulting elevation array pattern was compared with the unoptimized pattern. For the first combination of radar and communications transmission directions ($\theta_r = -30^\circ$ and $\theta_c = +40^\circ$), the ideal array pattern with no PA device connected, possessing no IMD3 and therefore providing only linear phasor excitations (3.1), is shown in Figure 3.10.

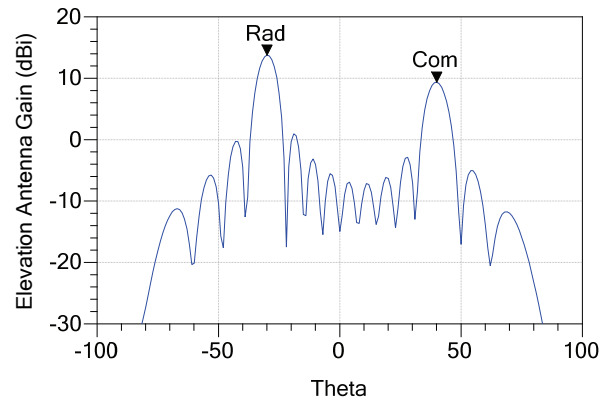


Figure 3.10. Ideal elevation array pattern (dBi) without PAs: $\theta_r = -30^\circ$, $\theta_c = +40^\circ$.

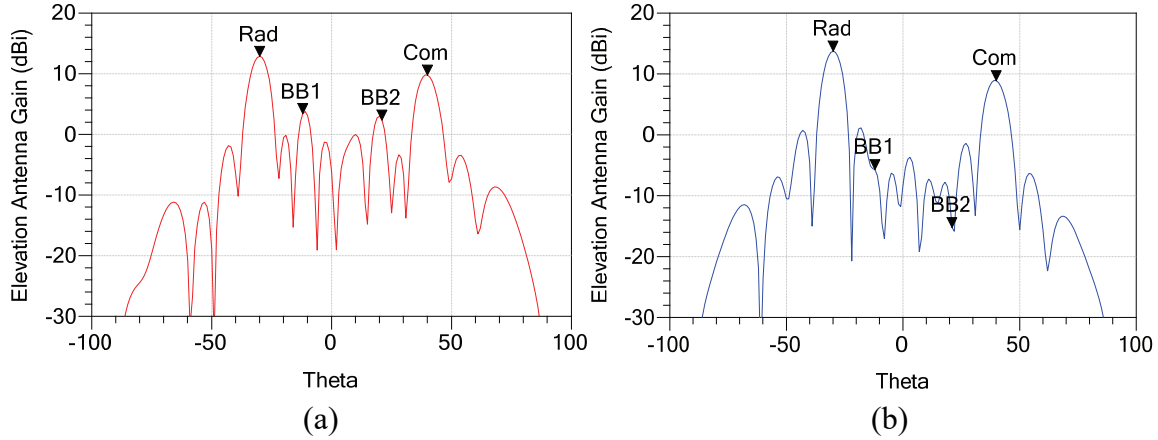


Figure 3.11. (a) Elevation array pattern with un-tuned PA outputs: $\theta_r = -30^\circ$, $\theta_c = +40^\circ$, calculated $\theta_{bb1} = -12^\circ$, calculated $\theta_{bb2} = +21^\circ$, (b) elevation array pattern with tuned PA outputs: $\theta_r = -30^\circ$ and $\theta_c = +40^\circ$. $\theta_{bb1} = -12^\circ$ and $\theta_{bb2} = +21^\circ$ suppressed.

The ideal linear excitations cause the dual-beam array to transmit only two intended beams in the far-field for both radar and communications as expected. The magnitude of the radar beam at $\theta_r = -30^\circ$ is 13.77 dBi and the magnitude of the communications beam at $\theta_c = +40^\circ$ is 9.36 dBi. When a PA is connected to each antenna element, the IMD3 phasor signals (3.3) cause two additional undesired beams to be transmitted in the far-field as expected. The PA nonlinearities additionally distort the magnitude of the intended RadCom beams since some of the power is now re-allocated to the two spurious beams. The IMD3 array pattern in Figure 3.11(a) shows that the magnitude of the radar beam at $\theta_r = -30^\circ$ is now 12.87 dBi, the magnitude of the communications beam at $\theta_c = +40^\circ$ is now 9.77 dBi. Additionally, the two spurious beat beams are visible: the magnitude of the beat beam at $\theta_{bb1} = -12^\circ$ is 3.44 dBi, and the magnitude of the beat beam at $\theta_{bb2} = +21^\circ$ is 2.37 dBi. Figure 3.11(b) shows the far-field array pattern that is transmitted following the impedance tuning optimization, minimizing the size and vector standard deviation of κ_n . The optimized array pattern of

Figure 3.11(b), with impedance tuning applied, more closely resembles the ideal array pattern of Figure 3.10. After impedance tuning, the magnitude of the radar beam at $\theta_r = -30^\circ$ is 13.76 dBi, the magnitude of the communications beam at $\theta_c = +40^\circ$ is 8.91 dBi, the magnitude of the first beat beam at $\theta_{bb1} = -12^\circ$ is -5.70 dBi, and the magnitude of the second beat beam at $\theta_{bb2} = +21^\circ$ is -15.23 dBi, indicating spurious beam suppression and a close restoration of the intended array pattern shape.

Tables 3.1-3.3 provide a comparison of the main and beat beam antenna gain magnitudes for the ideal (no PA), untuned, and optimized cases, respectively. Each input power value shown in the tables represents the power delivered to the transistor by the source. As such, the gain represents the operating power gain, which is the power delivered to the load relative to the power delivered to the transistor input. Table 3.2 shows an analysis of the κ_n IMD3 reversal factor element-wise magnitudes and phases. Since these κ_n values are significantly different in both magnitude and phase, the array element phasor excitations are different from the ideal excitations, causing far-field array pattern distortion, as shown in Figure 3.11(a). The un-tuned $|\kappa_n|$ standard deviation is 0.13 and the un-tuned $\angle\kappa_n$ standard deviation is 10.59° . Impedance tuning can be implemented to lower the standard deviations of $|\kappa_n|$ and $\angle\kappa_n$, indicating that the effects of the IMD3 phasor excitations have been reversed before they are fed to the antenna elements. From Table 3.3, $|\kappa_n|$ and $\angle\kappa_n$ are now much closer in value than the un-tuned values of Table 3.2. Following impedance tuning, the $|\kappa_n|$ standard deviation is reduced to 0.07 and the $\angle\kappa_n$ standard deviation is reduced to 6.43° . This results in an array pattern in Figure 3.11(b) that more closely resembles the array pattern in Figure 3.10.

Table 3.1. Comparison of Array Gain (dBi) for $\theta_r = -30^\circ$ and $\theta_c = +40^\circ$

Array Pattern Case	Gain at θ_r (dBi)	Gain at θ_c (dBi)	Gain at θ_{bb1} (dBi)	Gain at θ_{bb2} (dBi)
Ideal	13.77	9.36	--	--
IMD3	12.87	9.77	3.44	2.37
Tuned	13.76	8.91	-5.70	-15.23

Table 3.2. Untuned κ_n values for $\theta_r = -30^\circ$ and $\theta_c = +40^\circ$

Element	$ \kappa_n $	$\angle\kappa_n(^{\circ})$	Input Power (dBm)	Output Power (dBm)	PA Gain (dB)
1	0.29	-110.50	17.29	23.22	5.93
2	0.69	-102.07	7.54	4.93	-2.61
3	0.49	-95.38	16.99	18.34	1.34
4	0.52	-93.29	13.99	14.55	0.56
5	0.44	-94.25	13.95	14.83	0.88
6	0.29	-145.83	15.90	21.78	5.87
7	0.55	-88.88	7.80	10.28	2.48
8	0.29	-113.10	17.23	23.12	5.88
9	0.91	-80.46	7.64	3.47	-4.18
10	0.25	-139.93	15.86	22.98	7.13
11	0.54	-92.97	13.90	13.52	-0.39
12	0.49	-103.61	14.19	14.28	0.09
13	0.22	-154.00	15.69	14.40	8.71
14	0.53	-90.25	7.77	10.89	3.12
15	0.29	-112.06	17.24	23.04	5.81
16	0.63	-94.72	7.28	5.98	-1.30

Table 3.3. Tuned κ_n values for $\theta_r = -30^\circ$ and $\theta_c = +40^\circ$

Element	$ \kappa_n $	$\angle\kappa_n(^{\circ})$	Input Power (dBm)	Output Power (dBm)	PA Gain (dB)
1	0.47	-81.54	18.10	24.07	5.97
2	0.59	-65.68	8.34	15.45	7.11
3	0.44	-79.77	17.40	24.11	6.71
4	0.45	-75.82	14.55	22.14	7.58
5	0.45	-73.84	14.65	22.62	7.98
6	0.45	-81.17	17.38	23.56	6.20
7	0.58	-66.51	8.34	15.36	7.02
8	0.44	-76.52	18.27	25.52	7.25
9	0.61	-64.21	8.35	15.57	7.22
10	0.44	-79.31	17.41	24.10	7.72
11	0.45	-75.11	14.57	22.29	7.72
12	0.45	-74.53	14.63	22.45	7.82
13	0.46	-81.95	17.34	23.34	6.00
14	0.58	-63.68	8.43	15.87	7.44
15	0.44	-78.27	18.23	25.19	6.96
16	0.57	-80.62	7.95	12.77	4.82

Table 3.2 shows the individual input power and output power of each PA element when the IMD3 phasors are left untuned. Since each antenna element presents a different load impedance to each PA, some of the PAs provide a negative gain (loss, elements 2, 9, 11, and 16), even at very low input power values. As shown in Table 3.3, impedance tuning provides every element with gain, and very similar magnitudes and phases of κ_n are observed between the array elements. Table 3.1 shows that the beam magnitudes of the radar and communication main beams more closely resemble their ideal values.

3.2.2 RadCom Directions: $\theta_r = +10^\circ$ and $\theta_c = -15^\circ$

The simulation experiment was repeated for a different combination of radar and communications transmission directions: $\theta_r = +10^\circ$ and $\theta_c = -15^\circ$. For this scenario, the ideal array pattern is shown in Figure 3.12. The magnitude of the radar beam at $\theta_r = +10^\circ$ is 14.26 dBi and the magnitude of the communications beam at $\theta_c = -15^\circ$ is 10.83 dBi. Figure 3.13(a) shows the array pattern with untuned nonlinear PA devices added, resulting in a radar beam magnitude ($\theta_r = +10^\circ$) of 13.36 dBi, and a communications beam magnitude ($\theta_c = -15^\circ$) of 11.22 dBi. The magnitude of the first spurious beam at $\theta_{bb1} = -44^\circ$ is -5.79 dBi, and the magnitude of the second spurious beam at $\theta_{bb2} = +37^\circ$ is 0.73 dBi. As in the first scenario, connecting a compressed PA to each antenna element has disturbed the array pattern significantly.

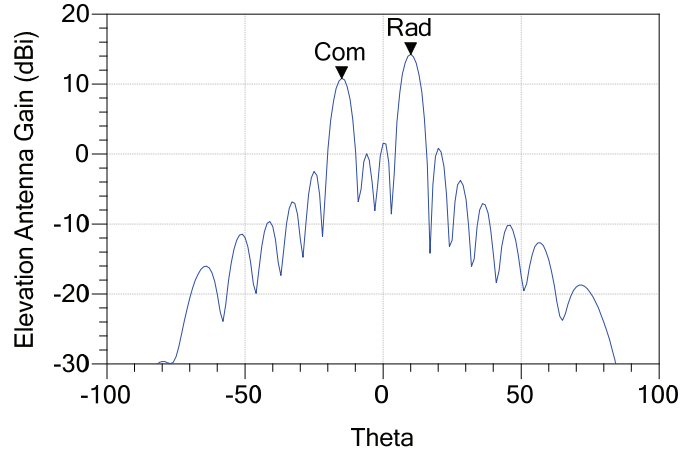


Figure 3.12. Ideal elevation array pattern (dBi) without PAs: $\theta_r = +10^\circ$, $\theta_c = -15^\circ$.

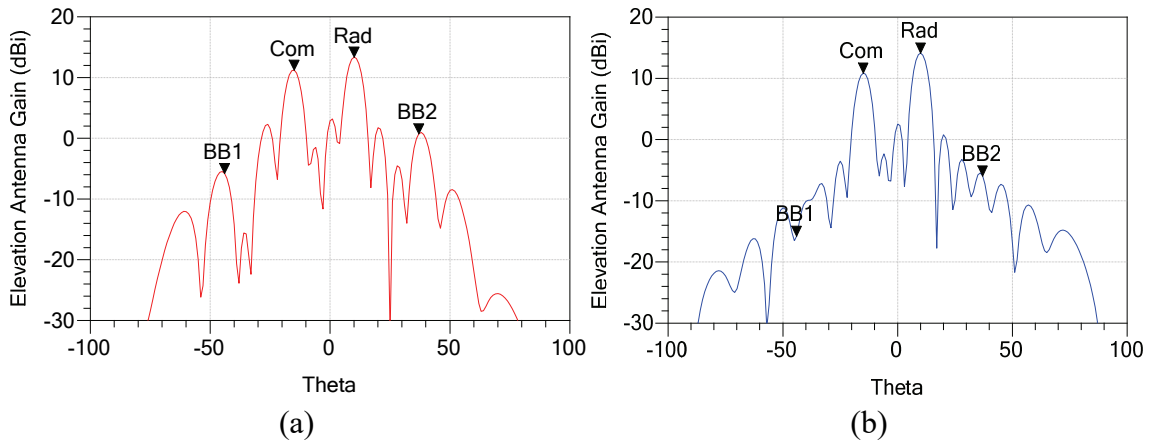


Figure 3.13. (a) Elevation array pattern with untuned PA outputs: $\theta_r = +10^\circ$, $\theta_c = -15^\circ$, calculated $\theta_{bb1} = -44^\circ$, calculated $\theta_{bb2} = +37^\circ$, (b) elevation array pattern with tuned PA outputs: $\theta_r = +10^\circ$ and $\theta_c = -15^\circ$. $\theta_{bb1} = -44^\circ$ and $\theta_{bb2} = +37^\circ$ suppressed.

Impedance tuning was once again implemented using the gradient descent algorithm to lower the standard deviations of $|\kappa_n|$ and $\angle\kappa_n$, compensating for the effects of the IMD3 phasor excitations and providing the needed phasor excitations for the antenna elements based on the desired beam pattern. Figure 3.13(a) shows the untuned array pattern with PAs included, and Figure 3.13(b) shows the tuned far-field array

pattern that is transmitted. The magnitude of the radar beam at $\theta_r = +10^\circ$ in the tuned array is restored to 14.13 dBi, and the magnitude of the communications beam at $\theta_c = -15^\circ$ is 10.87 dBi. The magnitude of the beat beam at $\theta_{bb1} = -44^\circ$ is reduced to -15.79 dBi, and the magnitude of the beat beam at $\theta_{bb2} = +37^\circ$ is reduced to -5.96 dBi, indicating successful spurious beam suppression. Tuning causes the array pattern in Figure 3.13(b) to more closely resemble the ideal array pattern of Figure 3.12.

Table 3.4 shows the beam magnitudes of each beam in the canonical, un-tuned, and tuned cases. The tuned case dBi values of the radar and communications beams are much closer to the ideal values than for the case where IMD3 is uncorrected. Table 3.5 shows the κ_n IMD3 reversal factor element-wise magnitudes and phases for this set of RadCom and spurious beam transmission directions. Table 3.6 shows the κ_n magnitudes and phases following the impedance tuning optimization. Comparing Table 3.6 to Table 3.5 shows that the κ_n values are much more similar in the tuned case (Table 3.6), and that the PA gain values are much more consistent in the tuned case.

Table 3.4. Comparison of Array Gain (dBi) for $\theta_r = +10^\circ$ and $\theta_c = -15^\circ$

Array Pattern Case	Gain at θ_r (dBi)	Gain at θ_c (dBi)	Gain at θ_{bb1} (dBi)	Gain at θ_{bb2} (dBi)
Ideal	14.26	10.83	-	-
IMD3	13.36	11.22	-5.79	0.73
Tuned	14.12	10.87	-15.79	-5.96

Table 3.5. Untuned κ_n values for $\theta_r = +10^\circ$ and $\theta_c = -15^\circ$

Element	$ \kappa_n $	$\angle\kappa_n(^{\circ})$	Input Power (dBm)	Output Power (dBm)	PA Gain (dB)
1	0.31	-116.53	17.26	23.19	5.93
2	0.27	-125.85	15.08	22.71	7.63
3	0.78	-98.84	7.67	8.04	0.36
4	0.71	-92.74	11.74	12.45	0.71
5	0.27	-128.62	16.13	23.38	7.25
6	0.31	-133.25	16.65	22.84	6.19
7	0.59	-93.13	13.78	15.01	1.23
8	0.76	-91.92	4.91	3.97	-0.93
9	0.47	-95.35	14.45	17.81	3.36
10	0.27	-123.73	17.35	26.00	8.64
11	0.24	-125.58	16.35	26.38	10.03
12	0.79	-103.91	10.71	11.71	1.00
13	0.61	-93.54	9.02	12.16	3.14
14	0.22	-142.61	15.59	26.37	10.78
15	0.24	-144.64	17.00	26.80	9.80
16	0.69	-95.70	15.35	16.05	0.70

Table 3.6. Tuned κ_n values for $\theta_r = +10^\circ$ and $\theta_c = -15^\circ$

Element	$ \kappa_n $	$\angle\kappa_n(^{\circ})$	Input Power (dBm)	Output Power (dBm)	PA Gain (dB)
1	0.46	-80.95	18.14	24.34	6.20
2	0.44	-77.38	16.23	23.37	7.14
3	0.56	-64.84	8.16	15.52	7.36
4	0.49	-64.77	12.47	21.13	8.65
5	0.44	-78.00	17.51	24.34	6.83
6	0.48	-79.26	17.93	24.60	6.67
7	0.41	-69.25	14.44	23.47	9.02
8	0.59	-66.62	5.56	12.05	6.40
9	0.46	-74.83	15.03	22.60	7.57
10	0.45	-81.31	18.10	24.49	6.39
11	0.44	-77.50	17.19	24.21	7.02
12	0.50	-64.90	11.20	19.56	8.36
13	0.54	-63.53	9.80	17.81	8.01
14	0.45	-77.46	16.78	23.84	7.06
15	0.47	-80.30	18.24	24.41	6.17
16	0.43	-77.32	15.69	23.33	7.64

3.2.3 RadCom Directions: $\theta_r = +50^\circ$ and $\theta_c = -50^\circ$

For $\theta_r = +50^\circ$ and $\theta_c = -50^\circ$, the ideal array pattern is shown in Figure 3.14.

The magnitude of the radar beam at $\theta_r = +50^\circ$ is 12.52 dBi and the magnitude of the

communications beam at $\theta_c = -50^\circ$ is 8.55 dBi. The array pattern including the untuned transistor devices with IMD3 effects is shown in Figure 3.15(a). With the amplifier distortion present, the magnitude of the radar beam at $\theta_r = +50^\circ$ is 10.98 dBi, the magnitude of the communications beam at $\theta_c = -50^\circ$ is 8.77 dBi, the magnitude of the first beat beam at $\theta_{bb1} = -17^\circ$ is 1.80 dBi, and the magnitude of the second beat beam at $\theta_{bb2} = +17^\circ$ is 3.48 dBi. This again results in a distorted array pattern shape in Figure 3.15(a) compared to Figure 3.14.

Table 3.7 shows the antenna gain magnitudes of the different beams for the ideal 16-element array pattern, the array pattern including the transistors without impedance tuning, and the array pattern with impedance tuning included. Impedance tuning allows very reasonable restoration of the radar and communication beams. Table 3.8 shows the κ_n element-wise magnitudes and phases for the untuned case, and Table 3.9 shows the same information for the tuned case. The results again show that impedance tuning provides consistent κ_n magnitudes and phases between the elements, and that the PA gain values are much more similar.

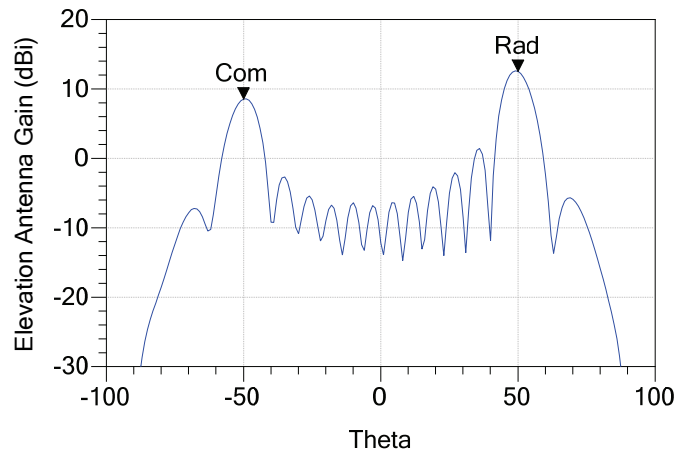


Figure 3.14. Ideal elevation array pattern (dBi) without PAs: $\theta_r = +50^\circ$, $\theta_c = -50^\circ$.

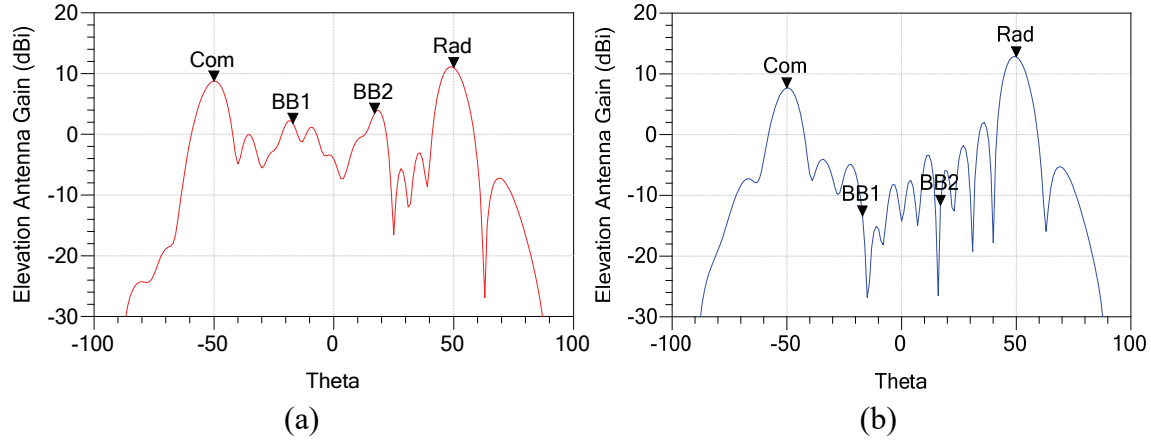


Figure 3.15. (a) Elevation array pattern with un-tuned PA Outputs: $\theta_r = +50^\circ$, $\theta_c = -50^\circ$, calculated $\theta_{bb1} = -17^\circ$, calculated $\theta_{bb2} = +17^\circ$, (b) elevation array pattern with tuned PA outputs: $\theta_r = +50^\circ$ and $\theta_c = -50^\circ$. $\theta_{bb1} = -17^\circ$ and $\theta_{bb2} = +17^\circ$ suppressed.

Table 3.7. Comparison of Array Gain (dBi) for $\theta_r = +50^\circ$ and $\theta_c = -50^\circ$

Array Pattern Case	Gain at θ_r (dBi)	Gain at θ_c (dBi)	Gain at θ_{bb1} (dBi)	Gain at θ_{bb2} (dBi)
Ideal	12.52	8.55	-	-
IMD3	10.98	8.77	1.80	3.48
Tuned	12.81	7.69	-13.40	-11.64

Table 3.8. Un-tuned κ_n values for $\theta_r = +50^\circ$ and $\theta_c = -50^\circ$

Element	$ \kappa_n $	$\angle\kappa_n(^{\circ})$	Input Power (dBm)	Output Power (dBm)	PA Gain (dB)
1	0.31	-110.81	17.45	22.18	4.73
2	0.41	-94.67	15.26	15.64	0.39
3	0.64	-86.53	5.40	1.25	-4.16
4	0.54	-103.84	13.81	12.20	-1.61
5	0.19	-101.44	17.10	26.86	9.76
6	0.39	-90.71	16.43	16.75	0.32
7	0.51	-85.31	8.97	7.93	-1.04
8	0.51	-105.78	11.13	5.95	-5.18
9	0.25	-124.88	16.25	21.95	5.70
10	0.28	-106.08	16.89	21.47	4.52
11	0.44	-96.77	12.09	11.41	-0.68
12	0.53	-99.96	15.80	6.19	-1.61
13	0.48	-100.23	16.25	14.49	-1.77
14	0.32	-110.04	17.45	21.44	3.99
15	0.40	-93.98	14.19	13.85	-0.34
16	0.58	-85.80	5.02	6.92	1.91

Table 3.9. Tuned κ_n values for $\theta_r = +50^\circ$ and $\theta_c = -50^\circ$

Element	$ \kappa_n $	$\angle\kappa_n(^{\circ})$	Input Power (dBm)	Output Power (dBm)	PA Gain (dB)
1	0.49	-83.95	18.02	23.37	5.34
2	0.44	-79.20	15.88	23.06	7.19
3	0.60	-76.27	5.93	10.89	4.96
4	0.49	-76.89	14.15	21.45	7.30
5	0.48	-81.34	17.94	23.90	5.95
6	0.45	-80.53	17.01	23.49	6.48
7	0.57	-71.47	9.64	16.38	6.75
8	0.56	-71.14	11.76	19.16	7.40
9	0.46	-79.30	17.53	23.86	6.32
10	0.47	-80.89	17.74	23.65	5.92
11	0.52	-70.75	12.78	20.56	7.78
12	0.58	-69.70	8.37	14.98	6.61
13	0.44	-80.05	16.62	23.26	6.65
14	0.46	-81.71	18.06	23.93	5.87
15	0.41	-71.09	15.06	23.88	8.83
16	0.60	-54.34	5.79	13.80	8.02

The three simulation experiments have demonstrated that impedance tuning can provide notable improvement in the array patterns when IMD3 distorts the array patterns from the ideal array pattern cases, even when the distortion is significant.

3.3 Comparison of Impedance Tuning with Predistortion

Instead of using impedance tuning, Braithwaite [22] applies digital predistortion (DPD) to reduce the IMD3 beams that occur from PA nonlinearities in a dual-beam, shared-frequency system. DPD modules are applied for beam correction in the four transmitted beam directions: two for the intended linear beam directions, and two for the unintended beat beam directions. Each DPD module uses a third-order basis vector that is calculated for each beam to reverse the nonlinear effects. These basis vector waveforms for each beam are shown below, as provided in [22]:

$$\begin{aligned}
b_{r_n} &= \left[|I_{r_n}|^2 + 2 \cdot |I_{c_n}|^2 \right] \cdot I_{r_n} \\
b_{c_n} &= \left[|I_{c_n}|^2 + 2 \cdot |I_{r_n}|^2 \right] \cdot I_{c_n} \\
b_{bb1_n} &= I_{r_n}^2 \cdot I_{c_n}^* \\
b_{bb2_n} &= I_{c_n}^2 \cdot I_{r_n}^* ,
\end{aligned} \tag{3.9}$$

where I_{r_n} and I_{c_n} are the current phasors for the radar and communications signals, respectively, from equation (3.1). The basis waveforms b_{r_n} , b_{c_n} , b_{bb1_n} , and b_{bb2_n} are the correction waveforms described in [22]. These are designed based on the current phasors for the intended radar and communications signals to suppress the radiation transmissions at θ_{bb1} and θ_{bb2} . The DPD module signals for the four beam directions θ_r , θ_c , θ_{bb1} , and θ_{bb2} are the following:

$$\begin{aligned}
I_{DPD,r_n} &= I_{r_n} + b_{r_n} \cdot \rho_{r_n} \\
I_{DPD,c_n} &= I_{c_n} + b_{c_n} \cdot \rho_{c_n} \\
I_{DPD,bb1_n} &= b_{bb1_n} \cdot \rho_{bb1_n} \\
I_{DPD,bb2_n} &= b_{bb2_n} \cdot \rho_{bb2_n} ,
\end{aligned} \tag{10}$$

where ρ_{r_n} , ρ_{c_n} , ρ_{bb1_n} , and ρ_{bb2_n} are the DPD coefficient vectors for each beam. The DPD coefficient vectors are used to weight the basis waveforms to create the desired correction PA input signal [22]. The predistorted phasor to be fed to each PA is summed together from (3.10) as follows,

$$I_{predist_n} = I_{DPD,r_n} + I_{DPD,c_n} + I_{DPD,bb1_n} + I_{DPD,bb2_n}. \tag{11}$$

This calculation results in a linear signal fed to the antenna elements after amplification.

To compare the impedance tuning method with predistortion, a Matlab/ADS co-simulation using this DPD technique was performed to verify that the predistortion calculations in (3.9)-(3.11) resulted in a corrected array pattern with beat beam suppression. The predistortion calculations were performed in Matlab, based on the current phasors for the intended RadCom transmission directions. The ρ_{r_n} , ρ_{c_n} , ρ_{bb1_n} ,

and ρ_{bb2_n} coefficients were calculated by the Matlab DPD system object using the PA input currents (3.1) and the PA output currents (3.3) recorded from ADS. The resulting predistorted signals (3.11) were then fed to each PA in ADS to the same transistor PAs as before. A fixed single-stub matching network was used on each element to match the driven element PA load impedances for the simplest beam condition at the broadside scan angle: ($\theta_r = \theta_c = 0^\circ$). The fixed single-stub matching was designed with the same input power values to the radar and communications components as the experiments in the previous section. Unlike the impedance tuning scenario, this network is not tuned as the beam angle is changed, but is held constant during the entire experiment. Figure 3.16 shows the resulting corrected array pattern when predistortion is applied prior to amplification, with fixed matching networks on the PAs, for $\theta_r = -30^\circ$ and $\theta_c = +40^\circ$. These are the same transmission angles as in Figures 3.10-3.11. An analysis of the κ_n metric for the case of predistortion is presented in Table 3.10. The κ_n magnitudes and phases show significant differences compared to the results of impedance tuning shown in Table 3.3. In predistortion, the input waveforms are adjusted to compensate for amplifier nonlinearities and the nonlinearities are left unchanged, whereas impedance tuning focuses on linearizing the amplifier and does not change the inputs. In Figure 3.16, as a result of predistortion, the magnitude of the first spurious beam at $\theta_{bb1} = -12^\circ$ is suppressed to -4.64 dBi and the magnitude of the second spurious beam at $\theta_{bb2} = +21^\circ$ is suppressed to -5.48 dBi. For comparison, the impedance tuning experiments of the preceding section provided suppression of the first spurious beam $\theta_{bb1} = -12^\circ$ to -5.70 dBi and suppression of the second spurious beam at $\theta_{bb2} = +21^\circ$ to -15.23 dBi. In this experiment, predistortion indeed provided significant suppression of the beat beams, but

did not suppress either of the beat beams as well as impedance tuning for this beam angle combination.

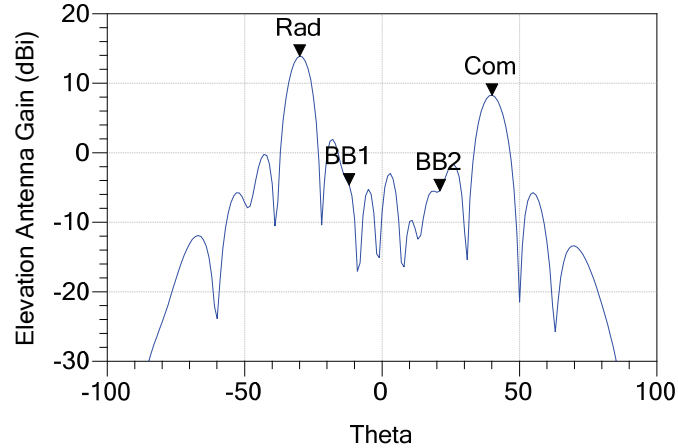


Figure 3.16. Predistortion array pattern correction for: $\theta_r = -30^\circ$ and $\theta_c = +40^\circ$. $\theta_{bb1} = -12^\circ$ and $\theta_{bb2} = +21^\circ$ suppressed.

The individual PA gain and output power values are shown in Table 3.10. Unlike the impedance tuning method, predistortion is not designed to maximize the gain of the individual element PAs, but is focused solely on linearization. Since predistortion modifies the element inputs to accomplish the desired beam pattern and does not adjust the amplifiers, the resulting element gain values of the PAs after predistortion is applied vary widely (Table 3.10) as compared to impedance tuning (Table 3.3). This is expected to cause a wide variation in power-added efficiency of the PAs as well. In both cases, back-off of many PA input power values is necessary to establish the beam pattern, but impedance tuning can make the best of the situation by adjusting to maximize element gain, whereas the impedance matching of the predistortion method is fixed, and therefore cannot be adjusted to compensate. Since only the input waveform can be adjusted in the predistortion method, little flexibility exists to address gain and efficiency issues in real

time. In fact, many of the predistortion input power values to the elements are higher than the impedance tuning case, requiring more gain from preceding amplifier stages.

Table 3.10. Predistortion κ_n values for $\theta_r = -30^\circ$ and $\theta_c = +40^\circ$

Element	$ \kappa_n $	$\angle\kappa_n(^{\circ})$	Input Power (dBm)	Output Power (dBm)	PA Gain (dB)
1	0.62	-36.25	20.45	21.74	1.29
2	0.31	-14.55	8.70	16.62	7.92
3	0.51	-13.27	19.23	21.57	2.34
4	0.36	-9.36	15.92	21.94	6.02
5	0.37	-3.89	15.84	21.37	5.53
6	0.49	-12.85	19.33	22.37	3.04
7	0.30	-4.56	8.61	15.97	7.36
8	0.60	-36.26	20.47	21.88	1.41
9	0.31	-15.31	8.69	16.61	7.93
10	0.51	-13.16	19.24	21.58	2.34
11	0.36	-8.90	15.90	21.86	5.96
12	0.37	-4.44	15.86	21.46	5.60
13	0.49	-13.49	19.32	22.47	3.14
14	0.31	-3.41	8.60	15.85	7.24
15	0.61	-35.25	20.45	21.38	0.93
16	0.24	-13.37	8.93	17.98	9.05

Predistortion and impedance tuning were also compared for the other scan angle directions addressed in Figures 3.12-3.15. For $\theta_r = +10^\circ$ and $\theta_c = -15^\circ$, impedance tuning provided a linear average element output power of 22.82 dBm (Table 3.6) with a linear average element input power of 15.77 dBm. The linear average element PA gain was 7.37 dB for impedance tuning. Predistortion provided a linear average element output power of 21.88 dBm from a linear average input power of 17.60 dBm. The linear average element PA gain was 5.59 dB for predistortion, significantly lower than for impedance tuning. For $\theta_r = +50^\circ$ and $\theta_c = -50^\circ$, impedance tuning provided a linear average element output power of 21.96 dBm (Table 3.9), linear average element input power of 15.41 dBm, and linear average element PA gain of 6.82 dB. Predistortion provided a linear average element output power of 19.66 dBm, linear average element

input power of 16.84 dBm, and linear average element PA gain of 4.89 dB. Impedance tuning again provided higher linear average element PA output power and gain across all elements compared to predistortion.

While the impedance tuning method addresses both linearity and efficiency issues in real time, it can be combined with predistortion to provide an overall benefit in some cases. In this experiment, impedance tuning was performed first, followed by predistortion, with the same Matlab input signal calculations applied as in the standalone case. Figure 3.17 shows the array pattern results from combining predistortion and impedance tuning for $\theta_r = -30^\circ$ and $\theta_c = +40^\circ$. The κ_n magnitudes and phases, as well as output powers, are recorded in Table 3.11. As shown in Table 3.11, the combination of predistortion and impedance tuning resulted in a linear average element output power of 22.90 dBm, presenting a further linear average element output power improvement from the standalone impedance tuning value of 22.36 dBm. The linear average element PA gain, however, for the combination method was reduced to 6.33 dB, compared to 7.04 dB linear average element PA gain of standalone impedance tuning. Since predistortion was performed after impedance tuning, the average PA gain was reduced when predistortion was applied to improve linearity across the array elements. Figure 3.17 shows that the spurious beams were successfully suppressed, as in the case with standalone predistortion and standalone impedance tuning.

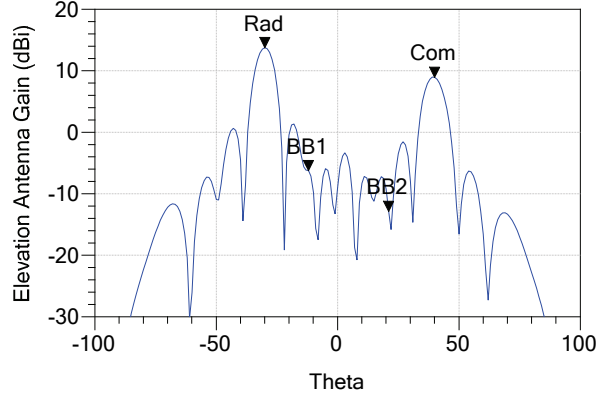


Figure 3.17. Predistortion and impedance tuning array pattern correction for: $\theta_r = -30^\circ$ and $\theta_c = +40^\circ$. $\theta_{bb1} = -12^\circ$ and $\theta_{bb2} = +21^\circ$ suppressed.

Table 3.11. Predistortion and Impedance Tuning κ_n Values for $\theta_r = -30^\circ$ and $\theta_c = +40^\circ$

Element	$ \kappa_n $	$\angle\kappa_n(^{\circ})$	Input Power (dBm)	Output Power (dBm)	PA Gain (dB)
1	0.44	63.11	20.28	24.75	4.47
2	0.32	73.68	8.49	15.57	7.08
3	0.38	72.16	19.18	24.47	5.29
4	0.30	77.34	15.63	22.81	7.18
5	0.31	80.48	15.72	23.26	7.54
6	0.37	73.34	19.23	24.07	4.84
7	0.31	86.98	8.53	15.76	7.22
8	0.44	48.59	20.47	26.08	5.61
9	0.32	61.02	8.50	15.71	7.21
10	0.38	74.01	19.17	24.39	5.22
11	0.30	78.09	15.64	22.92	7.28
12	0.31	80.14	15.70	23.11	7.41
13	0.38	73.23	19.22	23.88	4.66
14	0.32	90.03	8.62	16.20	7.58
15	0.43	54.60	20.41	25.87	5.47
16	0.24	69.25	8.10	12.85	4.75

The same experiment was performed for the other scan angle combinations using the combined impedance tuning and predistortion method. The combined method provided a linear average element output power of 23.25 dBm for $\theta_r = +10^\circ$ and $\theta_c = -15^\circ$ from a linear average element input power of 17.46 dBm. The linear average element PA gain was 6.55 dB for the combined method. The combined method also

provided a linear average element output power of 22.38 dBm for $\theta_r = +50^\circ$ and $\theta_c = -50^\circ$ from a linear average element input power of 16.65 dBm. The linear average element PA gain was 6.40 dB for the combined method. The combination method therefore further improved element output power across all elements in all angles tested over using either method alone. Lower average element PA gain was realized, however, as a result of applying predistortion after impedance tuning. This means that the input signal power must be larger in the combined case, likely reducing the combined efficiency of the element amplifiers when compared to using impedance tuning alone.

Tables 3.12, 3.13, and 3.14 provide a summary of the performance of the impedance tuning, predistortion, and combined methods. Table 3.12 shows that applying impedance tuning for $\theta_r = -30^\circ$ and $\theta_c = +40^\circ$ provides an increase of radiated powers to 29.33 dBm for the radar beam and 24.49 dBm for the communications beam. These power values result in a 5.62% improvement in radar range and a 22.20% improvement in communication range when compared to predistortion. Furthermore, impedance tuning suppresses the beat beams lower than with predistortion. If the combined method is used, the radiated power increases to 29.87 dBm (8.95% radar range increase compared to predistortion) for the radar beam and the 25.06 dBm for the communications beam (30.47% communication range increase compared to predistortion).

The experiment was repeated for the other scan angle combinations. For the $\theta_r = +10^\circ$ and $\theta_c = -15^\circ$ (Table 3.13), impedance tuning provided a range increase of 0.69% for the radar beam and 11.94% range increase for the communications beam compared to standalone predistortion. The combined method provided a range increase of 3.10% for the radar beam and a 17.75% range increase for the communications beam compared to

standalone predistortion. For $\theta_r = +50^\circ$ and $\theta_c = -50^\circ$ (Table 3.14), impedance tuning provided a range increase of 14.03% for the radar beam and a 34.11% range increase for the communications beam compared to standalone predistortion. The combination method provided a range increase of 16.68% for the radar beam and a 42.06% range increase for the communications beam compared to standalone predistortion. Impedance tuning is therefore essential in increasing range capabilities and suppressing spurious beams in a dual-beam RadCom system.

Overall, these simulation experiments have demonstrated that impedance tuning can increase range capability while providing excellent beat-beam suppression. Impedance tuning also provides better element-wise PA gain and better radiated power than predistortion alone. Combining impedance tuning and predistortion provides many of the benefits of impedance tuning, using predistortion to further reduce the beat beams in some cases, but typically results in reduced element-wise amplifier gain compared to the approach using only impedance tuning, and will result in higher required input power levels to the element PAs.

Table 3.12. Radiated Power and Spurious Beam Levels for $\theta_r = -30^\circ$ and $\theta_c = +40^\circ$

Method	Radiated Power (dBm) θ_r	Radiated Power (dBm) θ_c	Gain at θ_{bb1} (dBi)	Gain at θ_{bb2} (dBi)
Predistortion	28.38	22.75	-4.64	-5.48
Impedance Tuning	29.33	24.49	-5.70	-15.23
Combination	29.87	25.06	-6.24	-12.87

Table 3.13. Radiated Power and Spurious Beam Levels for $\theta_r = +10^\circ$ and $\theta_c = -15^\circ$

Method	Radiated Power (dBm) θ_r	Radiated Power (dBm) θ_c	Gain at θ_{bb1} (dBi)	Gain at θ_{bb2} (dBi)
Predistortion	29.88	25.76	-9.38	-5.93
Impedance Tuning	30.00	26.74	-15.79	-5.96
Combination	30.41	27.18	-14.07	-5.23

Table 3.14. Radiated Power and Spurious Beam Levels for $\theta_r = +50^\circ$ and $\theta_c = -50^\circ$

Method	Radiated Power (dBm) θ_r	Radiated Power (dBm) θ_c	Gain at θ_{bb1} (dBi)	Gain at θ_{bb2} (dBi)
Predistortion	25.96	20.57	-3.08	-1.25
Impedance Tuning	28.24	23.12	-13.40	-11.64
Combination	28.64	23.62	-10.11	-14.42

3.4 Summary

Load-impedance tuning of power amplifiers in phased-array elements has been demonstrated as a solution to eliminate undesired, spurious beat beams in the transmission pattern while maximizing element amplifier gain. A joint circuit and electromagnetic simulation platform was used to demonstrate an impedance tuning approach to maximize output power and minimize the spurious beat beams for a 16-element, $\lambda/2$ spaced, microstrip linear array. The use of the IMD3 reversal factor provided a significant improvement in the dual-beam array pattern from the untuned IMD3 array pattern caused by third-order PA nonlinearities for multiple beam angles in same-frequency, dual-beam radar-communications transmission examples. Comparison of the tuned array pattern to the untuned array pattern including the results of amplifier nonlinearities, as well as to the ideal array pattern, shows that the array pattern can be improved to restore the intended radar and communications beam relative amplitudes,

suppress the unintended spurious beat beams, and increase transmitter output power. Impedance tuning was also shown to have an advantage over predistortion because it focuses on maximizing both output power and linearity, providing increased range capabilities for both radar and communications while also minimizing the beat beams. While combining the impedance tuning and predistortion techniques is possible, and can cause further reduction of the spurious beat beams in some cases, it also often results in higher required element input power and lower element PA gain. As such, the standalone impedance tuning method demonstrated in these experiments is recommended as the approach of choice to both maximize PA gain and efficiency while significantly reducing the beat beams. Impedance tuning, as presented in this work, provides a useful new tool for the reduction of undesirable distortions in radar-communication multi-beam, spatially diverse transmissions.

CHAPTER FOUR

Secure Transmission in Dual-Beam Phased Array Transmitters

This chapter has been adapted from the publication: [40] P. Rodriguez-Garcia, G. Ledford, C. Baylis and R. J. Marks, "Real-Time Synthesis Approach for Simultaneous Radar and Spatially Secure Communications from a Common Phased Array," *2019 IEEE Radio and Wireless Symposium (RWS)*, Orlando, FL, USA, 2019, pp. 1-4.

Transmitting radar and communications signals from the same dual-beam phased array is an inherently real-time application since coexistence and spectrum sharing in unpredictable, dynamic 5G environments require the agility of a real-time solution. Simultaneously securing the information sent in the communications transmissions while sharing the spectrum and operating space against recovery by unintended receivers should also be considered in a real-time mission scenario. The research in this chapter extends the directional modulation (DM) concept previously prescribed for secure directional communications [36]-[38] for implementation in a dual-beam RadCom system to implement spatially secure communications capabilities in the dual-purpose system. Modulated signals that share the same frequency are transmitted in different directions and information is only de-modulated and therefore recovered by the intended communications receiver, based on the DM concept which calculates intelligently computed phase shifts [36] for the phasor excitations fed to the antenna elements. The purpose of DM in a RadCom system is to transmit recoverable constellation symbols toward the intended receiver's direction, while simultaneously transmitting a different signal toward a known unintended receiver or potential eavesdropper.

To integrate spatially secure communications in the dual-beam RadCom platform, Barker code sequencing can be applied, as described by Yinjuan [39]. The works [46]-[50] all describe waveform designs that can share radar and communications functionality using orthogonal frequency division multiplexing (OFDM) with multiple orthogonal subcarriers to transmit the desired data. These all assume multiple carrier frequencies are transmitted, so Barker code sequencing to compress a modulated signal into a radar pulse from a shared-frequency system is more desirable for this case. Optimal radar mission functionality from such a shared-frequency system is verified by analyzing the matched filter response on the return pulse from a moving target, as well as the range resolution and maximum unambiguous detection range in Section 4.2.

This chapter presents a modified uniform linear array (ULA) configuration, as shown in Figure 4.1. This system can be adapted to various scenarios as described by [51]-[55]. The element phasor excitations are derived from a shared-frequency carrier for both the radar and communications signals, modified by the magnitude and phase of a phasor baseband-weighted vector, which is fed to the individual radiating antenna elements. The baseband-weighted vector is calculated in real-time as a phasor using zero-forcing directional modulation (ZF) [38]. Since the ZF method is deterministic and presents a reasonable computational workload, it is suitable for a novel real-time implementation in this dual-beam RadCom system to provide spatially secure communications.

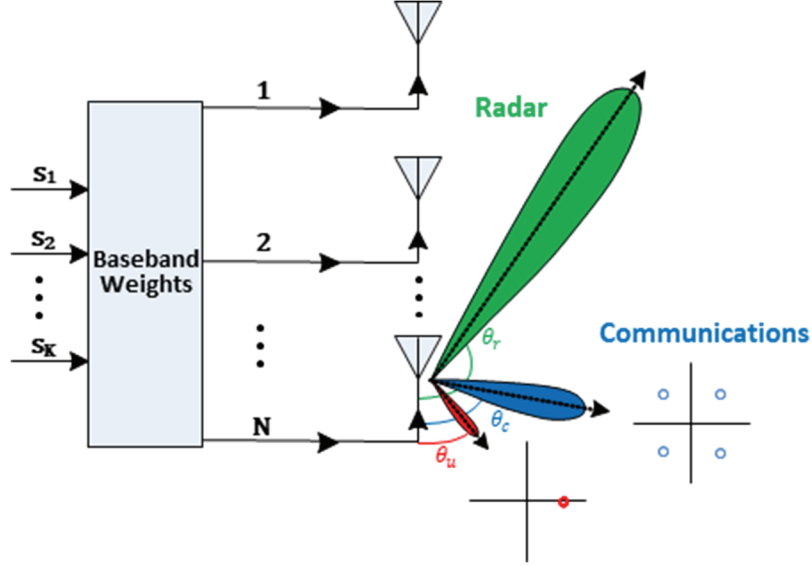


Figure 4.1. Block diagram for Dual-Beam RadCom transmitter with spatially secure communications.

4.1 Zero-Forcing Directional Modulation for Radar and Communications

The zero-forcing directional modulation solution begins with a description of the ULA, the directions of the intended radar and communications signals with respect to the phased array, the phase of the intended signal excitations, and the relative power allocated to each of the intended signals. The ULA has N elements uniformly spaced a distance d apart. The number of intended signals is given by the integer K , where $K \leq N$. The directions of the intended signals are collectively referred to as the vector $\Theta'_d = (\theta'_1, \dots, \theta'_k, \dots, \theta'_K)$, where θ'_k is the direction of the k^{th} intended signal. The notation and definitions of the steering vector, steering matrix, and steering matrix pseudo-inverse are defined by Xie [38], respectively. The baseband-weighted vector calculation is given by

$$\mathbf{W}(\theta') = \frac{\sqrt{P_a}}{\sqrt{K}} (\mathbf{H}(\Theta'_d)^H)^\dagger \text{diag}\{\sqrt{\mathbf{p}}\} \mathbf{s} \quad (4.1)$$

where \mathbf{s} is a $K \times M$ constellation symbol matrix according to the number of intended transmission angles and number of symbol states M in the transmitted signals, $\mathbf{p} =$

$(p_1, \dots, p_k, \dots, p_K)$ is the relative power of the intended signals, P_a is the average transmit power, and $(\mathbf{H}(\boldsymbol{\Theta}'_d)^H)^\dagger$ is the steering matrix pseudo-inverse that encompasses the intended array steering directions θ' . The computed transmit constellation symbols formed at the desired directions θ' through the dual-beam phased array antenna pattern is then given by

$$\mathbf{R}(\theta') = f(\theta') \sum_{n=0}^{N-1} e^{jn(k_0 d \sin \theta')} \mathbf{W}(\theta') \quad (4.2)$$

where $\mathbf{W}(\theta')$ is the phasor baseband-weighted excitation signal formulated by (4.1) at the intended transmit angle θ' and $f(\theta')$ is the element pattern of the individual antenna elements in the array at intended transmit angle θ' .

Secure real-time dual-beam transmission in various real-time synthesis scenarios can be demonstrated in a Matlab simulation environment using the ZF method with a 16-element $\lambda/2$ uniformly spaced array comprised of microstrip antenna elements and an average transmit power $P_a = 5W$. The radar and communications signals are simultaneously transmitted from the same microstrip phased array with the S-band carrier frequency of 3.55 GHz to lie within the recently reallocated frequency band of 3.45–3.65 GHz. This allows more efficient real-time spectrum usage within the frequency band that has been reallocated for use by both radar and communications platforms which was previously only allocated for use by radar platforms.

An ideal dual-beam RadCom transmission pattern is presented in Figure 4.2, which assumes no IMD3 transmissions as discussed in Chapter Three. A main beam is sent to -30° that has a larger magnitude than the other main beam sent to $+40^\circ$. These beams represent the radar and communications directional transmissions, respectively.

As shown in Figure 4.2, a target is present within the radar beam, an intended receiver is present within the communications beam, and an unintended receiver (potential eavesdropper) is present within one of the sidelobes of the dual-beam RadCom pattern. A QPSK-modulated communications signal is sent to the intended communications receiver at $+40^\circ$. A BPSK-modulated signal is simultaneously sent to the target of interest at -30° and is compressed to a radar pulse upon Barker code sequencing. The unintended receiver at $+70^\circ$ consequentially observes these transmissions. In this initial transmission scenario, there is no directional security enforced. Therefore, no ZF directional modulation is performed to secure the transmission at the unintended receiver direction, and the antenna elements in the dual-beam array are only fed with excitations for the intended transmission angles $\theta' = -30^\circ, +40^\circ$ for the modulated radar signal and for the modulated communications signal, respectively. Equation (4.1) can be used to perform the calculations. The relative power vector used for this case was, $\mathbf{p} = [10 \ 1.25]^T$, with the first and second elements of the vector representing the radar and communications signals, respectively. For transmitting a BPSK-modulated signal and QPSK-modulated signal, there are $M = 8$ desired constellation symbol states. The phasor baseband weight calculation is designed to simultaneously transmit an array pattern for each symbol state that continues to illuminate both the radar target and the intended receiver, so the array pattern remains relatively undisturbed as shown in Figure 4.2. The intended symbol matrix for the baseband weight calculation in (4.1) without enforced directional security is therefore described as,

$$\mathbf{s} = \begin{bmatrix} 1 & 1 & 1 & 1 & -1 & -1 & -1 & -1 \\ 1+j & 1-j & -1+j & -1-j & 1+j & 1-j & -1+j & -1-j \end{bmatrix}. \quad (4.3)$$

The first row in (4.3) corresponds to the desired BPSK symbols which are separated in the complex plane by 180° . The second row in (4.3) corresponds to the desired QPSK symbols which are separated in the complex plane by 90° . As a result, without any ZF directional modulation baseband weight calculation to intentionally disrupt the signals sent to the unintended receiver, the unintended receiver has the potential to recover the information sent in its direction. Figure 4.3 shows the superposition of the $M = 8$ constellation symbol states in the complex plane for the information sent to the unintended receiver. While the transmitted symbols to the unintended receiver at $+70^\circ$ appear scattered around the constellation as shown in Figure 4.3, with a potentially sophisticated demodulator, this unintended receiver has some chance to recover the information since an observed pattern of symmetry exists.

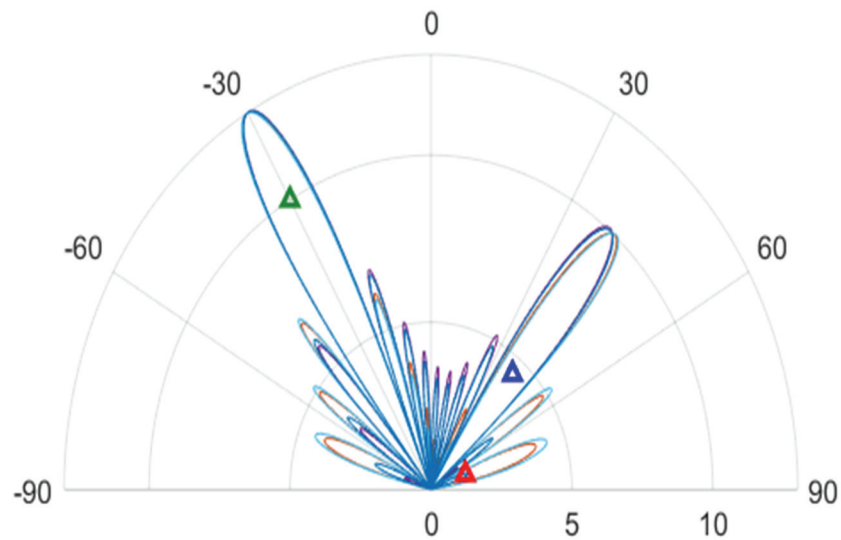


Figure 4.2. Phased array spatial scene for each symbol state with a radar beam sent to detect a target (green) at -30° , a communications beam sent to an intended receiver (blue) at $+40^\circ$, and an unintended receiver (red) located within one of the sidelobes at $+70^\circ$ when no directional security is enforced.

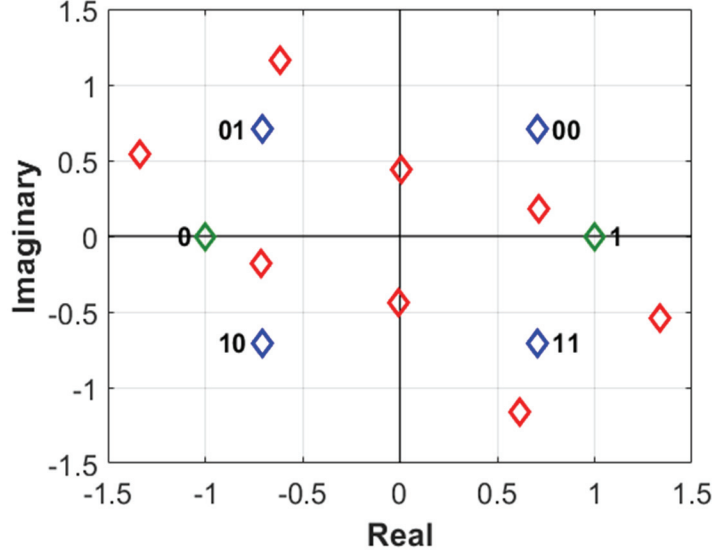


Figure 4.3. Radar transmit mode constellation scene with a BPSK-modulated signal sent to -30° (green), and a QPSK-modulated signal sent to an intended receiver at $+40^\circ$ (blue) with an unintended receiver located at $+70^\circ$ (red).

The next transmission scenarios are shown in Figure 4.4 and Figure 4.5. In these transmission scenarios, directional security is enforced, and the known unintended receiver location is now used to send intentionally unrecoverable constellation symbols in its direction. The DM calculations of the baseband weights (4.1) using the ZF method is utilized with a now modified \mathbf{s} matrix described as,

$$\mathbf{s} = \begin{bmatrix} 1 & 1 & 1 & 1 & -1 & -1 & -1 & -1 \\ 1+j & 1-j & -1+j & -1-j & 1+j & 1-j & -1+j & -1-j \\ 0.5 & 0.5 & 0.5 & 0.5 & 0.5 & 0.5 & 0.5 & 0.5 \end{bmatrix}, \quad (4.4)$$

to send intentional symbols to the unintended receiver during the transmit mode of the radar. The intended transmitted directions for baseband weight calculation (4.1) are now $\theta' = -30^\circ, +40^\circ, +70^\circ$. The relative power vector used for the directional security case was, $\mathbf{p} = [10 \ 1.25 \ 0.5]^T$, for the radar, communications, and unintended receiver signals respectively. In the radar's transmit mode, spatially secure directional modulation is

applied to the same spatial scene as the first scenario, but with the goal of obscuring the signal for the unintended receiver while the radar and intended receiver signals remain undisturbed. Compared to Figure 4.2, the array pattern shape is slightly altered in Figure 4.4 because the magnitudes and phases of the newly calculated excitations (4.3) have been modified since the direction of the unintended receiver is now accounted for in the calculation. Nonetheless, the radar target and the communications intended receiver are still illuminated for all symbol states, as is the unintended receiver because of the robustness of the calculation in (4.1).

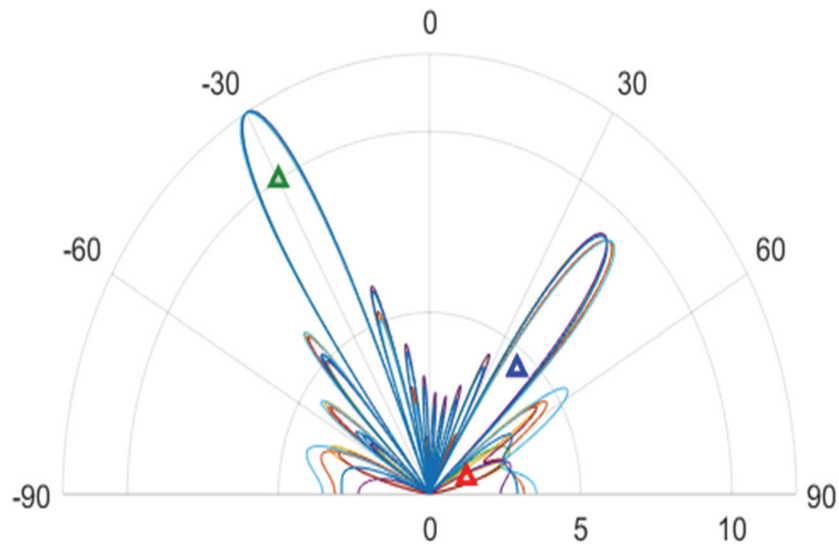


Figure 4.4. Phased array spatial scene when directional security is enforced in the radar transmit mode.

In this case, the superposition of the $M = 8$ constellation symbols states results in a uniform symbol, as observed by the unintended receiver at $+70^\circ$ in Figure 4.5. The symbol of 0.5 was selected so that the symbols are transmitted away from the radar and communications symbol, leaving no chance for the unintended receiver to obtain the information sent to the intended radar and communications directions. The Barker coded

BPSK constellation is still sent to the radar direction and the intended receiver still observes the QPSK constellation. The functionality of the radar and intended communications signals is therefore left unharmed by the ZF computation, while the same symbol for all constellation symbol states is sent to the unintended receiver. This allows the radar and communications signal to continue transmitting while ensuring that the unintended receiver does not recover any information.

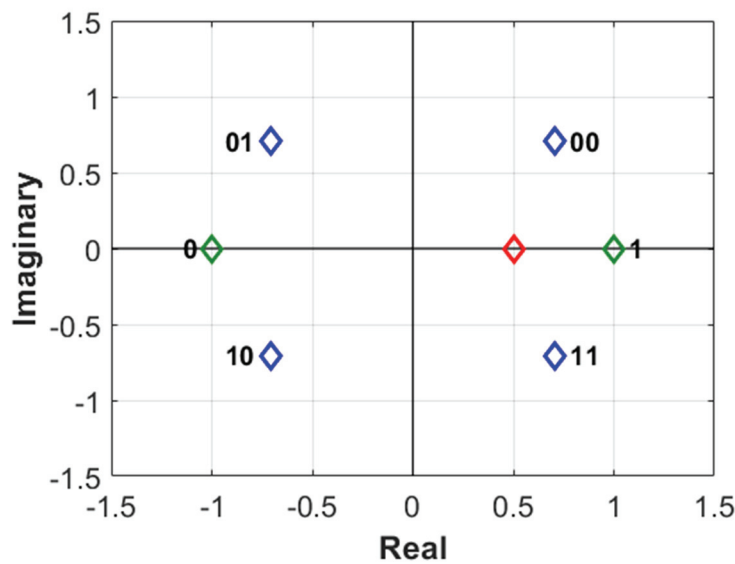


Figure 4.5. Radar transmit mode in which direction security is enforced to deliberately send the same symbols to the unintended receiver direction of $+70^\circ$.

Similarly, as shown in the transmission scenarios in Figure 4.6, Figure 4.7, and Figure 4.8, the ZF method is applied to the radar's receive mode where the magnitude of the radar transmission pulse is zero as it awaits the return echo signal from the target. The baseband weights are recalculated in real-time and still provide the desired constellation symbols to the intended receiver at $+40^\circ$ and the unintended receiver at $+70^\circ$. The desired symbol \mathbf{s} for the radar's receive mode is now

$$\mathbf{s} = \begin{bmatrix} 0 & 0 & 0 & 0 & 0 & 0 & 0 & 0 \\ 1+j & 1-j & -1+j & -1-j & 1+j & 1-j & -1+j & -1-j \\ 0.5 & 0.5 & 0.5 & 0.5 & 0.5 & 0.5 & 0.5 & 0.5 \end{bmatrix}, \quad (4.5)$$

so the recalculation of the baseband-weighted vector ensures spatially secure communications is maintained while the radar transitions from the transmit mode to the receive mode according to the structure of the synthesized radar pulse. Since the radar pulse magnitude is zero, a constellation symbol of zero is transmitted for all states, so the transmitted radar beam disappears, as shown in Figure 4.6. Radar systems typically transition rapidly between transmit and receive modes in their transceiver modules via a circulator [54]. The receiver array pattern can be therefore be activated with a radar beam that continues to illuminate the target as it awaits the return signal from the radar pulse, as shown in Figure 4.7. This assumes that a monostatic system is implemented where the same phased array is used for both transmit and receive modes.

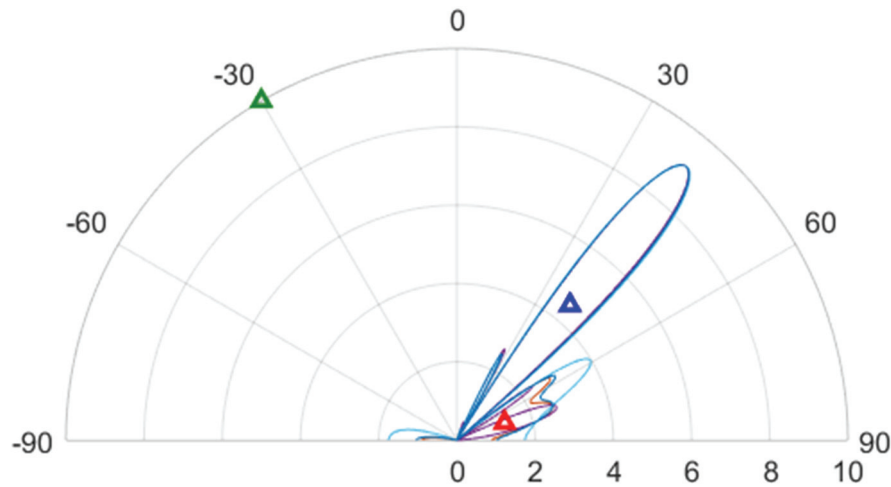


Figure 4.6. Phased array spatial scene for each symbol state when directional security is enforced in the radar receive mode (radar transmission zero).

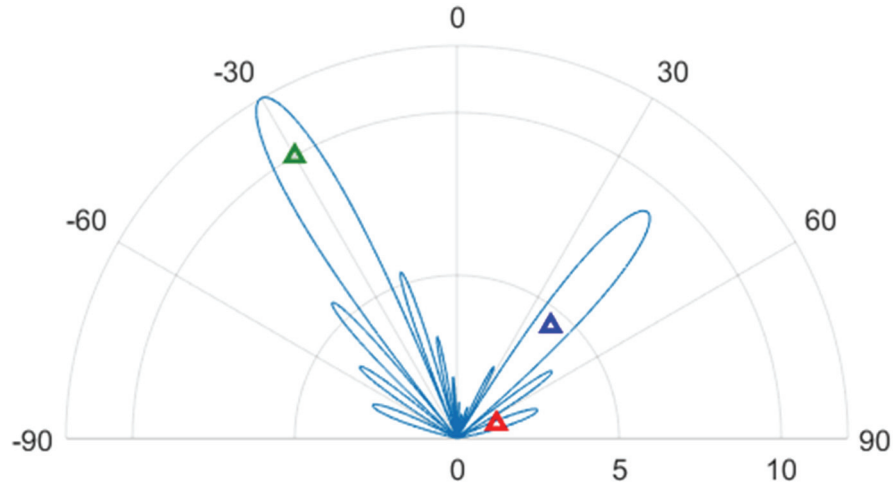


Figure 4.7. Phased array receiver array pattern when a circulator is used to transition to the receive mode to await the radar return signal for processing.

The constellation diagram in Figure 4.8 for the radar receive mode verifies that the same constellation symbol of 0.5 is still sent to the unintended receiver, while the radar transmission pulse is zero. This allows the radar beam to continue to transition between the transmit and receive mode while directional security is simultaneously maintained.

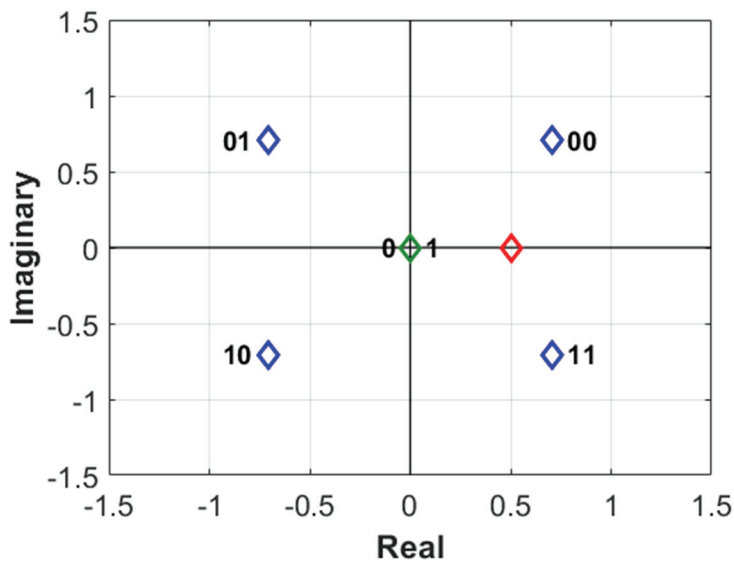


Figure 4.8. Radar receive mode in which direction security is enforced to deliberately send the same symbols to the unintended receiver direction of $+70^\circ$.

4.2 Barker Code Radar Signal Synthesis

To simultaneously synthesize the radar signal to have a transmit and receive mode as proposed in the previous section, phase-coded Barker sequences are applied to compress the continuous BPSK signal into a radar pulse. The BPSK signal is compressed to a radar pulse with a length two Barker code, representing the Barker sequence of +1, -1, resembling the BPSK symbols. As customary with Barker sequencing, the radar pulse is divided into sub-pulses according to the sequence selected. Range radar applications typically require high bandwidth waveforms to provide adequate range resolution, allowing differentiation between targets that are closely spaced apart. As such, a relatively short length Barker code sequence was selected to minimize the radar signal pulse width so that a high bandwidth could be achieved improving the range resolution of the radar. A sub-pulse width of 0.025 μs was therefore selected for each symbol, resulting in a total pulse width of 0.05 μs , and a minimum bit rate of 40 Mbps. The communication QPSK constellation is a two-bit signal and thus has a bit rate of 80 Mbps. A pulse repetition interval (PRI) of 700 μs was used to improve the unambiguous range. This repetition interval results in a pulse repetition frequency (PRF) of $PRF = 1.429$ kHz. The return pulse of a moving target traveling at 200 m/s at the distance of 70 km away from the phased array was simulated and is shown in Figure 4.9. The unambiguous range (4.6) and range resolution (4.7) are calculated as follows, with the speed of light $c = 3 \times 10^8$ m/s and the calculated radar signal bandwidth $B = 20$ MHz:

$$R_{unambiguous} = \frac{c}{2PRF} = \frac{3 \times 10^8}{2(1.429 \times 10^3)} = 105 \text{ km} \quad (4.6)$$

$$\Delta R = \frac{c}{2B} = \frac{3 \times 10^8}{2(20 \times 10^6)} = 7.5 \text{ m} \quad (4.7)$$

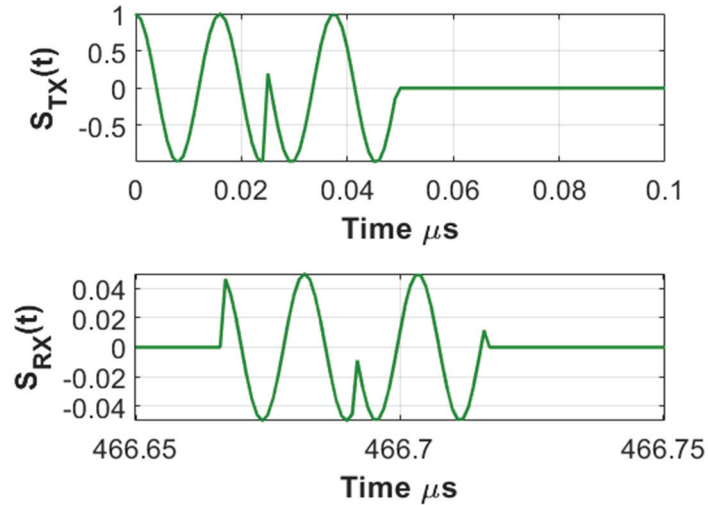


Figure 4.9. Barker coded transmission for the radar signal at -30° at 3.55 GHz and its return signal from the moving target.

The maximum unambiguous range for the selected PRF is 105 km and the moving target is located at 70 km, so the return echo can be detected and processed unambiguously in the radar receiver before the next radar pulse is transmitted [54]. If the moving target were located beyond 105 km at this PRF, the apparent return echo would be present in the next radar pulse, causing range ambiguity, since a second echo would be present, causing the target to appear closer than it really is. The range resolution for the selected Barker code signal bandwidth is 7.5 m, so the radar can distinguish between targets that are 7.5 m apart in range at the radar beam direction of -30° . The range resolution can be further improved by increasing the radar signal bandwidth. This may cause coexistence problems for other co-located users within the radar's transmission range, however, so the works by Egbert [3], Eustice [55], and Latham [56]-[57] can be applied to further optimize radar signal bandwidth while meeting spectrum requirements as well as radar ambiguity function requirements. The ambiguity function, described by,

$$\chi(\tau, u) = \int_{-\infty}^{\infty} s(t)s^*(t - \tau)e^{-j2\pi ut} dt, \quad (4.8)$$

is the two-dimensional response of a returned pulse from a target due to the receiver matched filter [58], given a signal $s(t)$, such as the transmitted signal in Figure 4.9, when the signal is received at a certain delay τ and with a certain Doppler shift u . To justify acceptable monostatic range radar performance, it is desired that the received waveform's ambiguity function contains minimal ambiguity along the range axis, which can be accomplished by transmitting short pulses and therefore, higher bandwidth radar signals. This is the justification for the selected bandwidth of the transmitted Barker code signal. The resulting ambiguity function of the simulated return signal from Figure 4.9 is shown in Figure 4.10. As observed, minimum ambiguity is placed along the range axis and maximum ambiguity is placed on the Doppler axis, therefore, high range resolution was achieved, indicating that the radar can more precisely detect the range of the target within its beam.

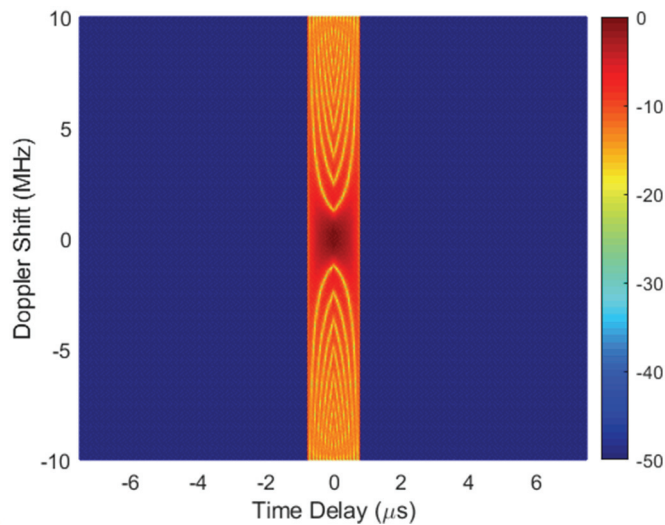


Figure 4.10. Normalized ambiguity function for the moving target radar return signal centered at 3.55 GHz in the radar direction of -30° .

4.3 Summary

An approach for synthesizing dual-beam transmission from a phased array system that can provide simultaneous radar and spatially secure communications signals has been presented. This work combines directional security concepts from communications into a shared radar and communications framework using a dual-beam, shared-frequency phased array system. The computation of the appropriate phasor excitations to feed each antenna element to maintain spatial security as well as the array pattern for each symbol state is significantly reduced. This provides a novel solution for a dual-beam, shared-frequency phased array that requires suitable radar functionality as well as real-time spatially secure communications. Such a multi-functional system will allow spatial, temporal, and spectral resources to be more efficiently and securely used in the ever-crowded spectral environment.

CHAPTER FIVE

Conclusion and Future Work

As the release of the fifth-generation (5G) and further future wireless standards approaches, the application of fast, reconfigurable element-wise impedance tuning will be essential for enhancing the performance of next-generation radar and communications systems that are typically designed with phased array transmitters consisting of many antenna elements. This dissertation has provided a better understanding of the electromagnetic physics involved in forming the array patterns for single-beam and dual-beam phased array transmitters, and has presented novel techniques in implementing impedance tuners in each element in the phased array to complete the required tasks and improve performance metrics for both transmission scenarios.

For the single-beam transmitter scenario, it was discovered that tuning the driven impedances of the array elements can affect the shape and scan angle of the array pattern, because changing the driven element impedance changes the excitation fed to each individual antenna element. As a result, when placing a reconfigurable impedance tuner between each PA and antenna element to tune the element-wise driven impedances, an identical tuning state must be implemented across all tuners to preserve the same relative magnitude and phase progressions of the element excitations, preserving the shape and scan angle of the single-beam array pattern. This concept was demonstrated in the ADS Momentum electromagnetic (EM) simulator using various single-beam scan angle examples for a four-element microstrip ULA phased array. A non-identical tuning state

was presented in which the inner element tuners and the outer element tuners were switched to slightly different states when attempting to steer the array to broadside. The array pattern was distorted severely as a result of this non-identical tuning as expected. Identical tuning states were then used on each tuner for broadside and other scan angles, which resulted in undisturbed shape and scan angle array patterns while also increasing transmitter output power, increasing range detection capabilities.

For the dual-beam transmitter scenario, it was shown through detailed mathematical calculations that, when attempting to transmit two beams at the same fundamental frequency from the same array, PA nonlinearities can cause IMD3 products to appear in the array pattern. This results in the transmission of two additional, unintended spurious beams. The IMD3 reversal factor κ_n was developed to serve as a metric in the impedance tuning to linearize the IMD3 caused by PA nonlinearities. It was shown that the IMD3 array pattern was corrected as a result of reducing the standard deviation of the vector κ_n magnitudes and phases as close to zero as possible through impedance tuning. A gradient-descent impedance tuning optimization is demonstrated to adjust the tunable capacitors that model the tuner resonant cavities. Additionally, it was shown that more collective signal amplification from each PA was achieved by reducing the κ_n as close to zero as possible, resulting in an increase in transmitter output power. This work showed a novel solution to resolve IMD3 artifacts that are transmitted at the fundamental frequency in a shared-frequency dual-beam RadCom system.

The dual-beam scenario was further enhanced with directional security as a result of the zero forcing directional modulation technique. Using the pseudo-inverse technique to calculate the required per-symbol excitation phase shifts, a known eavesdropper

location was sent intentional symbols to prevent information recovery, while simultaneously transmitting different symbol streams in the intended radar and communications directions. Additionally, Barker code sequencing was used to synthesize a radar pulse into a BPSK signal in the radar transmit mode and a zero signal in the receive mode. The pseudo-inverse phase shifts were recalculated in the transmit and receive modes. This ensured that the RadCom system can securely transmit both radar and communications signals while the radar continuously transitions from the transmit and receive modes.

It is intended in future work that the techniques developed in this dissertation for real-time impedance tuning will be implemented with fast programmable hardware and algorithm software from software-defined radio control for real-world adaptability. Future studies will also address the directional security solution discussed in Chapter Four with the addition of amplifier nonlinearities as discussed in Chapter Three. It should be examined how these nonlinearities affect the robustness of secure RadCom transmissions combined with reconfigurable impedance tuning. The findings in this dissertation will provide a framework for greater freedom and enhanced adaptability that will prove mission critical in real-world joint radar and communications applications.

BIBLIOGRAPHY

- [1] B. Badic *et al.*, "The Disruptor: The Millimeter-Wave Spectrum," in *Rolling Out 5G: Use Cases, Applications, and Technology Solutions*, Apress (Intel Corp.), 2016, pp. 111-130.
- [2] P. M. McCormick, S. D. Blunt and J. G. Metcalf, "Simultaneous radar and communications emissions from a common aperture, Part I: Theory," *2017 IEEE Radar Conference (RadarConf)*, Seattle, WA, 2017, pp. 1685-1690.
- [3] A. Egbert, C. Latham, C. Baylis and R. J. Marks, "Multi-dimensional coexistence: Using a spatial-spectral mask for spectrum sharing in directional radar and communication," *2018 Texas Symposium on Wireless and Microwave Circuits and Systems (WMCS)*, Waco, TX, 2018, pp. 1-6.
- [4] C. Baylis, A. Egbert, J. Alcala-Medel, A. Dockendorf, A. Martone and R. J. Marks, "Real-Time Circuit Reconfiguration for a Cognitive Software-Defined Radar Transmission: A New Paradigm in Spectrum Sharing," *2019 IEEE International Symposium on Electromagnetic Compatibility, Signal & Power Integrity (EMC+SIPI)*, New Orleans, Louisiana, July 2019, pp. 448-450.
- [5] R.L. Haupt, *Antenna Arrays: A Computational Approach*, Wiley-IEEE Press, 2010.
- [6] W.A. Sandrin, "Spatial Distribution of Intermodulation Products in Active Phased Array Antennas," *IEEE Transactions on Antennas and Propagation*, Vol. 21, No. 6, November 1973, pp. 864-868.
- [7] E.G. Larsson and L. Van Der Pierre, "Out-of-Band Radiation From Antenna Arrays Clarified," *IEEE Wireless Communications Letters*, Vol. 7, No. 4, August 2018, pp. 610-613.
- [8] C. Hemmi, "Pattern Characteristics of Harmonic and Intermodulation Products in Broad-Band Active Transmit Arrays," *IEEE Transactions on Antennas and Propagation*, Vol. 50, No. 6, June 2002, pp. 858-865.
- [9] R.L. Haupt, "Antenna Arrays in the Time Domain: An Introduction to Timed Arrays," *IEEE Antennas and Propagation Magazine*, Vol. 59, No. 3, June 2017, pp. 33-41.

- [10] C. Mollen, U. Gustavsson, T. Eriksson, and E.G. Larsson, "Spatial Characteristics of Distortion Radiated From Antenna Arrays With Transceiver Nonlinearities," *IEEE Transactions on Wireless Communications*, Vol. 17, No. 10, October 2018, pp. 6663-6679.
- [11] A.I. Zaghloul, O. Kilic, and E.C. Kohls, "System Aspects and Transmission Impairments of Active Phased Arrays for Satellite Communications," *IEEE Transactions on Aerospace and Electronic Systems*, Vol. 43, No. 1, January 2007, pp. 176-186.
- [12] S.L. Loyka, "The Influence of Electromagnetic Environment on Operation of Active Array Antennas: Analysis and Simulation Techniques," *IEEE Antennas and Propagation Magazine*, Vol. 41, No. 6, December 1999, pp. 23-39.
- [13] M. Obermier and E.J. Powers, "The Effects of Nonlinear High Power Amplifiers on Space Based Phased Array Antenna Patterns," 2000 International Conference on Phased Array Systems and Technology, Dana Point, California, May 2000, pp. 45-48.
- [14] T. Kaho, T. Nakagawa, K. Araki, and K. Horikawa, "Carrier Power to Intermodulation-Distortion Power-Ratio-Increasing Technique in Active Phased-Array Antenna Systems," *IEEE Transactions on Microwave Theory and Techniques*, Vol. 50, No. 12, December 2002, pp. 2987-2994.
- [15] B. Rupakula and G. Rebeiz, "Third-Order Intermodulation Effects and System Sensitivity Degradation in Receive-Mode 5G Phased Arrays in the Presence of Multiple Interferers," *IEEE Transactions on Microwave Theory and Techniques*, Vol. 66, No. 12, December 2018, pp. 5780-5795.
- [16] K. Yamauchi, M. Nakayama, Y. Ikeda, Y. Isota and T. Takagi, "Novel reduction technique of the non-linear distortion at the receiving point in the multi-beam active phased array antenna," *2005 Asia-Pacific Microwave Conference Proceedings*, Suzhou, 2005.
- [17] E. Lier and A. Cherrette, "An intermodulation suppression technique for transmit active phased array satellite antennas with multiple shaped beams," in *IEEE Transactions on Antennas and Propagation*, vol. 53, no. 5, pp. 1853-1858, May 2005.
- [18] K. G. Johannsen, "Scan Beam Antenna Intermodulation Improvement Due to Spatial Dispersion," in *IEEE Transactions on Aerospace and Electronic Systems*, vol. AES-23, no. 4, pp. 543-557, July 1987.
- [19] A. O'Connor and D. Rabideau, "Dual-Beam Transmit from Shared Aperture with Constant Envelope Constraint," 2019 IEEE Radar Conference, Boston, Massachusetts, April 2019.

- [20] R.L. Haupt and M.D. Weiss, "Power Amplifier Models for Multi-Beam Wideband Active Transmit Arrays," *2014 IEEE Antennas and Propagation Society International Symposium (APSURSI)*, Memphis, TN, 2014, pp. 1750-1751.
- [21] C. Rapp, "Effects of HPA-nonlinearity on a 4-DPSK/OFDM-signal for a digital sound broadcasting system," in *Proceedings of the Second European Conference on Satellite Communications*, Liege, Belgium, Oct. 22-24, 1991, pp. 179-184.
- [22] R.N. Braithwaite, "Amplifier Nonlinearities in an Antenna Array During Spatially Multiplexed Transmissions," *2020 IEEE Radio and Wireless Symposium*, San Antonio, Texas, January 2020.
- [23] P. Rodriguez-Garcia, J. Sifri, C. Calabrese, C. Baylis and R. J. Marks, "Spurious Beam Suppression in Dual-Beam Phased Array Transmission by Impedance Tuning," submitted to *IEEE Transactions on Antennas and Propagation*, January 2020.
- [24] Y. Sun *et al.*, "Adaptive Impedance Matching and Antenna Tuning for Green Software-Defined and Cognitive Radio," *2011 IEEE 54th International Midwest Symp. Circuits and Systems*, Seoul, South Korea, 2011.
- [25] J. de Mingo, A. Valdovinos, A. Crespo, D. Navarro and P. Garcia, "An RF electronically controlled impedance tuning network design and its application to an antenna input impedance automatic matching system," in *IEEE Transactions on Microwave Theory and Techniques*, vol. 52, no. 2, pp. 489-497, Feb. 2004.
- [26] Q. Gu and A. S. Morris, "A New Method for Matching Network Adaptive Control," in *IEEE Transactions on Microwave Theory and Techniques*, vol. 61, no. 1, pp. 587-595, Jan. 2013.
- [27] A. Semnani, M. Abu Khater, D. Peroulis, C. Baylis, L. Hays, C. Kappelmann, and Z. Hays, "An Evanescent-Mode Cavity-Based HighPower Impedance Tuner for Adaptive Radar Applications," *USNCURSI Nat'l Radio Sci. Mtg.*, Boulder, CO, Jan. 2018.
- [28] J. Alcalá-Medel *et al.*, "Fast Frequency-Agile Real-Time Optimization of High-Power Tuning Network for Cognitive Radar Applications," *2019 IEEE MTT-S International Microwave Symposium (IMS)*, Boston, MA, USA, 2019, pp. 1466-1469.
- [29] J. J. Luther and X. Gong, "A Microstrip Patch Phased Array Antenna with Parasitic Elements and Reactance-Tuned Coupling," *2011 IEEE International Symp. on Antennas and Prop.*, Spokane, WA, 2011, pp. 3291-3294.

- [30] E. Magill and H. Wheeler, "Wide-Angle Impedance Matching of a Planar Array Antenna by a Dielectric Sheet," in *IEEE Trans. Antennas and Prop.*, Vol. 14, No. 1, Jan. 1966, pp. 49-53, January 1966.
- [31] R. Xia *et al.*, "Experimental Investigation of Wide-Angle Impedance Matching of Phased Array Using Overlapped Feeding Network," *IEEE Antennas and Wireless Prop. Letters*, Vol. 13, 2014, pp. 1284-1287.
- [32] P. Rodriguez-Garcia, J. Sifri, C. Calabrese, C. Baylis and R. J. Marks, "Range Improvement in Single-Beam Phased Array Radars by Amplifier Impedance Tuning," submitted to *IEEE Transactions on Antennas and Propagation*, January 2020.
- [33] P. M. McCormick, C. Sahin, S. D. Blunt and J. G. Metcalf, "FMCW Implementation of Phase-Attached Radar-Communications (PARC)," *2019 IEEE Radar Conference (RadarConf)*, Boston, MA, USA, 2019, pp. 1-6.
- [34] C. Sahin, P.M. McCormick, J.G. Metcalf, and S.D. Blunt, "Power-Efficient Multi-Beam Phase-Attached Radar/Communications," *IEEE Radar Conference*, Boston, MA, 22-26 Apr. 2019.
- [35] B. Ravenscroft, P.M. McCormick, S. Blunt, E.S. Perrins, C. Sahin, J.G. Metcalf, "Experimental Assessment of Tandem-Hopped Radar and Communications (THoRaCs)," *International Radar Conference*, Toulon, France, 23-27 September 2019.
- [36] M. P. Daly and J. T. Bernhard, "Directional Modulation Technique for Phased Arrays," in *IEEE Transactions on Antennas and Propagation*, vol. 57, no. 9, pp. 2633-2640, Sept. 2009.
- [37] M. P. Daly and J. T. Bernhard, "Directional modulation and coding in arrays," *2011 IEEE International Symposium on Antennas and Propagation (APSURSI)*, Spokane, WA, 2011, pp. 1984-1987.
- [38] T. Xie, J. Zhu and Y. Li, "Artificial-Noise-Aided Zero-Forcing Synthesis Approach for Secure Multi-Beam Directional Modulation," in *IEEE Communications Letters*, vol. 22, no. 2, pp. 276-279, Feb. 2018.
- [39] F. Yinjuan, L. Yong, H. Qiongdan and Z. Kunhui, "Design and analysis of LFM/Barker RF stealth signal waveform," *2016 IEEE 11th Conference on Industrial Electronics and Applications (ICIEA)*, Hefei, 2016, pp. 591-595.
- [40] P. Rodriguez-Garcia, G. Ledford, C. Baylis and R. J. Marks, "Real-Time Synthesis Approach for Simultaneous Radar and Spatially Secure Communications from a Common Phased Array," *2019 IEEE Radio and Wireless Symposium (RWS)*, Orlando, FL, USA, 2019, pp. 1-4.

- [41] J. Allen, "Gain and Impedance Variation in Scanned Dipole Arrays," *IRE Transactions on Antennas and Propagation*, Vol. 10, No. 5, September 1962, pp. 566-572.
- [42] D. Qiao, R. Molfino, S. M. Lardizabal, B. Pillans, P. M. Asbeck and G. Jerinic, "An Intelligently Controlled RF Power Amplifier with a Reconfigurable MEMS-Varactor Tuner," *IEEE Transactions on Microwave Theory and Techniques*, Vol. 53, No. 3, March 2005, pp. 1089-1095.
- [43] A. Semnani, M. Abu Khater, Y. Wu and D. Peroulis, "An Electronically Tunable High-Power Impedance Tuner With Integrated Closed-Loop Control," *IEEE Microwave and Wireless Components Letters*, Vol. 27, No. 8, August 2017, pp. 754-756.
- [44] C. Calabrese, A. Dockendorf, A. Egbert, B. Herrera, C. Baylis, and R. J. Marks II, "Fast Switched-Stub Impedance Tuner Reconfiguration for Frequency and Beam Agile Radar and Electronic Warfare Applications," submitted to 2020 IEEE International Radar Conference, Washington, D.C., April 2020.
- [45] Sechi, Franco, and Marina Bujatti. *Solid-State Microwave High-Power Amplifiers*. Artech House, 2009. Print.
- [46] Y. L. Sit, L. Reichardt, C. Sturm and T. Zwick, "Extension of the OFDM joint radar-communication system for a multipath, multiuser scenario," *2011 IEEE RadarCon (RADAR)*, Kansas City, MO, 2011, pp. 718-723.
- [47] Y. Liu, G. Liao and Z. Yang, "Range and angle estimation for MIMO-OFDM integrated radar and communication systems," *2016 CIE International Conference on Radar (RADAR)*, Guangzhou, 2016, pp. 1-4.
- [48] X. Liu, Y. Liu, X. Wang and J. Zhou, "Application of communication OFDM waveform to SAR imaging," *2017 IEEE Radar Conference (RadarConf)*, Seattle, WA, 2017, pp. 1757-1760.
- [49] L. Hu, Z. Du and G. Xue, "Radar-communication integration based on OFDM signal," *2014 IEEE International Conference on Signal Processing, Communications and Computing (ICSPCC)*, Guilin, 2014, pp. 442-445.
- [50] A. Hassanien, M. G. Amin, Y. D. Zhang and F. Ahmad, "A dual function radar-communications system using sidelobe control and waveform diversity," *2015 IEEE Radar Conference (RadarCon)*, Arlington, VA, 2015, pp. 1260-1263.
- [51] H. Fu, S. Abeywickrama, L. Zhang and C. Yuen, "Low-Complexity Portable Passive Drone Surveillance via SDR-Based Signal Processing," in *IEEE Communications Magazine*, vol. 56, no. 4, pp. 112-118, April 2018.

- [52] Y. Chen, Y. Nijsure, C. Yuen, Y. H. Chew, Z. Ding and S. Boussakta, "Adaptive Distributed MIMO Radar Waveform Optimization Based on Mutual Information," in *IEEE Transactions on Aerospace and Electronic Systems*, vol. 49, no. 2, pp. 1374-1385, April 2013.
- [53] R. C. Daniels and R. W. Heath, "Link Adaptation with Position/Motion Information in Vehicle-to-Vehicle Networks," in *IEEE Transactions on Wireless Communications*, vol. 11, no. 2, pp. 505-509, Feb. 2012.
- [54] Richards, M. A., Jim Scheer, and William A. Holm. *Principles of Modern Radar / Basic Principles*. Raleigh, NC: SciTech Pub., 2010. Print.
- [55] D. Eustice, C. Latham, C. Baylis, R. J. Marks and L. Cohen, "Amplifier-in-the-Loop Adaptive Radar Waveform Synthesis," in *IEEE Transactions on Aerospace and Electronic Systems*, vol. 53, no. 2, pp. 826-836, April 2017.
- [56] C. Latham, A. Egbert, C. Baylis, L. Cohen and R. J. Marks, "Joint Radar Amplifier Circuit and Waveform Optimization for Ambiguity Function, Power-Added Efficiency, and Spectral Compliance," in *IEEE Transactions on Aerospace and Electronic Systems*, vol. 55, no. 3, pp. 1190-1199, June 2019.
- [57] C. Latham, M. Fellows, C. Baylis, L. Cohen and R. J. Marks, "Radar waveform optimization for ambiguity function properties and dynamic spectral mask requirements based on communication receiver locations," *2017 IEEE Radio and Wireless Symposium (RWS)*, Phoenix, AZ, 2017, pp. 147-149.
- [58] P. Woodward, *Probability and Information Theory with Applications to Radar*, New York: Pergamon Press, 1953.
- [59] A. Semnani, G.S. Shaffer, M.D. Sinanis, and D. Peroulis, "High-Power Impedance Tuner Utilising Substrate-Integrated Evanescent-Mode Cavity Technology and External Linear Actuators," *IET Microwaves, Antennas & Propagation*, Vol. 13, No. 12, October 2019, pp. 2067-2072.